

Magnetic anisotropies of (Ga,Mn)As films and nanostructures



DISSERTATION
ZUR ERLANGUNG DES DOKTORGRADES
DER NATURWISSENSCHAFTEN (DR. RER. NAT.)
DER FAKULTÄT PHYSIK
DER UNIVERSITÄT REGENSBURG

vorgelegt von
Frank Hoffmann
aus Passau

2010

Promotionsgesuch eingereicht am 06.10.2010

Die Arbeit wurde angeleitet von: Prof. Dr. C. H. Back

Prüfungsausschuss:

Vorsitzender: Prof. Dr. J. Fabian
1. Gutachter: Prof. Dr. C. H. Back
2. Gutachter: Prof. Dr. D. Weiss
Weiterer Prüfer: Prof. Dr. J. Lupton

Tag des Promotionskolloquiums: 02.02.2011

Contents

1	Introduction	1
2	Theoretical basics	5
2.1	Ferromagnetism	5
2.2	Magnetic energies and fields	6
2.2.1	Exchange Energy	6
2.2.2	Demagnetizing energy	6
2.2.3	Anisotropy energy	7
2.2.4	Zeeman Energy	10
2.3	Magnetization Dynamics	10
2.3.1	Equation of motion	10
2.3.2	The Landau-Lifshitz-Gilbert Equation	11
2.3.3	Basic concept of ferromagnetic resonance	11
2.3.4	Ferromagnetic resonance condition	12
2.3.5	Calculation of the FMR lineshape	13
3	Structural and magnetic properties of (Ga,Mn)As	17
3.1	Structural properties of (Ga,Mn)As films	17
3.1.1	Point defects	18
3.1.2	Lattice constant	19
3.2	Ferromagnetism in (Ga,Mn)As	21
3.2.1	Mean field Zener model	22
3.3	Magneto-crystalline anisotropies	23
3.3.1	Cubic anisotropy	23
3.3.2	Perpendicular anisotropy	24
3.3.3	Uniaxial in-plane anisotropy	24
4	Experimental techniques	27
4.1	Magneto-optic Kerr effect	27
4.2	Stroboscopic pump-probe technique	29
4.3	Components of the low-temperature time-resolved MOKE setup	30
4.3.1	Microscope cryostat	30
4.3.2	Magnetic DC field	30
4.4	Ferromagnetic resonance scanning Kerr microscopy	31
4.4.1	Excitation of the precessional motion	31
4.4.2	Scanning Kerr microscopy	32

4.5	All-optical pump-probe technique	35
5	Magnetic anisotropy and damping of (Ga,Mn)As films	39
5.1	Comparison of local and integral FMR techniques	39
5.2	Effects of microwave excitation	42
5.3	Magnetic anisotropies of (Ga,Mn)As films	43
5.3.1	Influence of annealing and Mn-concentration	47
5.3.2	Temperature dependence of the magnetic anisotropies	49
5.3.3	Conclusion	52
5.4	Electrical detection of the ferromagnetic resonance	53
5.5	Magnetic relaxation mechanisms	57
5.5.1	Intrinsic and extrinsic contributions of the FMR linewidth	58
5.5.2	Previous studies of the FMR linewidth in (Ga,Mn)As films	60
5.5.3	Homogeneity of the magnetic properties on macroscopic length scales	61
5.5.4	Homogeneity of the magnetic anisotropies on a sub-micrometer length scale	63
5.5.5	Intrinsic damping in (Ga,Mn)As films	67
5.5.6	Conclusion	68
5.6	Time-resolved experiments	69
5.6.1	All-optical pump-probe measurements	70
5.6.2	Acoustic strain waves	74
5.6.3	Transient changes of the magnetic anisotropies	75
6	Magnetic anisotropy and coercive fields of (Ga,Mn)As nanostructures	81
6.1	Magnetic anisotropies of rectangular (Ga,Mn)As elements	82
6.1.1	Structural properties	82
6.1.2	Quantitative determination of the anisotropies	83
6.2	Magnetic anisotropies of circular (Ga,Mn)As elements	86
6.3	Visualization of local variations of the magnetic anisotropy	87
6.4	Magnetization reversal in (Ga,Mn)As micro- and nanostructures	89
6.5	Origin of the intrinsic uniaxial in-plane anisotropy	93
7	Summary and Outlook	99
8	Appendix	101
8.1	Molecular beam epitaxy of (Ga,Mn)As films	101
8.2	Sample preparation	101
8.3	Coplanar Waveguides	103
	Bibliography	107
	Publications	117
	Acknowledgements	119

1 Introduction

The rapidly emerging field of spintronics, which makes use of both the electron spin and charge has already found its way into everyday's life. The most prominent example is the read head of a commercial magnetic hard disk drive which is based on the so called giant magneto-resistance effect (GMR) or the tunneling magneto-resistance effect (TMR). The GMR effect which was discovered independently by P. Grünberg and A. Fert in 1988 [1, 2], describes the dependence of the electrical resistance in a stack of thin ferromagnetic and nonmagnetic layers on the relative orientation of the magnetization in adjacent layers. The successful implementation of GMR based read heads has contributed significantly to the increase of the storage density in magnetic hard disk drives. In spintronics, during the last two decades, diluted magnetic semiconductors have attracted much attention due to their potential of combining both the storage and manipulation of data by means of a single material system. In 1996 for the first time the diluted magnetic semiconductor (Ga,Mn)As with ferromagnetic properties at low temperatures was grown successfully [3]. For many years this material has been considered as the most promising candidate for a magnetic semiconductor at room temperature. In theory, a Curie temperature of 300 K was predicted for 10% concentration of uncompensated Mn_{Ga} acceptors [4]. Although substantial efforts have been put into the optimization of the growth and the post-growth treatment of (Ga,Mn)As a further increase in the Curie temperature from currently 180-190 K [5, 6] up to temperatures well above room temperature is unlikely. Nevertheless, from a physical point of view (Ga,Mn)As is a very interesting material exhibiting a multitude of novel physical effects. As an example, by applying a gate voltage purely electrical manipulations of the magnetic properties such as magnetic anisotropies or Curie temperature have been demonstrated for the very first time [7, 8].

For various kinds of experiments and also for applications the possibility to control the magnetic anisotropies is desirable. The anisotropies directly influence the magnetic ground state, the width of domain walls, the coercive fields, etc. Yet, the magnetic anisotropies in (Ga,Mn)As can hardly be adjusted or not even be reproduced because they depend crucially on various parameters such as hole and Mn-concentration, post-growth annealing, etc. which cannot be fully controlled during the fabrication process. However, recent SQUID and magnetotransport experiments have shown that the magnetic anisotropies in lithographically prepared (Ga,Mn)As elements differ clearly from the unpatterned (Ga,Mn)As films [9–11]. Such nanostructured elements can be used to adjust the magnetic anisotropy well-directed and reproducible.

In order to quantitatively determine various magnetic properties of such small magnetic elements, a combination of ferromagnetic resonance (FMR) and Kerr microscopy is employed in this thesis. The technique offers several advantages compared to the

SQUID and magneto-transport measurements of the earlier publications [9–11]. On the one hand, a quantitative determination of the magnetic anisotropy in these type of experiments is very complex and is only possible under the assumption of a single domain state. This, however, is not justified for elements in the size range of hundreds of nanometers to micrometer. On the other hand, these techniques only measure the average magnetic properties of one or an array of similar magnetic elements. The novel low-temperature Kerr-FMR setup offers the possibility to determine the magnetic anisotropies and damping of individual elements with submicrometer spatial resolution. The reliability of the novel technique is tested by comparing the experimental results of a (Ga,Mn)As film to conventional ferromagnetic resonance measurements. After the investigation of (Ga,Mn)As films, the magnetic anisotropies of (Ga,Mn)As elements of various sizes, orientations and shapes are determined quantitatively. The results from the experiments are also used to perform micromagnetic simulations of the ground state and switching process in these patterned structures. Both the experimental investigation and the simulation of the coercive fields show that the changed magnetic anisotropies also influence the static magnetic properties. These results are of special importance for various experiments where information about the magnetic anisotropies and coercive fields is not accessible.

Besides the investigation of the magnetic anisotropies of (Ga,Mn)As films and nanostructured elements, two additional topics are addressed in this thesis: First, in conventional FMR studies large extrinsic contributions to the FMR linewidth are found in (Ga,Mn)As films which is an indication of a large magnetic inhomogeneity of the films. Yet, these measurements give no information about the relevant length scales and represent only the integral response of the whole macroscopic film. Therefore, frequency dependent *local* measurements of the FMR linewidth are performed in order to draw conclusions about the homogeneity of various magnetic properties on different length scales. Second, it is well established that the magnetic properties in (Ga,Mn)As depend crucially on the hole concentration since the holes mediate the ferromagnetic order in (Ga,Mn)As. Recent time-resolved experiments [12, 13] indicate that photoexcited holes can cause transient changes of the magnetization and the magnetic anisotropies occurring on a subnanosecond time scale. Yet, the magnetic parameters in these all-optical pump-probe measurements could not be determined quantitatively. By combining all-optical pump-probe and Kerr-FMR techniques the question is addressed how photoexcited carriers influence the magnetic properties on a picosecond to nanosecond time scale.

The thesis is structured as follows:

- **Chapter 2** provides the magnetic interactions and energies in the domain of ferromagnetism. Furthermore, the condition for ferromagnetic resonance which is essential for the experimental determination of magnetic anisotropies will be derived.
- The basic physical properties of the material system (Ga,Mn)As will be covered in **Chapter 3**. The structural and magnetic properties will be addressed with special emphasis on the magnetic anisotropies.

-
- The employed experimental techniques will be explained in **Chapter 4**. They can be divided into techniques in the time domain, such as time resolved scanning Kerr microscopy and techniques in the frequency domain, such as Kerr-FMR.
 - In **Chapter 5** the experimental results on the magnetic anisotropies, the damping and the homogeneity of (Ga,Mn)As films will be presented. The influence of Mn-, hole concentration and temperature on the magnetic anisotropies will be discussed. Furthermore, the influence of a short optical pump pulse on the magnetic properties, such as anisotropies is investigated.
 - The reduction of the lateral dimensions of a (Ga,Mn)As film changes the magnetic anisotropies and the switching behavior. The results on (Ga,Mn)As nanostructures and micromagnetic simulations will be presented in **Chapter 6**.
 - **Chapter 7** summarizes the thesis and gives an outlook on possible future experiments.

2 Theoretical basics

This chapter provides a basis for the comprehension of the physics of the phenomena discussed in the course of this thesis. First, a brief introduction into ferromagnetism is given. In Section 2.2 the contributions to the magnetic energy which define the equilibrium orientation of the magnetization will be discussed. The field of magnetization dynamics which describes the response of the magnetization to an external stimulus will be addressed in Section 2.3. Based on the equation of motion and on the magnetic energies, the ferromagnetic resonance condition will be derived in sections 2.3.4 and 2.3.5.

2.1 Ferromagnetism

In the absence of an external magnetic field the magnetic moments in paramagnetic materials are oriented randomly, leading to a spontaneous magnetization equal to zero. In contrast ferromagnetic materials have a non-vanishing spontaneous magnetization because the magnetic moments align parallel. Although the formation of the ferromagnetism in various materials is usually very complex, due to the itinerant (delocalized) character of the electrons in ferromagnetic metals such as iron, nickel and cobalt, the free electron gas model can be used as a simple illustration [14]: The spins of the electrons align in such a way that the total energy consisting of kinetic energy and exchange energy is minimized. The exchange interaction is a consequence of the Coulomb interaction between the electrons and Pauli's exclusion principle which can only be understood using quantum-mechanical principles. Electrons with the same spin orientation may not occupy the same electronic state and thus may not reside at the same position. Therefore the Coulomb energy can be minimized when the electrons have a parallel spin orientation because their average distance is larger than for an antiparallel alignment. If this gain of exchange energy is larger than the cost of kinetic energy which is caused by the spin-splitting and reoccupation of the bands a long range ferromagnetic order can be induced.

In the Heisenberg model the exchange interaction is described by the Hamiltonian

$$H_{\text{ex}} = -2 \sum_{i < j} J_{ij} \vec{S}_i \cdot \vec{S}_j, \quad (2.1)$$

where J_{ij} is the exchange integral and \vec{S}_i and \vec{S}_j are the spins at the lattice sites i and j . The summation extends only over nearest neighbors. This reflects the short range of the exchange interaction. A positive sign of J_{ij} leads to a parallel alignment of the spins which corresponds to a ferromagnetic order.

2.2 Magnetic energies and fields

The magnetization configuration of a magnetic sample is defined by the interplay of different magnetic energies. The total free energy E is obtained by adding various contributions, such as exchange energy E_{ex} , anisotropy energy E_{ani} , demagnetizing energy E_{dem} and Zeeman energy E_{zee} . The free energy density ε which is obtained by dividing the energy by the volume V of the magnetic sample reads:

$$\varepsilon = \frac{E}{V} = \frac{1}{V} (E_{\text{ex}} + E_{\text{ani}} + E_{\text{dem}} + E_{\text{zee}}). \quad (2.2)$$

These contributions will be described in the following. When addressing the dynamic behavior of the magnetization, the effective magnetic field \vec{H}_{eff} is commonly used instead of the magnetic energy. The correlation between these parameters is given by the functional derivative of the total energy:

$$\vec{H}_{\text{eff}} = -\frac{1}{\mu_0} \frac{\delta E[\vec{M}]}{\delta \vec{M}(\vec{r})}, \quad (2.3)$$

2.2.1 Exchange Energy

In the continuum approximation, where the microscopic arrangement of magnetic moments inside the crystal is neglected and the energy is obtained by integrating over all moments within the sample volume V , the exchange energy is given by [14]:

$$E_{\text{ex}} = \frac{A}{M_S} \int (\nabla \vec{M})^2 dV, \quad (2.4)$$

where A is the exchange constant and M_S is the saturation magnetization.

2.2.2 Demagnetizing energy

Although the dipolar interaction is not responsible for the formation of the ferromagnetic order, it plays a major role for the equilibrium orientation of the magnetization in samples with various shapes. This can be illustrated by considering a thin magnetic film, whose lateral dimensions are much larger than its thickness t , see Fig. 2.1. When the magnetization is aligned perpendicular to the film plane, magnetic poles are created at the upper and lower surface of the film, which - due to the relation $\vec{\nabla} \vec{H} = -\vec{\nabla} \vec{M}$ (following from Maxwell's law $\vec{\nabla} \vec{B} = 0$) - lead to a field which is oriented opposite to the magnetization inside the film. Because this field shows the tendency to demagnetize the sample, it is referred to as demagnetizing field \vec{H}_{dem} . In contrast, when the magnetization is aligned in the film plane, the demagnetizing and stray fields can be fully neglected because of the very large distance between the magnetic poles which are created at the small side surfaces. Hence, in order to avoid demagnetizing fields the magnetization favors to align in the film plane.

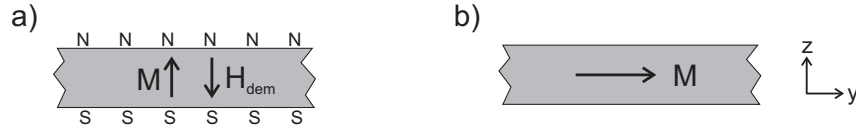


Figure 2.1: Cross section of a thin magnetic film. (a) If the magnetization is oriented perpendicular to the film plane, magnetic poles are created which lead to a demagnetizing field \vec{H}_{dem} . (b) For parallel alignment of the magnetization in the film plane, the demagnetizing field is negligible.

The demagnetizing energy reads:

$$E_{\text{dem}} = -\frac{\mu_0}{2} \int_V \vec{M} \cdot \vec{H}_{\text{dem}} \, dV, \quad (2.5)$$

where the integration extends over the sample volume V . In the case of an arbitrary shaped sample both the determination of the inhomogeneous demagnetizing field $\vec{H}_{\text{dem}}(\vec{r})$ and of the magnetization configuration $\vec{M}(\vec{r})$ are very complex and can only be performed numerically. Yet, for a homogeneously magnetized ellipsoid the demagnetizing field can be expressed by a simple analytic expression: $\vec{H}_{\text{dem}} = -\hat{N} \cdot \vec{M}$. The dimensionless demagnetizing tensor \hat{N} can be diagonalized when the magnetization is aligned along one of the principal axes a , b or c of the ellipsoid. The sum of the diagonal elements fulfills the condition $N_a + N_b + N_c = 1$. The above discussed film can be treated as a very flat and extended ellipsoid with $a, b \rightarrow \infty$ and $c \rightarrow 0$. In this case, the in-plane components of the demagnetizing tensor N_a and N_b equal zero, hence the perpendicular component is $N_c = 1$. For perpendicular orientation of the magnetization ($\vec{M} \parallel z$ -direction), the demagnetizing field is thus given by: $\vec{H}_{\text{dem}} = (0, 0, M_S)$. For arbitrary angles θ of \vec{M} with respect to the film normal, the demagnetizing energy density reads:

$$\varepsilon_{\text{dem}} = \frac{\mu_0}{2} M_S^2 \cos^2 \theta. \quad (2.6)$$

Another sample shape which plays a major role in this thesis are flat rectangular bars. The demagnetizing factors for homogeneously magnetized rectangular prisms were calculated analytically by A. Aharoni [15]. As an approximation, bars whose length is much larger than their width can be considered as infinitely long bars with rectangular cross section. In this case the demagnetizing factors depend only on the aspect ratio $p = w/t$, where w is the stripe width and t is the film thickness. For a typical aspect ratio $p = 10$, the demagnetizing factor perpendicular to the stripe axis $N_y \approx 0.05$ is very small. Consequently, it is a good approximation to treat also these magnetic stripes as extended films.

2.2.3 Anisotropy energy

The fact that the magnetization in many ferromagnetic solids prefers to align along certain directions, is referred to as magnetic anisotropy. The shape anisotropy which

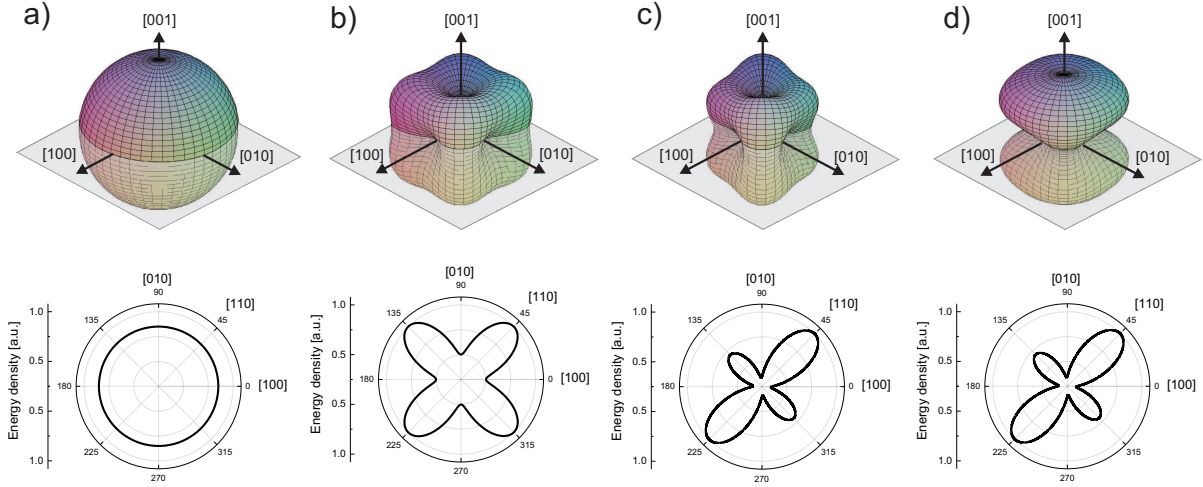


Figure 2.2: Illustration of the influence of different magnetic anisotropy contributions on the free energy surfaces in a cubic system. The minima (maxima) in these landscapes correspond to easy (hard) axes of the magnetization, respectively. Three dimensional plots of the free energy density without external field $H_0 = 0$ are shown in the upper row. The respective cross sections of the energy surfaces with the (001)-plane are illustrated in the lower row. (a) Without magnetic anisotropies (all K_i 's = 0) the energy surface is spherical. (b) Cubic magnetic anisotropy with $K_C > 0$. (c) Energy density (b) after adding a uniaxial in-plane anisotropy with $K_{U\parallel} > 0$. (d) Resulting energy density after adding a uniaxial perpendicular anisotropy with $K_{U\perp} < 0$.

depends only on the macroscopic shape of the sample was discussed in the previous section. In (Ga,Mn)As, the magneto-crystalline anisotropy which reflects the symmetry of the crystal structure and is caused by the spin-orbit interaction is of particular importance. Its origin will be discussed in more detail in Section 3.3. The magneto-crystalline anisotropy energy can be expressed using the direction cosines of the magnetization vector with respect to the $\langle 100 \rangle$ axes: $\alpha_1, \alpha_2, \alpha_3$. For a crystal with cubic symmetry, the expression for the anisotropy energy has to be invariant under permutation of the coordinates. In addition, only quadratic terms of the direction cosines are permitted. The term of lowest order which fulfills this condition $\alpha_1^2 + \alpha_2^2 + \alpha_3^2$ is equal to one and can be dropped. The next higher term satisfying the condition is the second power of the previous term: $(\alpha_1^2 + \alpha_2^2 + \alpha_3^2)^2$. Following up this approach and considering also terms of higher order, one can show that the energy density can be expressed in the form:

$$\varepsilon_{\text{ani}} = K^{(1)}(\alpha_1^2\alpha_2^2 + \alpha_2^2\alpha_3^2 + \alpha_3^2\alpha_1^2) + K^{(2)}(\alpha_1^2\alpha_2^2\alpha_3^2) + \dots, \quad (2.7)$$

where $K^{(1)}$ and $K^{(2)}$ represent the anisotropy constants of first and second order. Terms of higher order were omitted for simplicity. The term of lowest order in Eq. 2.7 already allows a description of the cubic magnetic anisotropy which is observed for instance in monocrystalline iron and nickel. The corresponding energy landscape is plotted in Fig. 2.2(b). For positive K_1 , the energy minima lie along the $\langle 100 \rangle$ directions. When the magnetization is aligned in the film plane (001), α_3 equals zero, and the second term in Eq. 2.7 vanishes. Thus, only the term of lowest order $K^{(1)}$ is observed experimentally

in this configuration. After simple algebraic transformations Eq. 2.7 simplifies to

$$\varepsilon_{C\parallel} \sim K_C \cos(4\varphi), \quad (2.8)$$

where φ is the angle of the magnetization vector with respect to the [100] axis, and $K_C \sim K^{(1)}$ is the cubic anisotropy constant. This energy term reflects the fourfold symmetry of this magnetic anisotropy with two easy axes along the [100] and [010] directions as shown by the intersection of the energy surface with the (001) plane in Fig. 2.2(b). Anisotropy energy expressions for various other types of crystals are given in Ref. [16].

In thin magnetic films also a uniaxial anisotropy $K_{U\parallel}$ in the film plane (001) is often observed experimentally, which due to symmetry reasons should not exist in cubic or tetragonal crystal structures. In (Ga,Mn)As films the physical origin of this anisotropy is still unclear, for details refer to Chapter 5. This in-plane uniaxial anisotropy energy density reads:

$$\varepsilon_{U\parallel} = K_{U\parallel} \sin^2(\varphi - \varphi_U), \quad (2.9)$$

where φ_U denotes the angle of the easy axis of this anisotropy with respect to the [100]-direction for a positive $K_{U\parallel}$. The additional effect on the energy landscape for $\varphi_U = -45^\circ$ is illustrated in Fig. 2.2(c), where the [110] and [1-10]-directions are not equivalent any more.

Finally, the lattice mismatch between the magnetic film and the substrate can lead to a tetragonal distortion of the film, where the lattice constants in the film plane and perpendicular to the film plane differ. This distortion induces a uniaxial anisotropy perpendicular to the film plane which has the same form as the parallel uniaxial anisotropy

$$\varepsilon_{U\perp} = -K_{U\perp} \cos^2 \theta, \quad (2.10)$$

where θ is the angle of the magnetization with respect to the film normal. The effect on the energy landscape for a negative $K_{U\perp}$, which corresponds to a hard axis along the growth direction is illustrated in Fig. 2.2(d).

The resulting anisotropy energy density is obtained by summing all anisotropy contributions. For a thin tetragonal magnetic film with arbitrary magnetization direction (Fig. 2.2(d)) and additional uniaxial in-plane anisotropy, it reads [16]:

$$\begin{aligned} \varepsilon_{\text{ani}} = & \frac{\mu_0}{2} M_S^2 \cos^2 \theta - K_{U\perp} \cos^2 \theta - \frac{1}{2} K_{C\perp} \cos^4 \theta \\ & - \frac{1}{8} K_{C\parallel} (3 + \cos 4\varphi) \sin^4 \theta - K_{U\parallel} \sin^2(\varphi - \varphi_U) \sin^2 \theta \end{aligned} \quad (2.11)$$

The first term describes the shape anisotropy of a thin magnetic film, see Section 2.2.2. $K_{U\parallel}$ and $K_{U\perp}$ are the uniaxial in- and out-of-plane anisotropies. Due to the tetragonal distortion of the crystal, the cubic anisotropy is split into an in-plane ($K_{C\parallel}$) and out-of-plane ($K_{C\perp}$) anisotropy term.

When the magnetization is aligned in the film plane ($\theta = 90^\circ$) one obtains:

$$\varepsilon_{\text{ani}}^{(001)} = -\frac{1}{8} K_{C\parallel} (3 + \cos 4\varphi) - K_{U\parallel} \sin^2(\varphi - \varphi_U) \quad (2.12)$$

Note that only the cubic and uniaxial in-plane anisotropies determine the magnetic energy density in the film plane.

2.2.4 Zeeman Energy

The Zeeman energy describes the interaction of the magnetization \vec{M} with an external magnetic field \vec{H}_0 :

$$E_{zee} = -\mu_0 \int_V \vec{M} \cdot \vec{H}_0 dV. \quad (2.13)$$

Parallel alignment of the magnetization and field direction is energetically preferred.

2.3 Magnetization Dynamics

The reaction of the magnetization to fast time-dependent magnetic fields with frequencies in the mega- and gigahertz range is treated in the framework of magnetization dynamics. The equation of motion which describes the temporal behavior of the magnetization will be addressed in sections 2.3.1 and 2.3.2. The basic concept of ferromagnetic resonance (FMR) where the precessional motion of the magnetization is excited resonantly, will be introduced in Section 2.3.3. One of the central topics of this thesis is the experimental determination of the magnetic anisotropy constants by means of ferromagnetic resonance measurements. Therefore, the aim of sections 2.3.3 and 2.3.4 is to derive a mathematic expression where the magnetic anisotropies constants enter the angle-dependent FMR equation.

2.3.1 Equation of motion

Consider the situation in Fig. 2.3(a), where the magnetization and the static effective field are initially aligned along the z-direction. When the magnetization vector is deflected from this equilibrium orientation, a torque \vec{T} is exerted which points perpendicular to magnetization and effective field direction:

$$\vec{T} = \mu_0 \vec{M} \times \vec{H}_{\text{eff}}. \quad (2.14)$$

This torque \vec{T} causes the precession of the magnetization around the equilibrium direction \vec{H}_{eff} . The temporal evolution of the magnetization is well described by the classical equation of motion, where the rate of change of angular momentum is equal to the torque acting on the angular momentum:

$$\frac{d\vec{M}}{dt} = -|\gamma|\vec{T} = -|\gamma|\mu_0 \cdot \vec{M} \times \vec{H}_{\text{eff}} \quad (2.15)$$

where $\gamma = \frac{g\mu_B}{\hbar}$ is the gyromagnetic ratio and the effective field \vec{H}_{eff} is derived from the free energy density Eq. 2.3 (cf. Section 2.2). Eq. 2.15 describes the resulting motion of the magnetization vector, as illustrated in Fig. 2.3(a).

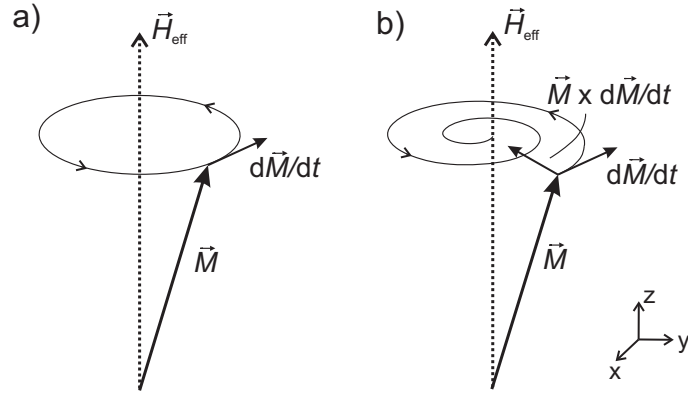


Figure 2.3: (a) Illustration of the precession of the magnetization around the effective field direction with constant cone angle. (b) With damping the tip of the magnetization vector follows a helical trace until the equilibrium orientation along \vec{H}_{eff} is reached.

2.3.2 The Landau-Lifshitz-Gilbert Equation

Equation 2.15 has no damping term. Hence, once \vec{M} is deflected from its equilibrium position, the precessional motion with constant cone angle would continue indefinitely. This behavior of course does not agree with experimental observations where \vec{M} returns to its equilibrium orientation after a few nanoseconds. The most frequently employed equation of motion which includes also damping is the phenomenological Landau-Lifshitz-Gilbert equation [17], which in contrast to the earlier Landau-Lifshitz-equation [18] provides physically correct solutions for both small and large damping factors:

$$\frac{d\vec{M}}{dt} = \underbrace{-|\gamma|\mu_0 \cdot \vec{M} \times \vec{H}_{\text{eff}}}_{\text{precession}} + \underbrace{\frac{\alpha}{M_S} \cdot \left(\vec{M} \times \frac{d\vec{M}}{dt} \right)}_{\text{damping}}, \quad (2.16)$$

where α is a phenomenological and intrinsic damping factor which is much smaller than one for most ferromagnetic materials. The first term of Eq. 2.16 is equal to Eq. 2.15 and represents the precessional motion of the magnetization vector. The second term describes the damping, adding a torque that pushes the magnetization back towards the effective field direction. As shown in Fig. 2.3(b) the resulting trajectory of the magnetization vector is helical. Note, that since the time derivative of the magnetization $\frac{d\vec{M}}{dt}$ enters the damping term, it represents a viscous, velocity (frequency)-dependent damping. Experimentally, it was found that this phenomenological description of the damping provides a correct description of the intrinsic damping.

2.3.3 Basic concept of ferromagnetic resonance

Ferromagnetic resonance (FMR) is a well established and important tool for characterizing magnetic samples. By performing angle- and frequency dependent measurements

a multitude of magnetic properties such as magnetic anisotropy, damping, g-factor, etc. can be determined [16]. In this section the basic concept of FMR will be introduced using a rather intuitive approach. A quantitative mathematic derivation of the resonance condition will be given in the subsequent Section 2.3.4.

Instead of tipping the magnetization out of its equilibrium direction by means of a short field pulse the magnetization can also be excited continuously. For this purpose, an alternating microwave field $\vec{h}(t)$ of frequency f is applied in a ferromagnetic resonance experiment and the magnetic sample is swept across the ferromagnetic resonance. This can be achieved by either sweeping the microwave frequency f or the external magnetic field H_0 . The external field provides an additional magnetic stiffness, i.e. the higher the external field the higher the frequency of the precessing magnetization. The term "stiffness" is used in analogy to a classical mechanical oscillator. The cone angles of the precessing magnetization reach a maximum when the excitation frequency f matches the eigenfrequency of the oscillator f_0 . Experimentally, the resonance is detected either indirectly by the absorption of microwave power or directly by measuring one of the components of the magnetization vector \vec{M} . Both measurement techniques will be discussed in Chapter 4.

So far, no magnetic anisotropies were considered in the equation of motion. In this case, without applied magnetic DC field the energy landscape is spherical, (cf. Fig. 2.2(a)), and the precession frequency f_0 is independent of the magnetization direction. Yet, the superposition of various magnetic anisotropies (cf. Section 2.2.3) can lead to an anisotropic energy landscape (e.g. Fig. 2.2(d)) with minima and maxima which are so called easy axes and hard axes of the magnetization, respectively. If the magnetization is aligned along an easy axis, it is in a state with high magnetic stiffness. Hence, the resonance frequency is large. In contrast when the magnetization is aligned along a hard axis, it can be more easily deflected since it is energetically more favorable to move towards an "easier" axis. The smaller magnetic stiffness leads to a smaller resonance frequency. When the microwave frequency is kept constant and the external field is swept, the magnetic field provides the additional magnetic stiffness. Consequently, when the magnetization is aligned along a hard axis, a larger external field is necessary to bring the sample into resonance.

Note, that these considerations are used only as an illustration. Actually, in the subsequent section it will be demonstrated that for small excursion of the magnetization from the equilibrium orientation, the resonance frequency is proportional to the curvature of the energy surface.

2.3.4 Ferromagnetic resonance condition

The condition for ferromagnetic resonance will be derived quantitatively using the so called 'macrospin'-approximation, where all spins are assumed to precess with the same amplitude and phase. Hence the contribution of the exchange energy can be neglected. The calculation of the resonance condition, without consideration of dynamic aspects such as damping, can be performed using a very simple and variational approach [19]. For small harmonic excursions of the magnetization from its equilibrium orientation, the

resonance frequency is determined by the second derivatives of the free energy density with respect to the spherical angles of the magnetization:

$$\left(\frac{\omega}{\gamma}\right)^2 = \frac{1}{M^2 \sin^2 \theta} \left(\frac{\partial^2 \varepsilon}{\partial \theta^2} \frac{\partial^2 \varepsilon}{\partial \varphi^2} - \left(\frac{\partial^2 \varepsilon}{\partial \varphi \partial \theta} \right)^2 \right). \quad (2.17)$$

Due to the presence of magnetic anisotropies the orientation of the magnetization (θ, φ) can deviate from the external field orientation (θ_H, φ_H) . The actual orientation of \vec{M} is found by minimizing the free energy density with respect to the spherical coordinates θ and φ :

$$\frac{\partial \varepsilon}{\partial \varphi} = 0, \quad \frac{\partial \varepsilon}{\partial \theta} = 0. \quad (2.18)$$

In the following the magnetic energy contributions for a thin magnetic film of tetragonal symmetry with an additional uniaxial in-plane anisotropy are considered (see Section 2.2). For parallel alignment of both magnetization and external field in the film plane ($\theta = \theta_H = 90^\circ$), the resulting resonance equation reads:

$$\left(\frac{\omega}{\gamma}\right)^2 = \mathfrak{B}_{\text{eff}} \cdot \mathfrak{H}_{\text{eff}} \quad (2.19)$$

$$\begin{aligned} \mathfrak{B}_{\text{eff}} &= \mu_0 H_0 \cos(\varphi - \varphi_H) + \mu_0 M_{\text{eff}} + \frac{K_{C\parallel}}{2M} (3 + \cos 4\varphi) + \frac{2K_{U\parallel}}{M} \sin^2(\varphi - \varphi_U), \\ \mathfrak{H}_{\text{eff}} &= \mu_0 H_0 \cos(\varphi - \varphi_H) + 2\frac{K_{C\parallel}}{M} \cos 4\varphi - \frac{2K_{U\parallel}}{M} \cos(2\varphi - 2\varphi_U). \end{aligned}$$

$\omega = 2\pi f$ is the angular frequency of the microwave field, γ is the gyromagnetic ratio and $\mu_0 M_{\text{eff}} = \mu_0 M - \frac{2K_{U\perp}}{M}$ is the effective magnetization including the demagnetization energy of a thin magnetic film and the perpendicular anisotropy $K_{U\perp}$.

2.3.5 Calculation of the FMR lineshape

This section addresses the calculation of the dynamic magnetic susceptibility. Based on the Landau-Lifshitz-Gilbert equation the shape of the FMR spectra including resonance position and linewidth will be derived. The calculation itself does not provide any novel physical insights and only the general ansatz and the main results will be discussed. A complete derivation can be found for instance in [20].

The dynamic magnetic susceptibility χ is related to the reaction of the magnetization to time-dependent fields. Starting point in the calculation is the LLG-equation which describes the damped precessional motion of the magnetization around the effective field direction. The effective field \vec{H}_{eff} can be derived from the free energy density ε (Eq. 2.3) and includes both the internal fields, such as anisotropy fields \vec{H}_{ani} , and demagnetizing fields \vec{H}_{dem} as well as external fields like the static DC field \vec{H}_0 and the microwave driving field \vec{h} :

$$\vec{H}_{\text{eff}} = \vec{H}_{\text{ani}} + \vec{H}_{\text{dem}} + \vec{H}_0 + \vec{h} \quad (2.20)$$

The calculation is executed in a coordinate system, where the x-direction lies along the static magnetization direction and the y-axis is aligned in the (001)-plane. The microwave field \vec{h} points along the y-axis. In this reference system the tip of the magnetization vector moves in the y-z-plane. The derivation of the resonance condition is performed for the so called in-plane configuration, where both \vec{H}_0 and \vec{M} are aligned in the film plane ($\theta_H = \theta = 90^\circ$).

For small cone angles of the precession, the dynamic components m_y , m_z are much smaller than the static magnetization M_S and one can use the following approximation:

$M_x = \sqrt{M_S^2 - m_y^2 - m_z^2} \approx M_S$, hence:

$$\vec{M}(t) = \begin{pmatrix} M_S \\ m_y(t) \\ m_z(t) \end{pmatrix}. \quad (2.21)$$

Since the microwave excitation has a sinusoidal time-dependence one can use the following ansatz for the time dependent magnetization components: $m_y, m_z \sim e^{i\omega t}$.

For small excitation fields h , linearization of the LLG-equation, where only terms to first order of m_y , m_z and h are considered, leads to two coupled equations for the dynamic components m_y and m_z :

$$i\frac{\omega}{\gamma}m_y + \left(\mathfrak{B}_{\text{eff}} + i\alpha\frac{\omega}{\gamma}\right)m_z = 0 \quad (2.22)$$

$$-i\frac{\omega}{\gamma}m_z + \left(\mathfrak{H}_{\text{eff}} + i\alpha\frac{\omega}{\gamma}\right)m_y = hM_S, \quad (2.23)$$

with $\mathfrak{B}_{\text{eff}}$ and $\mathfrak{H}_{\text{eff}}$ as defined in Eq. 2.19.

Solving Eq. 2.22 for m_z and inserting it into Eq. 2.23 leads to the dynamic magnetic susceptibility χ_y :

$$\chi_y = \frac{m_y}{h} = \frac{M_S \left(\mathfrak{B}_{\text{eff}} - i\alpha\frac{\omega}{\gamma}\right)}{\left(\mathfrak{B}_{\text{eff}} - i\alpha\frac{\omega}{\gamma}\right)\left(\mathfrak{H}_{\text{eff}} - i\alpha\frac{\omega}{\gamma}\right) - \left(\frac{\omega}{\gamma}\right)^2}. \quad (2.24)$$

When the sample undergoes resonance the precession angles and the absorption of microwaves reach a maximum. Mathematically this occurs when the imaginary part of the dynamic susceptibility χ_y has a maximum, i.e. the resonance takes place when the denominator of Eq. 2.24 is zero. For small damping one can set $\alpha = 0$ and the resonance condition reads:

$$\left(\frac{\omega}{\gamma}\right)^2 = \mathfrak{B}_{\text{eff}}\mathfrak{H}_{\text{eff}}. \quad (2.25)$$

Note that this is the same result as obtained by the simple calculation of the resonance condition (Eq. 2.19) with the second derivatives of the free energy density.

Finally, based on the dynamic susceptibility Eq. 2.24 the shape of the FMR spectra is addressed. This is necessary in order to determine resonance fields and linewidths by

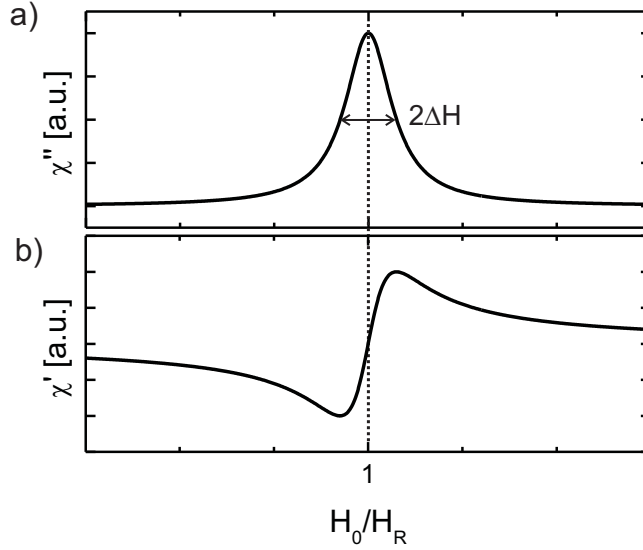


Figure 2.4: Illustration of imaginary part (a) and real part (b) of the dynamic magnetic susceptibility.

fitting the experimental FMR spectra. One can show that under certain conditions the FMR spectra have a Lorentzian shape [21]. For this purpose, the external static field H_0 which enters $\mathfrak{H}_{\text{eff}}$ and $\mathfrak{B}_{\text{eff}}$ in Eq. 2.24 is replaced by $H_R + \delta H$. For small damping $\alpha \ll 1$ the terms which are not linear in δH and α can be neglected and the susceptibility becomes

$$\chi_y = \left(\frac{M_S}{\mathfrak{H}_{\text{eff,R}} + \mathfrak{B}_{\text{eff,R}}} \right) \frac{B_R + \delta H - i\alpha \frac{\omega}{\gamma}}{\delta H - i\alpha \frac{\omega}{\gamma}}, \quad (2.26)$$

where both $\mathfrak{B}_{\text{eff,R}}$ and $\mathfrak{H}_{\text{eff,R}}$ have to be evaluated at $H_0 = H_R$.

Finally, real and imaginary parts of the susceptibility are obtained by multiplication with $\delta H + i\alpha \frac{\omega}{\gamma}$. By using $\delta H = H_0 - H_R$, one finds:

$$\begin{aligned} \text{Im}[\chi_y] &= \frac{M_S}{\mathfrak{H}_{\text{eff,R}} + \mathfrak{B}_{\text{eff,R}}} \cdot \frac{\Delta H}{\Delta H^2 + (H_0 - H_R)^2} \\ \text{Re}[\chi_y] &= \frac{M_S}{\mathfrak{H}_{\text{eff,R}} + \mathfrak{B}_{\text{eff,R}}} \cdot \frac{H_0 - H_R}{\Delta H^2 + (H_0 - H_R)^2} \end{aligned} \quad (2.27)$$

Both real and imaginary parts of the susceptibility are illustrated in Fig. 2.4. The imaginary part represents a symmetric Lorentzian line with a maximum at $H_0 = H_R$ and a half-width at half maximum linewidth (HWHM) $\Delta H = \alpha \frac{\omega}{\gamma}$. The real part is antisymmetric with respect to the resonance field H_R and has a zero-crossing at $H_0 = H_R$. In general, when the magnetization is probed with a certain phase correlation with respect to the microwave excitation, the FMR spectrum does not correspond to the imaginary part of the susceptibility, but represents a mixture of imaginary and real parts. For details on such time-resolved techniques, refer to Section 4.4. Hence the actual fit function is given by an asymmetric Lorentzian function:

$$y(H) = A \cdot \frac{\Delta H \cos \epsilon + (H_0 - H_R) \sin \epsilon}{\Delta H^2 + (H_0 - H_R)^2}, \quad (2.28)$$

where ϵ is the phase which mixes real and imaginary parts of the dynamic susceptibility. Finally, in conventional FMR absorption measurements the external field H_0 is modulated and the fit function is then given by the derivative of Eq. 2.28 with respect to H_0 :

$$y'(H) = \frac{dy}{dH} = A \cdot \frac{-2(H_0 - H_R)\Delta H \cos \epsilon - [\Delta H^2 - (H_0 - H_R)^2] \sin \epsilon}{[\Delta H^2 + (H_0 - H_R)^2]^2}. \quad (2.29)$$

3 Structural and magnetic properties of (Ga,Mn)As

(Ga,Mn)As is the most intensively studied material in the class of so called **Diluted Magnetic Semiconductors** (DMS). The basic idea behind these materials is to introduce a small amount of magnetic ions (e.g. Mn) in a semiconducting host material (e.g. GaAs), in order to induce ferromagnetic behavior. For applications, the ultimate goal is a diluted magnetic semiconductor with a ferromagnetic transition temperature above room temperature. In the case of GaAs, the typically applied growth temperature of $\approx 600^\circ\text{C}$, which ensures high crystalline quality, only allows to incorporate a very small amount of transition metal atoms such as Mn ($x \approx 0.01\%$). Higher doping concentrations lead to the formation of a second ferromagnetic phase, i.e. MnAs-clusters which are embedded in the GaAs matrix. This solubility limit was circumvented by growing the films at much lower temperatures in the range $\approx 200 - 270^\circ\text{C}$, where the formation of the MnAs clusters is inhibited for larger Mn-concentrations of up to $\sim 10\%$. In this way, (Ga,Mn)As films with ferromagnetic properties at low temperatures could be realized for the first time in 1996 [3]. Yet, the lower growth temperatures have negative effects on the sample quality which is expressed by a large number of point defects leading to a degradation of the ferromagnetic properties. By carrying out a post-growth annealing at temperatures slightly below the growth temperatures ($\approx 160 - 200^\circ\text{C}$), the defects can be partially removed. This is reflected by an increase of carrier concentrations and Curie temperatures [22–24]. Currently, the highest Curie temperatures that are realized are in the range of $T_C \approx 185 - 190\text{ K}$ [5,6]. These temperatures are achieved only in very thin (Ga,Mn)As films with Mn-concentrations of $x > 10\%$ and by additional optimized annealing treatment.

In the subsequent section, the structural properties of (Ga,Mn)As films will be discussed. In Section 3.2, the mean-field Zener model, a very successful theory allowing to describe many ferromagnetic properties of (Ga,Mn)As will be outlined. Finally, in Section 3.3 the origin of the magnetic anisotropies will be addressed. This chapter makes no claim to completeness, only the basic properties of (Ga,Mn)As will be introduced. For a more detailed discussion of the theory of ferromagnetic (III,Mn)V semiconductors refer to Jungwirth al. [25], reviews of recent experimental results are given in Refs. [26, 27].

3.1 Structural properties of (Ga,Mn)As films

GaAs crystallizes in a zinc-blende crystal structure, which is composed of two interpenetrating fcc (face-centered cubic) sublattices of the elements gallium and arsenide. The

individual sublattices are shifted by $1/4$ of the volume diagonal with respect to each other. In (Ga,Mn)As a small amount of the Ga-atoms (typically $x = 2 - 8\%$) is substituted by Mn-atoms (Mn_{Ga}). In addition, the non-equilibrium growth conditions at low temperatures lead to point defects such as Mn-interstitials (Mn_{I}) or As antisites (As_{Ga}). These common defects in (Ga,Mn)As will be discussed in the subsequent section.

In order to understand the influence of substitutional Mn-atoms on the electronic and magnetic properties, it is necessary to consider the electronic configuration of the individual isolated atoms: Ga [Ar] $3d^{10}4s^2p^1$, As [Ar] $3d^{10}4s^2p^3$, Mn [Ar] $3d^54s^2$. When Mn occupies a Ga site, it acts as an acceptor (provides one hole), because one 4p electron is missing. In addition, according to Hund's rules, the total spin in the half-filled 3d shell has to be maximized, leading to the spin $S = 5/2$. Experimentally, it was found, that for (Ga,Mn)As samples with metallic conductivity ($x > 2\%$) the ground state of the Mn-atoms corresponds to a $A^-(d^5)$ configuration which represents a negatively charged acceptor center with localized spin $S = 5/2$ and a hole which is only weakly bound to the Mn-atom [28]. These weakly bound holes mediate the ferromagnetic order between the localized Mn-spins, see the discussion in Section 3.2.

3.1.1 Point defects

Mn-Interstitials

The doping of GaAs with Mn does not only lead to substitutional positions Mn_{Ga} , where the Mn-atom occupies a Ga site, but also to interstitial positions (Mn_{I}), where Mn serves as a double donor (provides two electrons) and leads to a reduction of the hole concentration. Since the ferromagnetic order in (Ga,Mn)As is mediated by itinerant holes, this hole compensation also reduces the ferromagnetic transition temperature. In addition, the super-exchange interaction leads to an antiferromagnetic coupling between neighboring Mn_{Ga} and Mn_{I} , reducing the saturation magnetization [29]. Because the interstitial Mn_{I} ions are only weakly bound, post-growth annealing at temperatures slightly below the LT-MBE growth temperatures ($150 - 200^\circ\text{C}$) can lead to a significant reduction of Mn_{I} and thus strongly increase both hole concentration and magnetization. Experimental studies using Auger surface analysis demonstrated that the highly mobile Mn_{I} diffuses towards the (Ga,Mn)As film surface [24], where it is passivated by oxidation, nitration or formation of MnAs. This annealing treatment can lead to significant improvements of the magnetic properties, such as increase of the Curie temperature and magnetization, and enhancement of the sample homogeneity (confirmed by FMR [30]). The so far highest Curie temperatures of 185 K and 191 K were reached in well prepared and optimally annealed (Ga,Mn)As samples with very high Mn-concentrations of $x > 10\%$ [5, 6].

As-antisites

It is well established, that the low temperature growth of GaAs leads to the formation of a large number of As antisites As_{Ga} , where an As-atom occupies a Ga site. Because the

MBE growth of (Ga,Mn)As is performed at low temperatures one can assume that these defects also occur in (Ga,Mn)As. In addition, the As overpressure, which is applied to ensure the two dimensional, layer-by-layer growth of (Ga,Mn)As, can lead to an increase of the number of As_{Ga} . Because of the electronic configurations of As and Ga, As_{Ga} act as double donors and compensate the holes of two substitutional Mn atoms, leading to a decrease of T_C . As_{Ga} antisites are very stable and cannot be removed by a post-growth annealing process at typical temperatures of $150^\circ\text{C} - 250^\circ\text{C}$. Higher annealing temperatures would lead to the formation of MnAs clusters. For typical growth temperatures of $200^\circ\text{C} - 250^\circ\text{C}$ the concentration of As_{Ga} antisites is in the range of $y = 10^{19} - 10^{20} \text{cm}^{-3}$ [31].

Apart from these point defects, there are also other types of defects, such as Mn-Mn-clusters, Ga vacancies, etc. Yet, these defects are considered to have only relatively low concentrations and therefore should have no significant influence on the electronic and magnetic properties of (Ga,Mn)As.

3.1.2 Lattice constant

(Ga,Mn)As films can only be grown on appropriate substrates, such as GaAs(001) or (Ga,In)As, therefore one never deals with the properties of the 'bulk' material. As an example, x-ray diffraction measurements demonstrate that the out-of-plane lattice constants of otherwise identical (Ga,Mn)As films depend sensitively on the lattice constants a_0 of the underlying substrate [32]. The reason is the lattice mismatch between the (Ga,Mn)As film and the substrate $\Delta a = a_0 - a_{\text{rel}}$, where a_{rel} is the hypothetical relaxed lattice constant of (Ga,Mn)As. Because of the non-equilibrium growth conditions at relatively low temperatures, the in-plane lattice constant a_{\parallel} is locked to that of the substrate a_0 and the film is either under tensile or compressive strain (Fig. 3.1). It was found that even films with thicknesses of several micrometers are uniformly strained [33]. This is a consequence of the low temperature growth which inhibits the formation of dislocations or other defects. This compression (expansion) of the (Ga,Mn)As lattice in the film plane causes an expansion (compression) of the lattice in growth direction. Therefore, the in-plane lattice constant of (Ga,Mn)As films is smaller than the relaxed lattice constant of the film, which in turn is smaller than the out-of-plane lattice constant:

$$a_{\parallel} = a_0 < a_{\text{rel}} < a_{\perp}.$$

Whether the (Ga,Mn)As film is under compressive or tensile strain depends on the relaxed lattice constant of (Ga,Mn)As and on the lattice constant of the substrate. Due to the similar atomic radii of Mn ($R = 1.17\text{\AA}$) and Ga ($R = 1.25\text{\AA}$), one would expect only a weak dependence (decrease) of the relaxed lattice constant a_{rel} with increasing concentration of substitutional Mn_{Ga} (x_i). Density-functional theory calculations [34] predict a significant increase of the lattice constant with increasing concentration x_i of Mn_{I} and concentration y of As_{Ga} , following the law:

$$a_{\text{rel}}(x_s, x_i, y) = a_0 - 0.05x_s + 0.48x_i + 0.46y [\text{\AA}] \quad (3.1)$$

where a_0 is the lattice constant of undoped GaAs. Experimental studies, using as-grown and annealed samples have confirmed that the lattice constant in (Ga,Mn)As in-

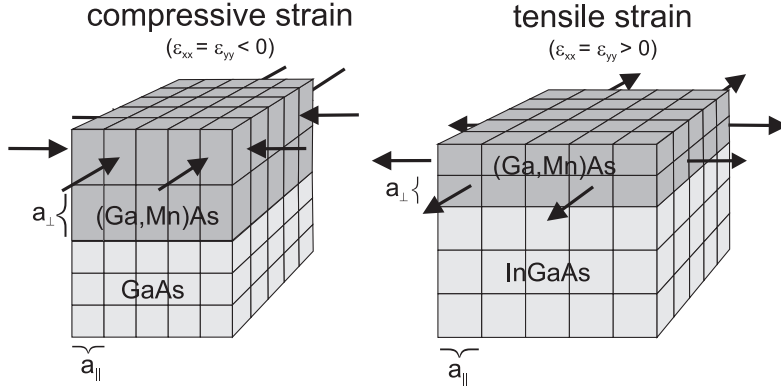


Figure 3.1: Schematic illustration of the biaxial strain on the (Ga,Mn)As lattice. The strain direction is indicated by the arrows. (a) (Ga,Mn)As grown on a GaAs(001) substrate is under compressive strain ($a_{rel} > a_0$). (b) (Ga,Mn)As grown on a (Ga,In)As(001) substrate is under tensile strain ($a_{rel} < a_0$).

creases with increasing concentration of Mn_I and As_{Ga} [35]. Also a reduction of a_{\perp} after annealing was found in x-ray diffraction measurements, which can be ascribed to the out-diffusion of Mn_I [35]. However, the theory seems to underestimate the influence of substitutional Mn_{Ga} on the lattice constant. Although it is very difficult to determine the individual concentrations of substitutional Mn and point defects experimentally, the findings hint to a much larger lattice expansion due to substitutional Mn_{Ga} than due to Mn_I or As_{Ga} , in disagreement with the theoretical predictions [36].

The strain effects in films can be described by the strain tensor $\hat{\epsilon}$, which relates the lattice vector \vec{r}' in the strained (tetragonal) lattice system to the vector \vec{r} of the fully relaxed (cubic) lattice: $\vec{r}' = \vec{r} + \hat{\epsilon}\vec{r}$. For a biaxially strained film the strain tensor reads [37]:

$$\hat{\epsilon} = \begin{pmatrix} e_{xx} & 0 & 0 \\ 0 & e_{yy} & 0 \\ 0 & 0 & e_{zz} \end{pmatrix} = e_0 \begin{pmatrix} 1 & 0 & 0 \\ 0 & 1 & 0 \\ 0 & 0 & -2c_{12}/c_{11} \end{pmatrix}, \quad (3.2)$$

where $e_0 = \Delta a/a_0$ and c_{12} and c_{11} are the elastic moduli of (Ga,Mn)As, which are usually assumed to agree with those of GaAs. All studied films were grown on GaAs(001) substrates, which for a typical Mn-concentration $x = 6\%$ leads to a compressive strain $e_0 \approx 0.2\%$ [38, 39].

In narrow lithographically defined (Ga,Mn)As bars the compressive strain can be partially relaxed. In order to account for these relaxation effects, the strain tensor has to be modified. For an infinite long bar of width w and thickness t oriented along the y-direction, the strain tensor is given by [40]:

$$\hat{\epsilon} = e_0 \begin{pmatrix} -\rho + 1 & 0 & 0 \\ 0 & 1 & 0 \\ 0 & 0 & c_{12}/c_{11}(\rho - 2) \end{pmatrix}, \quad (3.3)$$

where ρ quantifies the lattice relaxation in the transverse direction of the stripe. Only for very narrow stripes ($t/w \gg 1$) complete strain relaxation is obtained ($\rho = 1$). In a

realistic stripe with finite width w the relaxation varies across the stripe. The actual strain profile $\rho(x)$ can be simulated using finite element simulations by minimizing the strain energy [11,40]. More details concerning these relaxation effects and their influence on the magnetic anisotropies will be presented in Chapter 6.

3.2 Ferromagnetism in (Ga,Mn)As

This section addresses the origin of the ferromagnetic order in zinc-blende diluted magnetic semiconductors, such as (Ga,Mn)As. The most established and successful theory for diluted magnetic semiconductors, the mean field Zener model will be outlined in the subsequent section. The interested reader can find a very extensive overview of various theories on diluted magnetic (III,Mn)V semiconductors in Ref. [25].

Due to the low doping concentrations of GaAs with Mn atoms on the order of a few percent, the average distance between substitutional Mn_{Ga} atoms in (Ga,Mn)As is relatively large. Therefore, the overlap of the wavefunctions of neighboring Mn atoms is too small for a direct exchange interaction between the localized Mn spins. However, the interstitial Mn atoms do not only carry a localized spin $S=5/2$ but also provide an itinerant hole. Various experiments have shown that the ferromagnetic order in (Ga,Mn)As is mediated by these weakly bound or delocalized holes. As an example, it was demonstrated, that the magnetic properties such as Curie temperature or magnetic anisotropies can be manipulated by changing the hole concentration with electric fields or illumination with light [7, 8]. It was also found, that the ferromagnetic order is destroyed in hydrogen-passivated samples, when the concentration of holes diminishes [41].

Hence, the ferromagnetic order between localized Mn spins in (Ga,Mn)As is caused by an indirect exchange interaction mediated by the itinerant holes, the so called RKKY interaction. The interaction can be illustrated as follows: When a magnetic impurity atom is introduced in a metal, the free itinerant carriers try to shield the spin of this impurity atom. Therefore, the carriers around the magnetic impurity atom become spin-polarized. A second magnetic impurity atom within the range of this spin-polarization aligns its spin in order to minimize the exchange energy. Hence, an indirect exchange coupling is induced between the localized spins \vec{S}_i and \vec{S}_j of the two impurity atoms whose Hamiltonian reads [14]:

$$H_{RKKY} = -J_{ij}(r_{ij})\vec{S}_i\vec{S}_j \quad (3.4)$$

where the exchange integral $J_{ij}(r_{ij})$ depends on the distance r_{ij} between neighboring impurity atoms. For larger distances ($r_{ij} \gg k_F^{-1}$), it has the form [14]:

$$J_{ij}(r_{ij}) \propto \frac{\cos(2k_F r_{ij})}{r_{ij}^3}, \quad (3.5)$$

where k_F is the Fermi wavevector. J_{ij} shows a damped oscillatory behavior, with increasing distance r_{ij} the sign switches between positive (ferromagnetic coupling) and negative (antiferromagnetic coupling). In addition, the interaction is long range and decreases

with $1/r_{ij}^3$. In (Ga,Mn)As films the hole concentration p is smaller than the concentration of substitutional Mn x_i due to hole compensating defects (see Section 3.1.1). Under the condition $p/x_i \ll 1$ the coupling between the Mn-spins is ferromagnetic and the oscillating character of the RKKY interaction does not become apparent in (Ga,Mn)As [37]. It is however important to note that the distance of neighboring Mn atoms is not constant because they are randomly distributed over the GaAs crystal. Hence, an antiferromagnetic coupling between two Mn spins can exist locally, although the long range magnetic order is ferromagnetic.

3.2.1 Mean field Zener model

The Zener model which was initially proposed by Zener in 1951 [42] describes the indirect exchange coupling between localized spins via itinerant carriers. It does not allow to explain certain properties of conventional ferromagnetic metals, such as the oscillating character of the exchange interaction. Nevertheless, it was demonstrated that a mean field approximation of the Zener model provides a good description of various properties of diluted magnetic semiconductors such as (Ga,Mn)As [37, 43, 44]. Such a model was initially proposed by Dietl et al. [43] and extended in Refs. [37, 44]. It has allowed to determine various parameters such as Curie temperature, magnetization and magnetic anisotropies quantitatively. In this model, the magnetization of the localized Mn-spins \vec{M} is calculated by minimizing the free energy functional $F[\vec{M}]$. The free energy is obtained by diagonalizing the Hamiltonian H which contains various contributions:

$$H = H_{pd} + H_{KL} + H_{str} \quad (3.6)$$

The first term represents the p-d exchange interaction, which is caused by the hybridization of p-like valence states and local Mn d shells. In the mean field approximation, it is assumed that the effect of the localized Mn spins on the holes can be described as an effective field, which is proportional to the magnetization $\vec{M}(\vec{r})$ of the localized spins. The resulting interaction between the spin of the holes \vec{s} and the magnetization is described by the Hamiltonian [37]:

$$H_{pd} = \beta \vec{s} \cdot \vec{M}(\vec{r}) / (g\mu_B) \quad (3.7)$$

Since the ferromagnetic order is mediated by the itinerant holes it is essential to consider the complex valence band structure of the holes. The second term H_{KL} represents the 6×6 Kohn-Luttinger Hamiltonian taking into account the first six valence bands of pure undoped GaAs. In the $\vec{k} \cdot \vec{p}$ approximation the valence bands are only treated near the Γ point ($\vec{k} = 0$). The spin-orbit interaction between angular momentum and spin in the valence bands is included by the spin-orbit split off bands.

Finally, the lattice strain, which is generated by the lattice mismatch of the (Ga,Mn)As film and the substrate (cf. Section 3.1.2) is taken into account by means of the strain Hamiltonian H_{str} . Although the strain has no significant effect on the Curie temperature [37], it induces a very pronounced perpendicular magnetic anisotropy. The consideration of the strain has allowed to calculate the sign, magnitude and temperature

dependence of this perpendicular magnetic anisotropy, in good agreement with experimental results (cf. Section 3.3.2). Explicit forms of the individual Hamiltonians and the procedure which serves to derive various magnetic and thermodynamic parameters are given in Ref. [37].

Within a two-band mean-field model [45], one finds the following relation between Curie temperature and Mn- and hole concentrations:

$$T_C \propto x_i p^{1/3}. \quad (3.8)$$

In order to achieve high Curie temperatures, it is necessary to realize both a high concentration of substitutional Mn atoms and holes. However, (Ga,Mn)As films with higher Mn-concentrations have to be grown at lower temperatures in order to ensure a two-dimensional epitaxial growth. At these lower growth temperatures a larger number of hole compensating defects such as As antisites (As_{Ga}) are generated, which cannot be removed by post-growth annealing procedures. This technical drawback currently limits the Curie temperature of (Ga,Mn)As to about $T_C \approx 190$ K [5, 6].

3.3 Magneto-crystalline anisotropies

Magneto-crystalline anisotropies reflect the dependence of the free energy on the direction of the magnetization with respect to the crystallographic axes. In conventional metallic ferromagnets, magneto-crystalline anisotropies are a consequence of the interaction between orbital momentum and spin of the magnetic electrons. In (Ga,Mn)As the Mn^{2+} acceptors that carry the localized spin $S = 5/2$ have a d^5 configuration, hence the half filled d-shell has zero orbital momentum ($L=0$). Therefore, the spin-orbit interaction of the localized d-electrons cannot cause the very pronounced magneto-crystalline anisotropies in (Ga,Mn)As. However, since the exchange interaction in (Ga,Mn)As is mediated by holes, which have nonzero orbital moment, the magneto-crystalline anisotropies in (Ga,Mn)As are a consequence of the strong spin-orbit coupling in the valence bands. Experimentally, in (Ga,Mn)As on GaAs(001)-substrates various magnetic anisotropies are observed:

3.3.1 Cubic anisotropy

The magnetic anisotropies reflect the symmetry of the anisotropic Fermi surface of the holes which in turn reflects the symmetry of the zinc-blende crystal structure. Hence, in the case of completely unstrained (Ga,Mn)As films, one would expect only a cubic anisotropy K_C with easy axes along the $\langle 100 \rangle$ or $\langle 110 \rangle$ directions. This behavior was also theoretically predicted in the mean field calculations of Dietl et al. [37], where the direction of the easy axes depends on the occupation of the hole subbands (and thus the hole concentration) and the spin splitting parameter. In mean-field theory, the easy axis orientation should fluctuate between $\langle 100 \rangle$ and $\langle 110 \rangle$ as a function of the hole concentration. However, in (Ga,Mn)As a cubic anisotropy with easy axes along $\langle 110 \rangle$ has not been observed experimentally so far.

3.3.2 Perpendicular anisotropy

The lattice mismatch between the substrate and the (Ga,Mn)As film Δa (cf. Section 3.1.2) induces a biaxial strain $\varepsilon_{xx} = \varepsilon_{yy} = \Delta a/a_0$ in the film plane. This strain breaks the cubic crystal symmetry, leading to a uniaxial magnetic anisotropy $K_{U\perp}$ perpendicular to the film plane. In the case of moderate Mn-doping ($> 2\%$), the strain direction (either compressive or tensile) determines the sign of this anisotropy [32, 46]. These experimental observations are also reproduced theoretically in the mean-field calculations of Dietl et al. [37] and Abolfath et al. [44], where the biaxial strain splits the heavy and light hole valence bands. Experimentally [32], it was found that the magnitude and the sign of this anisotropy in (Ga,Mn)As can be adjusted continuously by using $\text{In}_y\text{Ga}_{1-y}\text{As}$ buffer layers, where the In-concentration y determines the lattice constant of the buffer layer. All films studied in the course of this thesis have a Mn-concentration of more than 5% and were grown on GaAs(001) substrates leading to a compressive strain $\varepsilon_{xx} \approx -0.2\%$ and a perpendicular anisotropy with its hard axis along the growth direction. Khazen et al. [38] have performed systematic FMR studies of the magnetic anisotropies for films with constant Mn-concentration but various hole concentrations. It was found that the perpendicular anisotropy constant is proportional to both biaxial strain ε_{xx} and hole concentration p :

$$K_{U\perp} \propto \varepsilon_{xx}p. \quad (3.9)$$

It is important to note, that the tetragonal distortion of the crystal also leads to a splitting of the cubic anisotropy into in-plane ($K_{C\parallel}$) and out-of-plane ($K_{C\perp}$) components. For zero strain $\varepsilon_{xx} = 0$, $K_{C\perp}$ and $K_{C\parallel}$ would assume the same value. Similar values of $K_{C\perp}$ and $K_{C\parallel}$ were actually observed in FMR studies of samples with low Mn-concentration ($x = 0.02$) and consequently small biaxial strain ε_{xx} [26]. For average Mn- and hole concentrations, $K_{C\perp}$ is however overshadowed by the much larger value of the perpendicular uniaxial anisotropy $K_{U\perp}$ [38], leading to a hard axis along the growth direction.

3.3.3 Uniaxial in-plane anisotropy

Experimentally, also a uniaxial magnetic anisotropy in the film plane $K_{U\parallel}$ with an easy axis either along the [110] or [1-10] direction is frequently observed in (Ga,Mn)As [30, 33, 47] which is not expected in a crystal with tetragonal symmetry. So far, the physical origin of $K_{U\parallel}$ is controversially discussed in the literature [33, 47]. Measurements of films with thicknesses in the micrometer range [33] have demonstrated that this anisotropy occurs also in thick films, excluding that the anisotropy results solely from interface or surface effects. This strongly suggests a mechanism in the "bulk" of the (Ga,Mn)As film. In SQUID measurements [47] it was demonstrated that this uniaxial anisotropy remains unchanged when the surface layer is etched away. This rules out any influence of surface-accumulated Mn, which might be generated during the growth or annealing process. In Ref. [47], it was suggested that a trigonal distortion ε_{xy} in the film plane causes this

uniaxial anisotropy. The magnitude of $K_{U\parallel}$ can be explained theoretically in the mean-field Zener model when assuming an additional trigonal distortion of $\varepsilon_{xy} = 0.01 - 0.05\%$. However, an experimental evidence of this in-plane strain is still missing and the explanation of the microscopic origin of this anisotropy is still unclear. In Section 6.5 lithographically defined circular (Ga,Mn)As elements are investigated in order to follow up on the question whether this anisotropy is caused by such an intrinsic strain in the film plane or not.

4 Experimental techniques

The experimental techniques which were mainly employed in the course of this thesis are based on an optical detection of the magnetization. The underlying physical effect, the magneto-optical Kerr-effect will be introduced in Section 4.1. Time-resolved measurements of the magnetization in the femtosecond to picosecond time range are based on a so called stroboscopic pump-probe technique. The general concept of such a technique will be explained in Section 4.2. For the local determination of the magnetic anisotropies in small (Ga,Mn)As structures and for the investigation of ultrafast magnetic processes in (Ga,Mn)As, a novel low-temperature scanning Kerr microscopy setup was developed and assembled. The basic components of this setup, such as microscope cryostat, and rotatable external magnetic field assembly will be addressed in sections 4.3.1 and 4.3.2. The individual measurement techniques, ferromagnetic resonance scanning Kerr microscopy and all-optical pump-probe technique will be described separately in Section 4.4 and Section 4.5, respectively. Finally, superconducting quantum interference device (SQUID) measurements were performed in order to determine the temperature dependence of the magnetization. A very detailed description of this technique can be found in the PhD-theses of M. Sperl [48] and W. Kipferl [49].

4.1 Magneto-optic Kerr effect

In general, magneto-optic effects occur when polarized light interacts with magnetized media. In the following, only the magneto-optic Kerr effect (MOKE) will be discussed, where the polarization or intensity of linearly polarized light is changed upon reflection from a magnetic material. Although the magneto-optic Kerr effect is a quantum-mechanical phenomenon, the effect can be understood qualitatively from a classical point of view [50]. The field vector of the incident light \vec{E} induces forced oscillations of the electrons inside the magnetic material along the E-field direction. This motion of the electrons leads to radiation of an electromagnetic wave with unchanged field direction \vec{E}_N compared to the incident light wave. In addition, due to the magnetization \vec{M} , the electrons inside the magnetic material experience a magnetic field. The resulting Lorentz-force leads to an additional component of the motion \vec{v}_{Lor} which is aligned perpendicular with respect to the magnetization and the electric field direction: $\vec{v}_{Lor} \propto \vec{M} \times \vec{E}$. This additional small oscillatory component leads to the emission of linearly polarized light which is superimposed to the regularly reflected light, leading to a rotation of the polarization. A phase lag between different polarization components induces also ellipticity of the polarization in the reflected beam.

Depending on the relative orientation of the plane of incidence, polarization and mag-

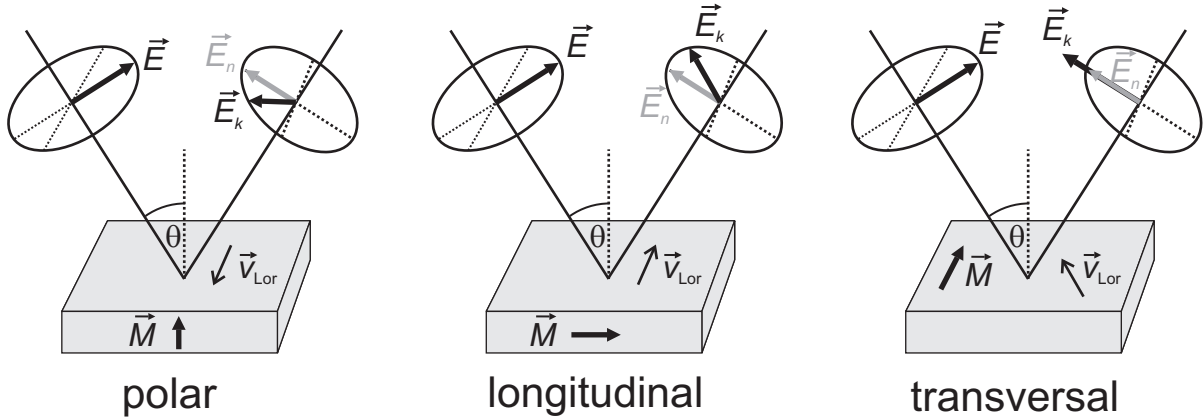


Figure 4.1: Illustration of different configurations for the magneto-optic Kerr effect (MOKE). \vec{M} indicates the magnetization. \vec{E} and \vec{E}_n denote the incident and regularly reflected electric fields orientations, respectively. The change of the polarization or intensity of the reflected light (field direction \vec{E}_K) is a consequence of the interaction of the oscillating electrons inside the material with the magnetization.

netization, different Kerr configurations can be distinguished, see Fig. 4.1.

- In the polar Kerr configuration the magnetization is orientated perpendicular to the sample surface. The rotation of the polarization reaches a maximum for perpendicular incidence ($\theta = 0^\circ$).
- In the longitudinal configuration, the magnetization lies in the sample plane and is parallel to the plane of incidence. For $\theta = 0^\circ$ the longitudinal effect vanishes. The sense of rotation changes sign when the polarization of the incident light is switched from parallel to perpendicular to the plane of incidence. These cases are usually referred to as 'longitudinal \parallel ' and 'longitudinal \perp ' Kerr effects [50].
- In the transverse configuration, the magnetization lies in the film plane, but is aligned perpendicular to the plane of incidence. The polarization of the reflected light remains unchanged, only the intensity of the reflected light changes. The effect vanishes for $\theta = 0^\circ$ and if the polarization is oriented perpendicular to the plane of incidence (s-pol).

It is important to note, that for arbitrary orientations of the magnetization vector the resulting effect is a mixture of different Kerr configurations.

The Kerr signal does not represent the bulk properties of the magnetic material but originates only from a surface layer, whose thickness is determined by the skin depth of the light. While for metals the skin depth is on the order of ~ 10 nm in the visible spectral range, the absorption in (Ga,Mn)As is much lower [37], so that films with thicknesses of several tenths of nanometers are probed uniformly. Since the size of the magneto-optic Kerr effect depends on the exchange and spin-orbit coupling of the material, it does not scale linearly with the magnitude of the magnetization. As an example,

in (Ga,Mn)As a relatively large Kerr rotation ($\sim 0.3^\circ$ for saturated magnetization) was found by Lang et al. [51], although the magnetization of (Ga,Mn)As is typically two orders of magnitude smaller than in the 3d-ferromagnets. Lang et al. [51] have also observed a complex wavelength dependence of the polar Kerr rotation in (Ga,Mn)As, with distinct minima and maxima. These Kerr spectra differed also significantly for two films with different Mn-concentrations. In the present thesis, it was found, that in (Ga,Mn)As films with a Mn-concentration $x = 0.06$ and average hole concentrations $p = 2 - 4 \times 10^{20} \text{ cm}^{-3}$, the Kerr rotation at $\lambda \sim 400 \text{ nm}$ is by a factor of 2-3 smaller than at $\lambda \sim 800 \text{ nm}$. Therefore, for some measurements, which did not require the full spatial resolution, the 800 nm beam was used to probe the magnetization.

4.2 Stroboscopic pump-probe technique

Pump-probe experiments are the most important tools to investigate physical processes which are below the time resolution of conventional measurement techniques. The underlying idea is to use a pump event which triggers a certain physical process and a probe event which takes a "snapshot" of the process at a certain time after the excitation. The time resolution in such an experiment is only limited by the duration of pump and probe events.

In the present experiments short light pulses in the visible spectral range act as pump and probe events. A commercially available pulsed Ti:sapphire laser (a Coherent Mira 900 laser) was used which generates light pulses of $\sim 150 \text{ fs}$ duration at a repetition rate of 80 MHz and at a central wavelength $\sim 800 \text{ nm}$. This fundamental laser beam is split into two parts, which are referred to as pump and probe beams. The pump pulse triggers the experiment, for instance it launches the precessional motion of the magnetization by means of a short magnetic field pulse. In addition, the pump pulse can be used for the synchronization of a continuous excitation, such as microwave fields in the ferromagnetic resonance scanning Kerr microscopy technique. The probe pulse samples the state of the system after a certain time Δt which is determined by the time delay between pump and probe pulse. In the present experiments, the z-component of the magnetization is measured by means of the polar magneto-optic Kerr effect (MOKE). An opto-mechanical delay stage allows to adjust the optical path of the probe pulses Δs . The resulting time delay is then given by $\Delta t = \frac{\Delta s}{c}$, where c is the speed of light. As an example, the length of the used mechanical delay of $\Delta s = 0.52 \text{ m}$ is traveled by the probe pulses two times, which corresponds to a time delay of $\Delta t = 3.4 \text{ ns}$. The actual time resolution in the experiment is $\sim 300 \text{ fs}$; it is given by the convolution of pump and probe pulses at the sample position. The minimum step size of the mechanical delay of $1.25 \mu\text{m}$ which corresponds to a time step of only $\Delta t = \frac{2\Delta s}{c} \sim 8 \text{ fs}$ has no effect on the time resolution. A stroboscopic experiment is performed since the signal of a single probe event cannot be detected. In order to obtain a sufficient signal to noise ratio (SNR) the same experiment is typically repeated many million times. Thus, one has to maintain a fixed time correlation between the pump and probe events. In addition, for experiments with pulsed excitation, (e.g. all-optical pump probe technique) two essential conditions have to be

fulfilled so that this stroboscopic technique can be employed. First, it should be guaranteed that the relaxation of the system back into its initial ground state is completed before the next pump-probe experiment takes place. Due to the repetition rate of the laser of 80 MHz, this relaxation has to take place within 12.5 ns. Second, the response of the system to the pump event has to be reproducible. All stochastic processes, such as variations of the response due to slightly different experimental conditions average out and cannot be observed.

4.3 Components of the low-temperature time-resolved MOKE setup

First of all, the basic components of the newly developed low-temperature Kerr microscopy setup will be described.

4.3.1 Microscope cryostat

Due to the low Curie temperatures of the diluted magnetic semiconductor (Ga,Mn)As, the experiments are carried out in a temperature range from 4.2 K to 100 K in a He-flow microscope cryostat (modified Cryovac KONTI-Cryostat-Mikro). In order to minimize heat transfer from the ambient air to the sample, the cryostat is evacuated. The isolation vacuum of $< 1 \cdot 10^{-5}$ mbar is generated by a combination of rotary vane and turbomolecular pumps. Cold helium from a reservoir of liquid helium is transferred to the cryostat using a helium transfer line and pumping at the helium outlet of the cryostat. The helium flow and thus the sample temperature can be roughly set in a range of 4-40 K by using a needle-valve. In order to reach more stable and also higher sample temperatures the cryostat is equipped with an electrical heater. The exact cryostat temperature which is measured by means of a Si diode, is monitored and stabilized using an Oxford PID-temperature controller. The sample is glued to a copper sample holder using conductive silver which ensures good thermal contact. This sample holder also provides two high-frequency SMP-connectors and six electrical connections for DC measurements. The sample holder is mounted on top of the copper cold finger of the cryostat and the SMP-connectors are attached to semirigid coaxial cables which are accessible from the outside via custom-made feed-throughs. Optical access to the sample is provided through a 0.2 mm thick polarization-conserving glass window. Both the cryostat and the liquid helium dewar are mounted directly onto the optical table which is stabilized with an air cushioning system in order to minimize mechanical vibrations.

4.3.2 Magnetic DC field

Since magnetic anisotropies reflect the dependence of the free energy on the crystal directions or on the orientation in a macroscopic sample, the experimental determination of the anisotropy constants requires that either the sample or the magnetic bias field is rotatable. Because of the semi-rigid high-frequency connectors a rotation of the sample

is not possible. Therefore, a rotatable electromagnet was developed, which satisfies the experimental requirements of the low-temperature Kerr microscopy setup. The development resulted in a water-cooled electromagnet with yoke and pole-shoes made from soft iron and a gap of 22 mm. A maximum current of $I = 30$ A can be applied to each of the two coils (~ 200 windings) allowing to apply magnetic fields of up to 0.3 T. The magnet is mounted on a rotatable disk which is computer controlled and adjusted by a stepper motor; allowing the reproducible alignment of the field in any direction of the sample plane. The magnetic field value H_{pole} is measured by means of a Hall probe attached to one of the pole shoes of the magnet. The magnetic field at the sample position H_0 is then given by $H_0 = c \cdot H_{\text{pole}}$. The calibration factor c was determined by measuring the magnetic field at the sample position H_0 with a separate calibrated and temperature-stabilized Hall probe.

4.4 Ferromagnetic resonance scanning Kerr microscopy

Ferromagnetic resonance scanning Kerr microscopy (FMR-SKEM) combines two experimental techniques: angle-resolved ferromagnetic resonance (FMR) and time-resolved scanning Kerr microscopy (TR-SKEM). FMR-SKEM allows one to perform spatially and phase resolved measurements. Thus this technique can be used to image magnetic modes in confined magnetic structures [52–54] or to visualize local variations of the internal fields [54]. In FMR-SKEM microwave fields are used to excite the precessional motion of the magnetization, the perpendicular component of this motion is probed stroboscopically with a short laser light pulse by means of the polar magneto-optic Kerr effect. An illustration of the setup is shown in Fig. 4.3.

Since the application of a stroboscopic technique (cf. Section 4.2) requires that the excitation and the detection have a fixed phase correlation, the phase of the microwave field has to be synchronized to the laser probe pulses. For that purpose, the fundamental beam ($\lambda \sim 800$ nm, pulse length ~ 150 fs) of the Ti:Sapphire laser serves for the generation of synchronized microwaves. The optical path length of this beam is varied by means of an opto-mechanical delay line allowing one to measure the dynamic response of the magnetization at various phases of the excitation.

4.4.1 Excitation of the precessional motion

First, the excitation of the sample with microwave fields in the GHz range is described. The red beam is focussed onto a fast photodiode, where voltage pulses with a risetime on the order of 50 ps and the laser repetition rate $f = 80$ MHz are generated. A pulse generator is used to convert this signal into a regular square-wave signal. This rectangular 80 MHz signal is frequency-doubled to 160 MHz and amplified. A frequency mixer is used to apply a 180° phase modulation of the microwaves, i.e. the microwave phase is switched by 180° with a frequency of several kHz (cf. Fig. 4.2). This modulation allows lock-in detection of the Kerr signal. A comb generator is used to create higher harmonics of this 160 MHz fundamental signal. A certain microwave frequency (a multiple of the

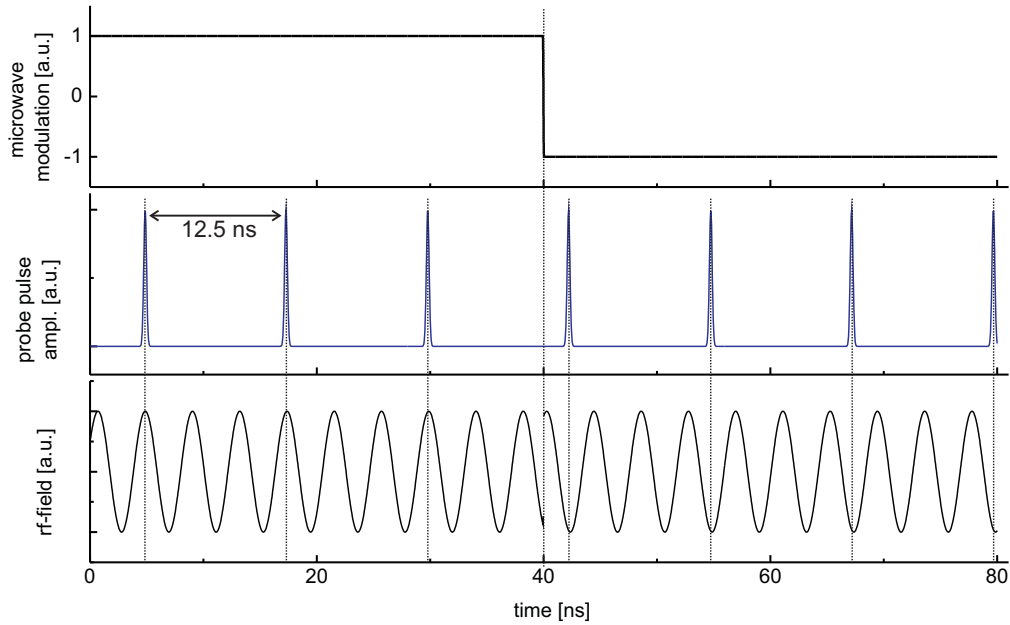


Figure 4.2: Synchronization between continuous microwave excitation and laser probe pulses. Due to the repetition rate of the laser, the magnetization is probed every 12.5 ns. The microwave phase is the same for each probe event. Phase modulation of the microwaves is performed with a low frequency in the kHz-range. Note that at $t = 40$ ns, the phase of the excitation field is switched by 180° .

160 MHz signal) can be selected using a yttrium iron garnet microwave filter (YIG). Finally, this rf-signal is amplified and transmitted to the coplanar waveguide of the sample inside the cryostat. In order to ensure both the excitation of the sample and the phase synchronization of the microwaves with the probe laser pulses the transmitted microwave signal is monitored using a 20 GHz sampling oscilloscope. The synchronization between excitation and probe pulses is shown schematically in Fig. 4.2. The microwave current through the waveguide leads to an alternating magnetic field \vec{h} which circulates around the conductors of the waveguide, see Fig. 4.3. At the position of the magnetic elements this microwave field is mostly oriented perpendicular to the sample plane (z-direction). The resulting torque on the magnetization $\vec{T} = \vec{M} \times \vec{h}$ excites the precessional motion. A detailed discussion of the characteristics of the employed waveguides, such as current densities and field profiles can be found in Appendix 8.3.

4.4.2 Scanning Kerr microscopy

The fundamental near infrared beam of the Ti:Sapphire laser ($\lambda \sim 800$ nm) is focussed into a lithium-borate crystal (LBO), where a small part of the beam is frequency doubled due to second harmonic generation. The frequency-doubled blue beam ($\lambda \sim 400$ nm) and the fundamental red beam are separated using a dichroic mirror. The dynamic response of the magnetization to the continuous microwave excitation is probed by the frequency doubled blue laser pulses by means of the polar magneto-optic Kerr effect. For this purpose, the blue beam is linearly polarized using a Glan-Thompson polarizer

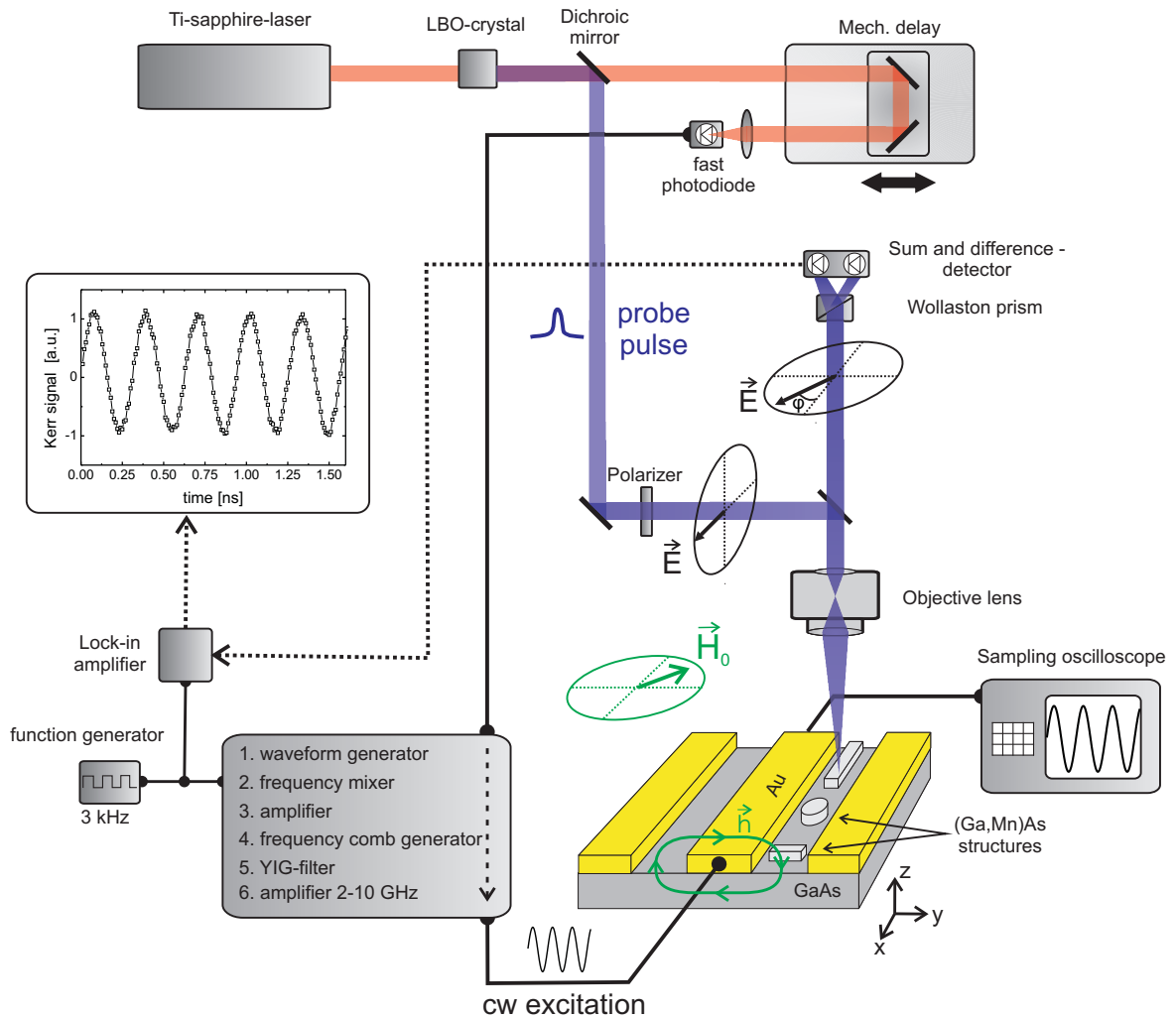


Figure 4.3: Illustration of the ferromagnetic resonance scanning Kerr microscopy setup. A part of the fundamental infrared beam of the Ti-Sapphire laser (~ 800 nm) is frequency doubled using a LBO crystal. This frequency doubled blue beam (~ 400 nm) probes the perpendicular magnetization component by means of the polar magneto-optic Kerr effect. The red laser pulses are delayed by means of a mechanical delay stage and focused onto a fast photodiode, which triggers the generation of phase-synchronized microwaves. For clarity reasons the individual components which are used for the microwave generation are combined in one unit. The microwave current passes through the coplanar waveguide structure of the sample, leading to an rf-magnetic field \vec{h} which excites the precessional motion of the magnetization. The transmission of the microwaves through the sample is monitored using a 20 GHz sampling oscilloscope. The sample is mounted on the cold finger of a He-flow cryostat allowing samples temperatures from 4 K to room temperature. The cryostat is placed on a piezo scanning stage which is used to scan the sample laterally under the fixed laser beam. Static magnetic fields \vec{H}_0 can be applied in any direction in the sample plane by using a rotatable electromagnet.

and focused onto the sample with a polarization conserving objective lens (numerical aperture $A_N = 0.6$). Since the probe beam has to pass the cryostat window an objective lens with adjustable cover glass correction was used. The rotation of the polarization of the reflected light is analyzed by means of a polarization sensitive detector. This detector consists of a Wollaston prism which splits the beam into two beams with orthogonal polarization direction whose intensities are measured with two photodiodes. The resulting difference signal is amplified and fed to the input of a lock-in amplifier. At the same time the intensity of a small part of one of the two beams is measured with a separate photodiode. This signal represents the reflectivity of the sample at the laser spot position, which is material dependent. Topographic (reflectivity signal) and magnetic (polar Kerr signal) images of the sample are obtained by scanning the cryostat (including the sample) laterally in the sample plane with a piezostage. The spatial resolution x_{\min} is diffraction-limited and determined by the numerical aperture of the objective lens and the laser wavelength. For the frequency doubled blue light ($\lambda = 400$ nm), one can achieve a resolution of $x_{\min} = \frac{\lambda}{2A_N} \approx 330$ nm. In practice, a slightly lower resolution of about 500 nm was found experimentally by scanning the laser beam over the sharp edge of a nanostructure and recording the reflectivity signal.

Since the Kerr signals are very small, lock-in detection has to be used in order to guarantee a sufficient signal-to-noise ratio. The frequency (several kHz) of the pulse generator which is used for the above described phase modulation of the microwaves provides the reference for this phase sensitive detection. Because the microwave phase is switched between 0° and 180° (cf. Fig. 4.2), the output signal from the lock-in amplifier represents the difference between the z-components of the magnetization vector on opposite sides of the precession cone (cf. Fig. 4.4). Therefore, the signal to noise ratio is increased by a factor of two compared to microwave amplitude modulation, where the microwave excitation is switched on and off periodically.

Finally, various types of measurements are discussed: First, one can fix both the external field and the microwave frequency, and vary the phase of the microwaves with respect to the probe pulses by means of the mechanical delay line. The resulting sinusoidal signal represents the z-component of the precessing magnetization, an example is shown in Fig. 4.3. Second, by keeping phase, frequency and magnetic field constant and scanning the sample, magnetic images of the sample can be recorded. Third, and most importantly, FMR spectra at a certain sample position (x,y) can be measured by sweeping the external field and keeping all other parameters constant. Based on the correlation between microwave excitation and probe pulses, the Kerr-FMR spectra can have different lineshapes. This is illustrated for two special cases in Fig. 4.4. For the sake of simplicity, the static magnetization is assumed to point along the x-direction and the tip of the precessing magnetization is assumed to move on a circular path in the y-z-plane with microwave excitation. The dots label the position of the tip of \vec{M} at the point in time when the probe pulse queries the z-component of \vec{M} . Far away from resonance ($H_0 \ll H_R$ and $H_0 \gg H_R$), the precession amplitudes are small, expressed by the smaller circles. At resonance ($H_0 = H_R$), the precession amplitude reaches the maximum. In addition, the phase between excitation field \vec{h} and the precessing magneti-

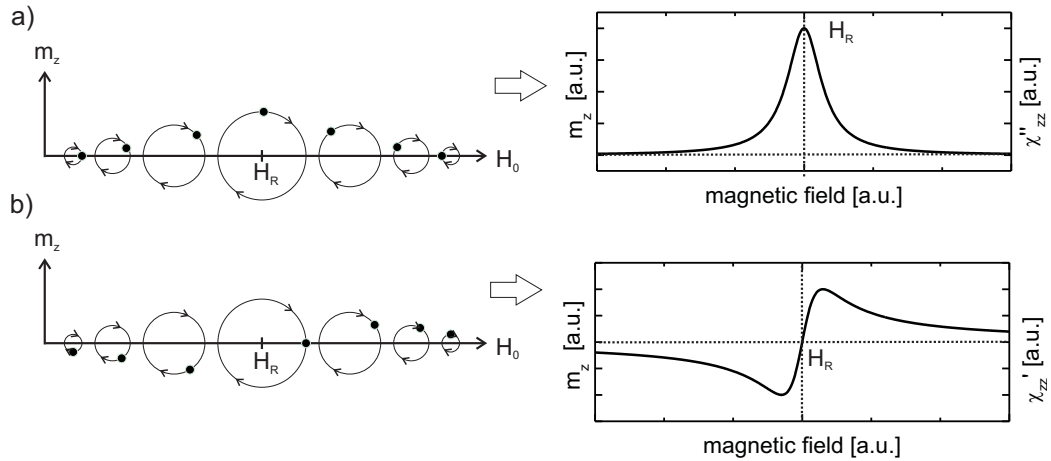


Figure 4.4: Illustration of the different lineshapes in Kerr-FMR measurements. (Left side) z -components of the magnetization M_z versus external magnetic field H_0 for two different microwave phases. The static magnetization lies along the x -direction. The circles represent the precessing magnetization in the y - z -plane. The dots label the position of the tip of the magnetization vector for different field values at the moment when the probe pulses query m_z . (Right side) Depending on the phase correlation, the resulting spectra can have a symmetric (a) or an asymmetric line shape (b).

zation \vec{M} has to be considered. For high magnetic fields, \vec{h} and \vec{M} are in phase ($\varphi = 0^\circ$), because the frequency of the exciting microwave field is much lower than would be required to bring the sample into resonance. The phase changes continuously from 0° to 180° when the external field is decreased. At resonance, the phase lag of the precessing magnetization behind the excitation field is exactly 90° . By considering these amplitude and phase correlations, the position of \vec{M} at the probe moment can be deduced. Just by following the dots in Fig. 4.4, the origin of symmetric and asymmetric Kerr-FMR spectra (right side of Fig. 4.4) can be easily understood. Note that for arbitrary phase correlations in the experiment, the measured Kerr-FMR spectra represent a mixture between the symmetric and asymmetric lineshapes.

4.5 All-optical pump-probe technique

In conventional time-resolved MOKE experiments usually a fast magnetic field pulse triggers the precession of the magnetization. This field pulse can be generated in a microcoil or stripline using a fast photodiode, an Auston-switch, or a pulse generator [54–56]. Instead, in all optical experiments, both the excitation and the detection of the precessional motion of the magnetization are performed optically [57–59]. In doing so, the precession is triggered by a temporal change in the effective field direction due to a pump-induced change of the magnetic anisotropy fields. The underlying physical processes will be discussed in detail in Section 5.6. An illustration of the setup is shown in Fig. 4.5. In these all-optical experiments, the frequency doubled blue beam ($\lambda \sim 400$ nm) is used for pumping, while the red beam ($\lambda \sim 400$) acts as the probe beam. The red probe pulses are delayed with respect to the blue pump pulses by means of a mechanical

delay stage and probe the change of the z-component of the magnetization vector $\Delta M_z(t)$ by means of the polar magneto-optic Kerr effect. In front of the microscope red and blue beam are brought together using a dichroic mirror which transmits the blue beam and reflects the red beam. Both beams are linearly polarized and are focussed to the same sample position. The rotation of the polarization of the reflected red beam is analyzed by the polarization sensitive detector (as described above). The spatial overlap of pump and probe beam is found using the following procedure: First, the blue pump beam is blocked and an image of a microstructure is measured by scanning the sample and recording the reflectivity of the red probe beam. Then another image is obtained by performing the same process with probe beam blocked. If the two beams are misaligned, the images are shifted with respect to each other. The exact overlap is set by changing the alignment of the pump beam via adjustable scanning mirrors. Subsequently, the pump beam is blocked in front of the detector by using an interference filter. In order to increase the SNR, lock-in detection is applied and the pump beam is modulated by a mechanical chopper operating at a frequency of approximately 1.5 kHz. Therefore, the Kerr signal corresponds to the difference of the perpendicular magnetization components with and without excitation $M_z(t) - M_z^0$, where M_z^0 labels the static z-component of the magnetization. Since the static magnetization of all investigated films lies in the film plane ($M_z^0 = 0$), the polar Kerr signal represents the dynamic z-component of the magnetization $M_z(t)$. As an example, the exponentially damped oscillation shown in Fig. 4.5 can be attributed to the damped precessional motion of the magnetization.

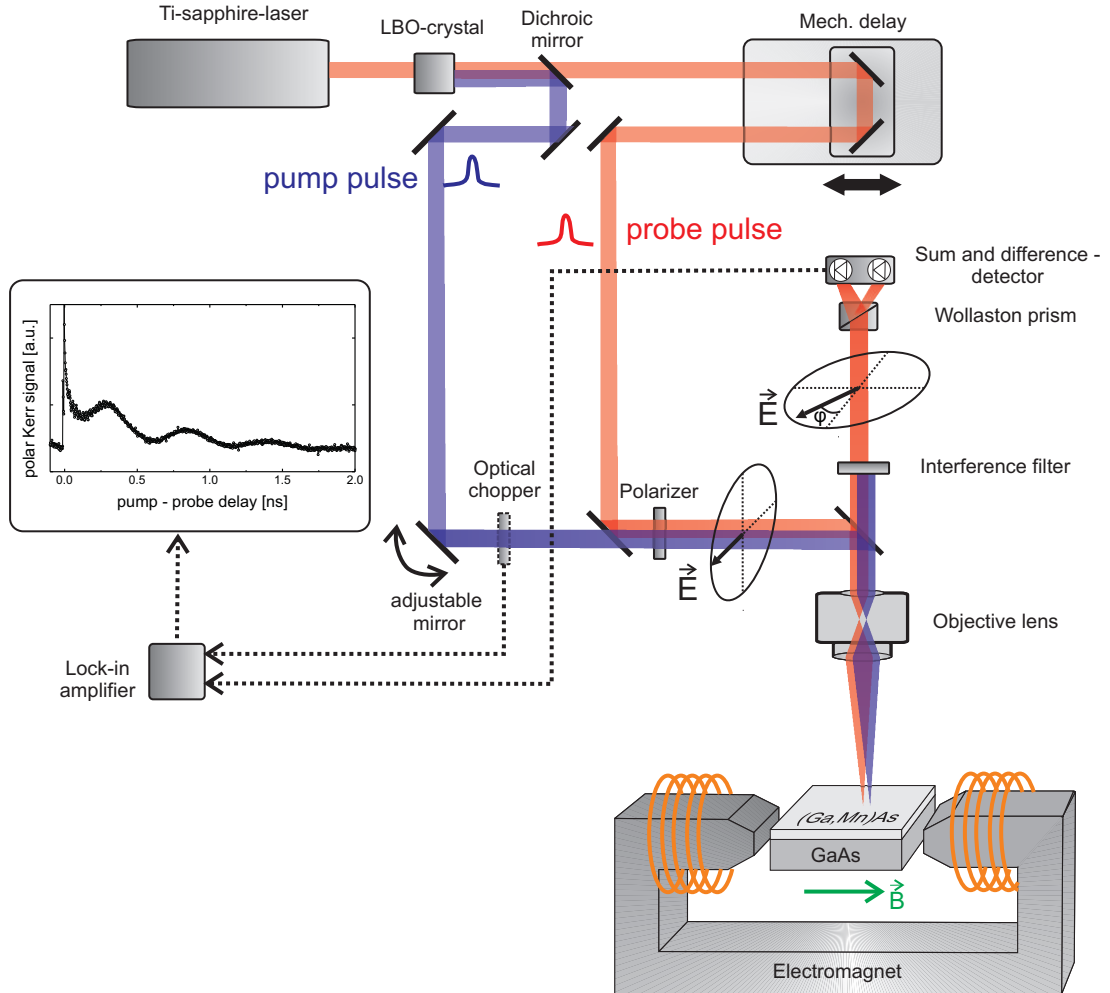


Figure 4.5: Scheme of the all-optical MOKE setup. The frequency doubled ($\lambda = 400$ nm) blue pump pulses are focused onto the sample and trigger the magnetization dynamics. The red pulses ($\lambda = 800$ nm) are used to probe the changes of the perpendicular magnetization component M_z using the polar magneto-optic Kerr effect. For this the polarization of the reflected light is analyzed by means of a polarization sensitive detector. The spatial overlap of pump and probe beams is set by tilting the pump beam by adjustable mirrors. Note that for a better visualization pump and probe beams are offset parallel. The temporal evolution of the Kerr signal is obtained by delaying the probe pulses with respect to the pump pulses using a mechanical delay stage. The pump beam is chopped in order to apply lock-in amplification. The sample is mounted on the cold finger of a He-flow cryostat allowing a sample temperature from 4 K to room temperature. Static magnetic fields can be applied in any direction in the sample plane by using a rotatable electromagnet.

5 Magnetic anisotropy and damping of (Ga,Mn)As films

In this chapter various experimental techniques are introduced which can be used to study the magnetic anisotropies and damping in (Ga,Mn)As films. In Section 5.1 the reliability of the local Kerr-FMR technique will be demonstrated by comparing the results to conventional ferromagnetic resonance. In Section 5.3 angle-resolved FMR measurements are employed to measure the different anisotropy contributions in (Ga,Mn)As films. The physical origin of these anisotropies and the dependence of the anisotropies on parameters such as strain, temperature or Mn-concentration are discussed. Another novel approach using an electrical detection scheme of the ferromagnetic resonance will be introduced in Section 5.4. In Section 5.5 the magnetic damping mechanisms in (Ga,Mn)As are addressed. Both the Gilbert damping factor, which is related to the intrinsic damping mechanisms in (Ga,Mn)As, and the inhomogeneous linewidth, caused by local variations of the magnetic properties, are discussed. The local Kerr-FMR technique is also used to draw conclusions about the homogeneity of the magnetic anisotropies on microscopic and macroscopic length scales. In addition, the experimental results are compared to all optical experiments where a strong pump pulse is used to trigger precessional motion of the magnetization (Section 5.6). A combination of pump-probe and FMR techniques is employed to investigate how transient carriers influence the magnetic properties of (Ga,Mn)As.

5.1 Comparison of local and integral FMR techniques

Most of the results in this thesis were obtained by locally probing the precession of the magnetization by means of the polar magneto-optic Kerr effect. I.e., the magnetic properties are measured within the laser spot diameter which is in the submicrometer range (probe area $\approx 0.25 - 1\mu\text{m}^2$) while the signal in conventional FMR is an average of the entire sample area (usually several mm^2). Thus the locally probed sample volume is six to seven orders of magnitude smaller compared to the conventional FMR method which also demonstrates that the local Kerr-FMR technique provides direct access to the local magnetic properties. By investigating an extended (Ga,Mn)As element, it can be verified that both approaches yield consistent results. Furthermore, the comparison of the linewidths of both techniques allows one to draw conclusions about the sample homogeneity and the damping processes. These topics are discussed in Section 5.5. The results of the local Kerr-FMR measurements can be also compared to conventional FMR measurements which are performed in another experimental setup using a closed-

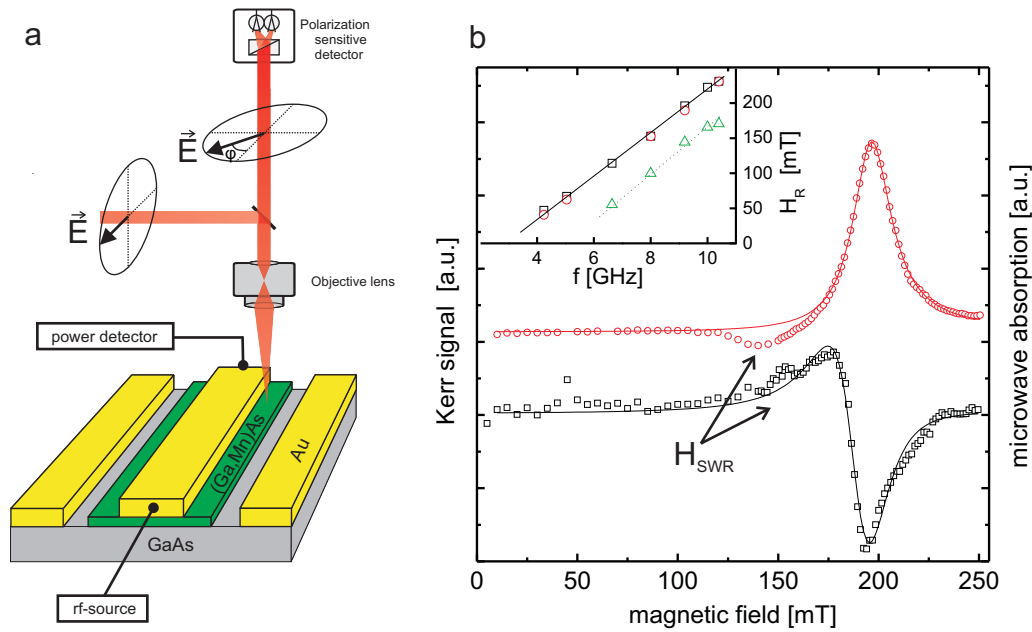


Figure 5.1: (a) Illustration of the measurement setup using local and inductive probing techniques. (b) Local FMR measurement at the center of the 1 mm long stripe (red circles) and microwave absorption of the total sample (black squares). Both measurements were performed under the same conditions like microwave frequency ($f = 9.2$ GHz) and temperature ($T = 8$ K) and are vertically offset for clarity. The external magnetic field was applied along an easy axis of the cubic anisotropy $\langle 100 \rangle$. The experimental results are fitted by a Lorentzian and the derivative of a Lorentzian function (solid lines). The second and less pronounced resonance at $\mu_0 H_{\text{SWR}} \approx 140$ mT which is observed both in the local as well as in the inductive measurement, can be attributed to a spin wave resonance (SWR). The local (circles) and integral (squares) resonance fields H_R , and the position of the SWR (triangles) as a function of microwave frequency are plotted in the inset of (b).

cycle cryostat. The comparison is, however, delicate since the magnetic properties like Curie temperature or magnetic anisotropies show slight variations at different positions of the same (Ga,Mn)As wafer due to inhomogeneous growth conditions. Nevertheless, similar conditions can be obtained by measuring *local* and *integrated* FMR signals at the same time using the same experimental setup and exactly the same sample. For this purpose, a (Ga,Mn)As stripe of $1 \text{ mm} \times 50 \mu\text{m}$ was prepared by optical lithography and ion beam etching and then covered by a coplanar waveguide with a signal linewidth of $30 \mu\text{m}$ (Fig. 5.1(a)). The frequency characteristics and the field profiles of such a planar waveguide are discussed in detail in Appendix 8.3.

In the experiments, the microwave frequency is kept constant and the external magnetic field is swept. When the sample undergoes resonance (FMR) microwave power is absorbed, which is detected by measuring the transmitted rf-power by means of a Schottky-diode. At the same time, the precession of the magnetization at a certain sample position (x, y) is probed by means of the magneto-optic Kerr effect.

Typical FMR spectra are shown in Fig. 5.1(b). The local measurements were performed

with a laser spot of $\approx 1 \mu\text{m}$ diameter in the center of the 1 mm long (Ga,Mn)As stripe. In Section 2.3.5 it was demonstrated that for small damping ($\alpha \ll 1$) and if $\vec{M} \parallel \vec{H}_0$, the line shape of the spectrum is given by an asymmetric Lorentzian function. In the inductive approach, an additional AC magnetic field with a frequency of ≈ 70 Hz and an amplitude of 1-2 mT was used in order to apply lock-in detection and to enhance the signal-to-noise ratio. Therefore, the line shape of the inductive FMR measurements corresponds to the derivative of a Lorentzian function (Eq. 2.29). Compared to conventional 3d-ferromagnets, the saturation magnetization in (Ga,Mn)As is one to two orders of magnitude smaller and the damping factor α is one order of magnitude larger, thus the signal-to-noise ratio in the inductive experiment is relatively low. Nevertheless, by fitting the experimental data to Eqs. 2.28, 2.29, the resonance fields H_R and linewidths ΔH can be compared quantitatively. The resulting resonance fields for a microwave frequency $f = 9.2$ GHz extracted from the fits (solid lines in Fig. 5.1(b)) are $\mu_0 H_R^{\text{Ind}} = 190$ mT and $\mu_0 H_R^{\text{Loc}} = 196$ mT for the inductive and local spectrum, respectively. This good quantitative agreement is also found for other microwave frequencies (inset of Fig. 5.1(b)). These results demonstrate that the Kerr-FMR technique is a valuable technique to study the magnetic properties, such as the magnetic anisotropies, on small length scales. In contrast to the good agreement of local and inductive resonance fields, the inductive linewidth $\mu_0 \Delta H^{\text{Ind}} = 17.2$ mT is approximately 50 % larger than the local linewidth $\mu_0 \Delta H^{\text{Loc}} = 11.7$ mT. Although a small part of the inductive linewidth (< 1.5 mT) is related to parasitic effects like temperature variations (see the discussion in Section 5.5), this discrepancy shows that the resonance fields are spatially inhomogeneous, leading to the broadening of the lines in the inductive measurements. These variations of the resonance fields may be attributed to sample inhomogeneities causing local variations of the magnetic anisotropy and magnetization. Therefore, one has to be aware, that the results from integrating measurements, such as SQUID or FMR, only reflect the average magnetic properties of the macroscopic sample and that the local microscopic parameters can deviate significantly. This topic will be also addressed in detail in Section 5.5.

Finally, the physical origin of the second less pronounced peak at $\mu_0 H_{\text{SWR}} = 140$ mT in Fig. 5.1(b) will be discussed. While the main peak at $\mu_0 H_R = 195$ mT corresponds to the quasi-uniform precession of the magnetization, where all magnetic moments precess in phase, the second less pronounced peak at $\mu_0 H_{\text{SWR}} = 140$ mT, can be attributed to a spin wave resonance (SWR). In the inset of Fig. 5.1(b), this assignment is confirmed by the frequency independent separation of the SWR to the main resonance $\mu_0 H_{\text{sep}} = \mu_0 (H_R - H_{\text{SWR}}) \approx 50$ mT. Using the simplified picture, that the magnetic film perpendicular to the film plane is considered as a chain of precessing spins, a spin wave can be understood in the sense of a constant phase difference of the precession between neighboring spins. The finite thickness of the film and the boundary conditions at the film surfaces lead to a quantization of the spin waves perpendicular to the film plane (described by the mode number n). These spin waves are also referred to as perpendicular standing spin waves (PSSW). A very sophisticated analysis of the spin wave resonances in (Ga,Mn)As was recently given by Bihler et al. [60]. Both the positions

and the intensities of the resonances could be well reproduced in an elaborate model. The model assumes a linear gradient of the perpendicular anisotropy in the bulk of the (Ga,Mn)As film and "natural freedom" of the surface spins, which corresponds to neither fully pinned nor unpinned boundary conditions. In Ref. [61], it was found that Kittel boundary conditions [62] with strong pinning of the surface spins, are appropriate to describe the spin wave resonances of an annealed (Ga,Mn)As film, when the external field is applied in the film plane. Due to the film thickness of $t = 50$ nm, the intensities of the spin wave resonances in the studied sample are relatively small and only the first spin wave resonance can be observed in Fig. 5.1(b). Therefore, it is unclear, which of the discussed models is appropriate. Nevertheless, the Kittel-model with pinned boundary conditions can be used to get a rough estimate of the spin wave stiffness D , which reflects the strength of the exchange coupling. The separation $\mu_0 H_{\text{sep}}$ between main resonance and the spin wave resonances is given by the following equation [62]:

$$\mu_0 H_{\text{sep}} = \frac{D}{g\mu_B} \frac{\pi^2}{t^2} n^2 \quad (5.1)$$

where $t = 50$ nm is the film thickness and n is an odd integer representing the mode number. Although the resulting spin wave stiffness $D = 147 \text{ meV}\text{\AA}^2$ ($D^* = \frac{D}{g\mu_B} = 12.7 \text{ Tnm}^2$) can only be considered as a rough approximation, D is in good agreement to the more accurate SQUID measurements of the spin wave stiffness $D = (129 \pm 15) \text{ meV}\text{\AA}^2$ of the same (Ga,Mn)As film C. For the experimental determination of the spin wave stiffness refer to the PhD-thesis of M. Sperl [48]. From D the exchange constant $A = \frac{M_S D^*}{2} = 2.1 \cdot 10^{-13} \frac{\text{J}}{\text{m}}$ can be derived. Finally, from A the exchange length $l_{\text{ex}} = \sqrt{\frac{2A}{\mu_0 M_S^2}} = 18$ nm can be deduced which provides a length scale across which the exchange interaction is dominant over the dipolar interaction. Compared to 3-d ferromagnets, such as iron ($l_{\text{ex}} = 3.3$ nm), the exchange length in (Ga,Mn)As is significantly larger.

5.2 Effects of microwave excitation

The analysis of the data in this thesis is based on the linearized LLG-equation, which is only valid for small precession angles of the magnetization. By determining the excitation fields and the dynamic susceptibility, one can estimate these precession angles to justify the application of this small angle approximation. In addition, the measurement of the Kerr amplitude as a function of the excitation field will demonstrate that nonlinear effects are irrelevant in our experiments. Finally, it will be shown that the sample temperature is slightly raised by ohmic losses in the microwave wave guides. This effect is of special importance at relatively low sample temperatures. At first, the precession angles of the magnetization are estimated under typical experimental conditions: Considering the waveguide design and also the non-uniform current density across the conductors (see Appendix 8.3), a maximum excitation field of $\mu_0 h_z = 0.2$ mT at the sample position can be estimated. Due to the relatively low susceptibility at resonance

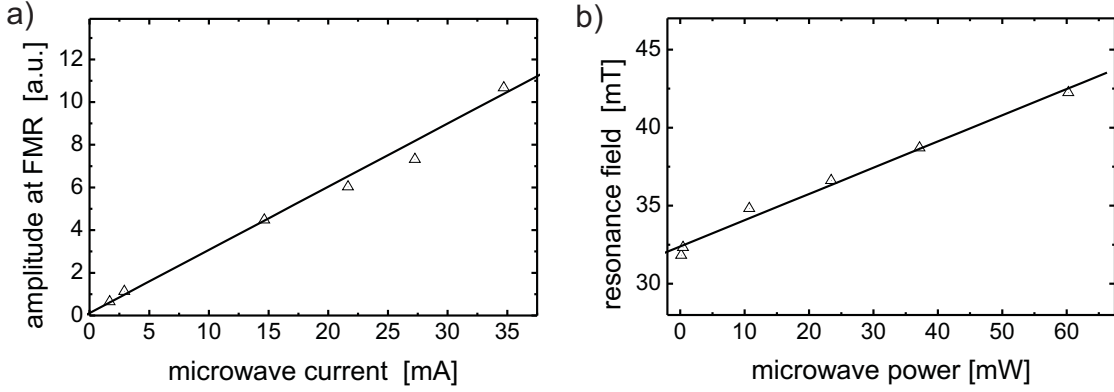


Figure 5.2: Experimental data obtained with sample B, for $f = 3.04$ GHz, a temperature of 7 K and for the external field applied along an easy axis [100]. (a) The amplitude of the polar Kerr signal at resonance is plotted as a function of the microwave current I . (b) The linear dependence of the resonance fields as a function of microwave power indicates the heating effects of the microwave excitation. The solid lines are linear fits to the experimental data.

of typically 1-10 (which is mainly related to the high damping factor in (Ga,Mn)As), an in-plane precession angle of $1^\circ - 3^\circ$ can be estimated. Because of the elliptical trajectory of the magnetization, the out of plane precession angle is even smaller. Consequently, the experiments can be described using the linearization of the LLG-equation. In order to exclude the presence of other non-linear effects experimentally, FMR measurements were performed in a large power range of -9 dBm to +18 dBm under otherwise identical conditions. By fitting the individual FMR spectra to a Lorentzian function, both the resonance fields and the amplitudes of the polar Kerr signal at resonance were extracted. In Fig. 5.2(a), the Kerr signal (proportional to the out-of-plane precession component m_z) is plotted as a function of the microwave current (proportional to the excitation field h_z). The linear dependence demonstrates that non-linear effects can be neglected. Finally, also the microwave induced sample heating will be discussed. In Fig. 5.2(b), a linear increase of the resonance fields with increasing microwave power P_{rf} is observed. Since the magnetic anisotropies in (Ga,Mn)As show a very strong temperature dependence, this demonstrates that the sample temperature is raised by ohmic losses in the metallic waveguide. The increase of the resonance field H_R can be mainly attributed to a temperature induced reduction of the perpendicular magnetic anisotropy $K_{U\perp}$. The temperature increase $\Delta T(P_{\text{rf}})$ can be estimated by comparison with temperature dependent measurements of the anisotropy parameters (Section 5.3.2). The observed shift of $\frac{\Delta H_R}{\Delta P_{\text{rf}}} = \frac{1}{6} \frac{\text{mT}}{\text{mW}}$ can be explained by a temperature increase of $\frac{\Delta T}{\Delta P_{\text{rf}}} \approx 0.5 \frac{\text{K}}{\text{mW}}$. As an example, the microwave power $P_{\text{rf}} = 10$ dBm (10 mW) leads to a temperature increase of ≈ 5 K with respect to the sample temperature without microwave excitation. As a consequence, for a quantitative comparison of the experimental results, it was necessary to maintain exactly the same microwave power during the measurements.

5.3 Magnetic anisotropies of (Ga,Mn)As films

In this section, angle-resolved FMR measurements are employed to determine the magnetic anisotropies of thin (Ga,Mn)As films. The comparison of different samples will

demonstrate the complex dependence of the anisotropies of various parameters, such as temperature, strain, and hole concentration. The experimental results are also compared to the predictions of the mean field Zener model (see Section 3.3 and Refs. [37, 44]). In addition, before the lithographically defined (Ga,Mn)As elements in Chapter 6 can be addressed, the unpatterned (Ga,Mn)As films need to be characterized and their behavior understood.

The discussion in Section 3.3 has demonstrated that the magnetic anisotropies of (Ga,Mn)As films grown on (001)-oriented substrates can be described by taking into account four contributions: a cubic anisotropy ($K_{C\perp}$ and $K_{C\parallel}$) due to the symmetry of the zinc-blende lattice, a uniaxial anisotropy perpendicular to the film plane ($K_{U\perp}$), due to the compressive strain in the film plane, and a uniaxial anisotropy in the film plane ($K_{U\parallel}$), whose physical origin is still under discussion. Finally, also the magneto-static shape anisotropy (K_S) has to be considered.

These different contributions will be introduced only exemplarily by discussing four films: Three films with the same nominal Mn-content $x = 0.06$ (samples A,B,C), and one film with a much higher Mn-concentration $x = 0.125$ (sample D), whose magnetic anisotropies differ significantly from all other films. The sample properties, such as thickness and hole concentration, are summarized in table 5.1. Details concerning the MBE growth, annealing process and layer composition are given in Appendix 8.1.

In contrast to conventional FMR, the Kerr-FMR technique requires the samples to be prepared by means of lithography. The sample design is illustrated in Appendix 8.2. The measurements were performed on (Ga,Mn)As structures with lateral dimensions of several tenths of micrometers. In order to exclude strain relaxation effects at the edges of the (Ga,Mn)As elements which can modify the magnetic anisotropies locally (compare Chapter 6), all FMR measurements were performed at a distance of at least $5\mu\text{m}$ from the boundaries.

The coordinate system which is used throughout this thesis is shown in Fig. 5.3(a). In this measurement configuration, both the magnetic field \vec{H}_0 and the magnetization \vec{M} are aligned in the film plane (001). The procedure, which was used to experimentally determine the anisotropy parameters is illustrated with the help of the representative (Ga,Mn)As sample C. In Fig. 5.3(b), FMR spectra for various angles of the magnetic field φ_H for $f = 3.84$ GHz are shown. One observes a clear dependence of the resonance fields H_R (the field positions with maximum Kerr signal) on the field angle φ_H , with minima along [100] and [010], and a maximum along [110]. The symmetry of the angular dependence $H_R(\varphi_H)$ provides information about the symmetry of the internal magnetic fields. The fourfold symmetry of $H_R(\varphi_H)$ can be attributed to the cubic anisotropy $K_{C\parallel}$, reflecting the symmetry of the (Ga,Mn)As zinc-blende lattice. The different values of the resonance fields along [110] and $[1\bar{1}0]$ are caused by the uniaxial in-plane anisotropy $K_{U\parallel}$. Finally, the perpendicular anisotropy $K_{U\perp}$ does not lead to an angular variation of the resonance fields in this in-plane configuration, but only to a constant resonance field offset, which shifts the resonance positions to larger (smaller) values for smaller (larger) values of $K_{U\perp}$. A detailed discussion of the physical origin of these anisotropies is given in sections 3.3 and 6.5. Quantitatively, the anisotropy constants can be deter-

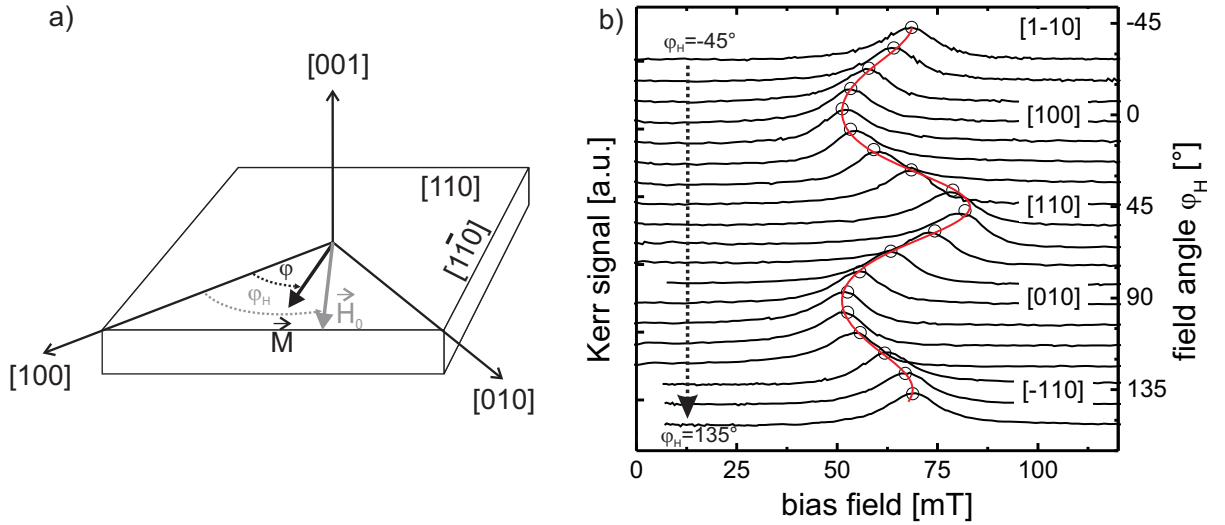


Figure 5.3: (a) FMR geometry: Both the external field \vec{H}_0 and the magnetization \vec{M} are aligned in the film plane (001). (b) FMR spectra of sample C (50 nm thick $\text{Ga}_{0.94}\text{Mn}_{0.06}\text{As}$) for various field angles φ_H for $f = 3.84$ GHz and $T = 7$ K. The resonance fields H_R which are obtained by fitting the experimental FMR spectra to a Lorentzian function (Eq. 2.28) are given by open dots. The solid line represents the best fit, which was obtained by the procedure described in the text below. The resulting fit parameters $K_{C\parallel}$, $K_{U\parallel}$, $K_{U\perp}$ are summarized in table 5.1.

mined by fitting the experimental data to Eq. 2.19, which was derived theoretically in Section 2.3.4. Five unknown parameters enter Eq. 2.19, magnetization M , g-factor g , which determines the gyromagnetic ratio $\gamma = g\mu_B/\hbar$, effective magnetization M_{eff} , cubic in-plane anisotropy $K_{C\parallel}$ and uniaxial in-plane anisotropy $K_{U\parallel}$. The effective magnetization $\mu_0 M_{\text{eff}} = \mu_0 M - \frac{2K_{U\perp}}{M}$ includes both demagnetization field and strain-induced perpendicular anisotropy. Since the magnetization M in Eq. 2.19 enters the individual terms as a prefactor, M is no adequate fitting parameter and needs to be determined with an independent measurement technique. SQUID measurements of each sample were employed to determine the temperature dependence of the magnetization $M(T)$. The remaining four parameters cannot be obtained by fitting a single experimental angular dependence $H_R(\varphi_H)$. A simultaneous determination of both M_{eff} and g-factor would require the measurement of the resonance fields in a second FMR geometry (e.g. \vec{H}_0 applied in the (110)-plane) or the measurement of the angular dependence $H_R(\varphi_H)$ at two very different microwave frequencies. These requirements cannot be satisfied in the present Kerr-FMR setup, since neither very high magnetic fields nor fields perpendicular to the film plane can be applied. Yet, the g-factor of (Ga,Mn)As films with various Mn- and hole concentrations was already studied experimentally by means of conventional FMR using modulation doped and hydrogen passivated samples [38, 63]. If the magnetization in (Ga,Mn)As originated simply from the magnetic moments of the Mn-spins, in these studies $g = 2.00$ would have been observed, since the magnetic moment of isolated Mn^{2+} ions is $\mu_{\text{Mn}} = 5\mu_B$. Indeed, a slight decrease of the g-factor with increasing hole concentration was found, which demonstrates that the magnetic

moment of the holes contributes to the total magnetic moment. Therefore, the FMR experiments must be understood in the sense of a collective precession of the exchange coupled Mn/hole complex. Following the results from Khazen et al. [38], $g = 1.95$ was used for the (Ga,Mn)As films with average hole and Mn-concentrations (samples A,B,C), while for the (Ga,Mn)As film D with much higher hole and Mn-concentration the g-factor was set to $g = 1.9$. The remaining uncertainty of the g-factors in the present samples should lead only to insignificant errors of the anisotropy constants.

Once $M(T)$ and g are known, only the anisotropy constants $K_{C\parallel}$, $K_{U\parallel}$ and M_{eff} remain as fitting parameters. The perpendicular anisotropy constant can then be calculated using the relation $\mu_0 M_{\text{eff}} = \mu_0 M - \frac{2K_{U\perp}}{M}$. In order to account for the deviation of the magnetization direction φ from the external field angle φ_H (so called 'dragging'), the fitting procedure is performed as follows: At first, the resonance field H_R^i for a certain field angle φ_H is calculated using a set of start parameters ($K_{C\parallel}^i$, $K_{U\parallel}^i$, M_{eff}^i) and under the assumption, that the magnetization is aligned along the field direction ($\varphi = \varphi_H$). The resulting H_R^i is used to minimize the energy density (Eq. 2.12), in order to find the actual magnetization angle. Next, the actual resonance field H_R is recalculated using this new angle φ . This procedure is repeated for each field angle, which yields the angular dependence $H_R(\varphi_H)^i$ for this initial set of parameters. The whole procedure above is performed repeatedly for each new set of fitting parameters, until the best agreement of the fit function with the experimental data is found. As an illustration, Fig. 5.3(b) demonstrates the good agreement between theoretical fit function (solid line) and experimental resonance fields (open dots). The resulting anisotropy constants (table 5.1) will be discussed in the following. The value of the perpendicular anisotropy $K_{U\perp} = -3.1 \times 10^3 \frac{\text{J}}{\text{m}^3}$ is comparable to earlier FMR studies of samples with similar Mn and hole-concentration [38, 64]. $K_{U\perp}$ is also in fairly good agreement with the predictions of the mean-field Zener model [37]: $K_{U\perp} = H_{2\perp} M / 2 \approx -4 \times 10^3 \frac{\text{J}}{\text{m}^3}$ ($x = 0.05$, $p = 3.5 \times 10^{20} \text{cm}^{-3}$, $\varepsilon_{xx} = -0.25$). Because of the negative sign of $K_{U\perp}$ and because $|K_{U\perp}| \gg |K_{C\parallel}|, |K_{U\parallel}|$, the easy axes of the magnetization lie in the film plane. This behavior is also found for the other studied samples A,B,D with intermediate or high Mn- and hole concentrations ($x \geq 0.06$, $p > 2 \times 10^{20} \text{cm}^{-3}$), where $K_{U\perp}$ has a negative sign in the whole temperature range (e.g. table 5.1 and Fig. 5.6). An easy axis perpendicular to the film plane was only reported for (compressively strained) (Ga,Mn)As films on GaAs(001) substrates for low hole concentrations $p \ll 10^{20} \text{cm}^{-3}$ and at low temperatures [38, 65].

Finally, the magnetic anisotropies in the film plane are discussed. In the mean-field calculations [37, 44], it was found that the easy axis of the cubic anisotropy $K_{C\parallel}$ oscillates between $\langle 100 \rangle$ and $\langle 110 \rangle$ as a function of the hole concentration. However, such a behavior was not observed in experiments with variable hole concentration, but constant Mn-concentration [7, 38, 63]. As an example, the FMR studies of Ref. [38] showed a decrease of $K_{C\parallel}$ with increasing hole concentration p . Due to these disagreements, it is not reasonable to compare the experimental values of $K_{C\parallel}$ with the mean-field calculations. In addition, in the initial theoretical models [37, 44], a uniaxial anisotropy $K_{U\parallel}$ in the film plane is not included, because in a zinc-blende lattice, $[110]$ and $[1\bar{1}0]$ are equivalent. At

Table 5.1: Overview of the sample properties and the magnetic parameters of (Ga,Mn)As films with various nominal Mn-concentration x , thickness t , and post-growth treatment. Samples B and C differ only in the annealing temperature and duration. The hole concentrations were determined in a standard hall-bar geometry at $T = 4.2$ K. The anisotropy constants were measured at $T = 7$ K (samples A,B,C), and at $T = 25$ K (sample D).

	annealing	x [%]	t [nm]	p $\times 10^{20}[\text{cm}^{-3}]$	T_C [K]	$\mu_0 M_0$ [mT]	$K_{U\perp}$ $\times 10^2[\frac{\text{J}}{\text{m}^3}]$	$K_{C\parallel}$ $\times 10^2[\frac{\text{J}}{\text{m}^3}]$	$K_{U\parallel}$ $\times 10^2[\frac{\text{J}}{\text{m}^3}]$
A	as-grown ^a	6	100	4.4	63 ± 3	40	-66 ± 2	1.7 ± 0.2	-1.2 ± 0.2
B	3h@180°C	6	50	2.0	86 ± 3	33	-40 ± 1	3.7 ± 0.2	-1.9 ± 0.2
C	20h@200°C	6	50	≈ 4 ^b	110 ± 3	43	-31 ± 1	2.2 ± 0.1	1.2 ± 0.1
D	6h@160°C	12.5	20	23	184 ± 3	106	-174 ± 2	-1.3 ± 0.5	18.6 ± 0.6

^a Although sample A was annealed after the MBE growth, it is referred to as as-grown sample, because the annealing led only to insignificant changes of the sample properties (same $M(T)$ characteristics, increase of T_C smaller than 7 K).

^b p was not determined in sample C. However, since samples B and C differ only in the annealing process, the relation $T_C \propto x p^{1/3}$ was used to estimate $p \approx 4 \times 10^{20} \text{cm}^{-3}$ in sample C.

the moment, the presence of $K_{U\parallel}$ is simply acknowledged as an experimental fact, a more detailed discussion of its origin will be given in Section 6.5. It should be pointed out that due to the competition between the in-plane anisotropies $K_{C\parallel}$ and $K_{U\parallel}$, the easy axes of the magnetization are not aligned along the crystallographic directions ([100], [110], etc.), but at intermediate angles defined by the ratio of $K_{C\parallel}/K_{U\parallel}$. In Section 5.3.2, it will be demonstrated, that the temperature characteristics of this ratio can lead to spin reorientation transitions in the film plane.

5.3.1 Influence of annealing and Mn-concentration

After having analyzed the magnetic properties of the representative sample C, also other samples, which differ in the treatment after the MBE growth will be discussed. It is well established, that optimized annealing can lead to significant improvements of the magnetic and structural properties, such as increase of Curie temperature, magnetization and hole concentration [23, 24, 66]. Also a reduction of the FMR linewidth was found [26, 30], which is an indication of an improvement of the sample homogeneity.

As discussed above, SQUID measurements were employed to determine T_C and $M(T)$. The resulting parameters are summarized in table 5.1. Samples B and C, which differ only in the annealing time and temperature, show different values of the Curie temperature of $T_C = 86$ K and $T_C = 110$ K, demonstrating that the magnetic properties depend crucially on the annealing process. Apparently, in sample C the higher annealing temperature of 200°C and the longer annealing time of 20 h has led to a more efficient diffusion and passivation of Mn-interstitials (Mn_I), reflected by the higher hole concentration and Curie temperature. This behavior is also expressed by an increase of the magnetization from $\mu_0 M_0 = 33$ mT to $\mu_0 M_0 = 43$ mT after the optimized annealing

treatment. It is not useful to compare the anisotropies of the annealed samples B and C, because the different annealing processes lead also to significant changes of the hole concentration p . Experimentally, a very strong dependence of the perpendicular and cubic anisotropy on the hole concentration was found [38,39], therefore the hole induced changes of the anisotropies in sample C probably exceed the changes of the anisotropies by other parameters, such as reduction of the compressive strain.

Indeed, the comparable hole concentration of the (as-grown) sample A and the (annealed) sample C offers the opportunity to compare the magnetic anisotropies of two samples with different concentration of point defects. One should however point out that the hole concentration in sample C was estimated using the hole concentration of sample B (cf. table 5.1) and can only be considered as a rough approximation. The anisotropy constants of sample A at $T = 7$ K were determined by fitting the experimental resonance fields using the same procedure as described in the previous section and are summarized in table 5.1. While the in-plane anisotropy constants of sample A and C are of comparable size, the perpendicular anisotropy $K_{U\perp}$ in the annealed sample C is by a factor of two lower. Because of the relation $K_{U\perp} \propto \varepsilon_{xx}p$ (see Section 3.3 and Ref. [38]), this reduction of $K_{U\perp}$ can be mainly attributed to a reduction of the compressive strain ε_{xx} - in spite of the uncertainty of the hole concentration in sample C. This finding is consistent with earlier x-ray diffraction studies [35], where a decrease of the perpendicular lattice constant a_{\perp} , and therefore also a decrease of ε_{xx} was found after the annealing process. The physical mechanism behind this lowering of the compressive strain is a reduction of the number of Mn-interstitials Mn_{I} during the annealing process. At last, the in-plane anisotropy constants of the individual samples A, B and C are compared. In all samples, the cubic anisotropy constants $K_{C\parallel}$ are positive and are of the same order of magnitude, as one would expect for (Ga,Mn)As films with similar values of the Mn- and hole concentration. Also the uniaxial in-plane anisotropy $K_{U\parallel}$ of all three samples is of comparable size, however, the sign of $K_{U\parallel}$ is negative in samples A,B and positive in sample C. So far, it is unclear, which sample properties determine the sign and the magnitude of $K_{U\parallel}$. Actually, it was found, that samples with intermediate Mn-concentration show a random easy axis orientation of $K_{U\parallel}$. A more detailed discussion of the origin of $K_{U\parallel}$ will be given in Section 6.5.

Finally, also a (Ga,Mn)As film which differs significantly from the above discussed samples A, B and C will be addressed. The film (sample D) with a thickness of only 20 nm and a very high nominal Mn-concentration $x = 12.5\%$ was grown by V. Novák at the institute of physics in Prague. The high Mn-content and the optimized post-growth annealing led to a very high Curie temperature of $T_C = 184$ K. More details concerning these highly-doped samples can be found in Ref. [5]. As an illustration, the angular variation of the resonance fields at $T = 25$ K is shown for sample D in Fig. 5.4. The most striking feature is the very pronounced twofold symmetry, which can be ascribed to the uniaxial in-plane anisotropy $K_{U\parallel}$. The resulting parameters from the theoretical fit (solid line) are $K_{U\parallel} = (1.86 \pm 0.06) \times 10^3 \frac{\text{J}}{\text{m}^3}$, $K_{C\parallel} = (-1.3 \pm 0.5) \times 10^2 \frac{\text{J}}{\text{m}^3}$ and $K_{U\perp} = (-1.74 \pm 0.02) \times 10^4 \frac{\text{J}}{\text{m}^3}$. Due to the very large value of $K_{U\parallel}$ which is one order of magnitude larger than in samples A,B,C this sample is well suited to elucidate the physical origin of this controversially discussed uniaxial in-plane anisotropy. This topic

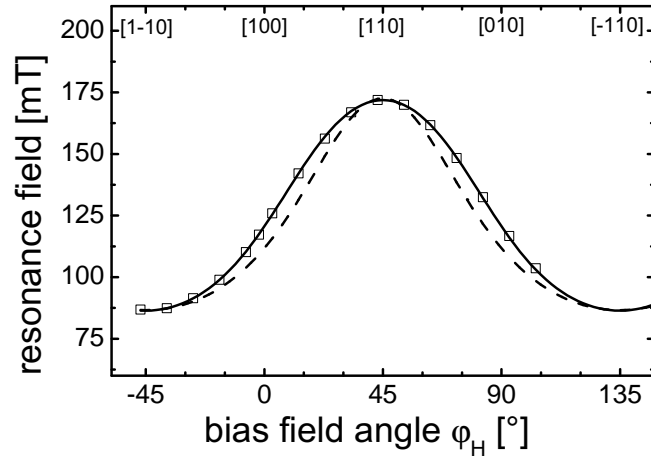


Figure 5.4: Angular variation of the resonance fields of the $\text{Ga}_{0.875}\text{Mn}_{0.125}\text{As}$ film D for $f = 8$ GHz and $T = 25$ K. Solid (dashed) curves represent theoretical fits using a negative (positive) value for $K_{C\parallel}$.

will be addressed in Section 6.5, where the anisotropies of this unpatterned film are compared to the anisotropies of lithographically defined elements. Also the perpendicular anisotropy $K_{U\perp}$ is by a factor 2-5 larger than in the other samples, compare table 5.1. Because of the high hole concentration of this (Ga,Mn)As film, this increase is in agreement with theoretical [44] and experimental findings [32, 38, 39], where $K_{U\perp}$ increases linearly with strain ε_{xx} and hole concentration p . In addition, due to the lower growth temperature a larger concentration of As_{Ga} antisites causing an increase of the compressive strain can be expected. Although the cubic in-plane anisotropy $K_{C\parallel}$ is overshadowed by $K_{U\parallel}$, from Fig. 5.4 it is clear that only a negative sign of $K_{C\parallel}$ leads to a reasonable agreement of the theoretical fit function with the experimental data. This negative sign corresponds to easy axes oriented along the $\langle 110 \rangle$ directions. It is noteworthy, that $K_{C\parallel}$ has an opposite sign compared to samples A,B,C and to our knowledge to all previous experimental reports of the anisotropies in (Ga,Mn)As [7, 30, 32, 38, 39, 61, 63, 67, 68].

5.3.2 Temperature dependence of the magnetic anisotropies

In the mean-field Zener model [37, 44], the magnetic anisotropies in (Ga,Mn)As are characterized by the symmetry of the valence subbands of the holes, which are split by magnetization and strain. Since the magnetization and hole concentrations vary with temperature, the population of these subbands, and consequently also the magnetic anisotropies are a function of temperature. Actually, in FMR studies a complicated temperature dependence of the magnetic anisotropies was found, which cannot be described using a simple power law [26, 38]. Different scaling of the anisotropy constants with temperature can also lead to so called spin reorientation transitions (SRT), which were frequently observed in FMR and SQUID measurements [26, 38, 47, 65]. As an example, a SRT from in-plane to out-of-plane orientation was reported for (Ga,Mn)As films with low hole concentrations [65]. In SQUID measurements, the magnetic anisotropies

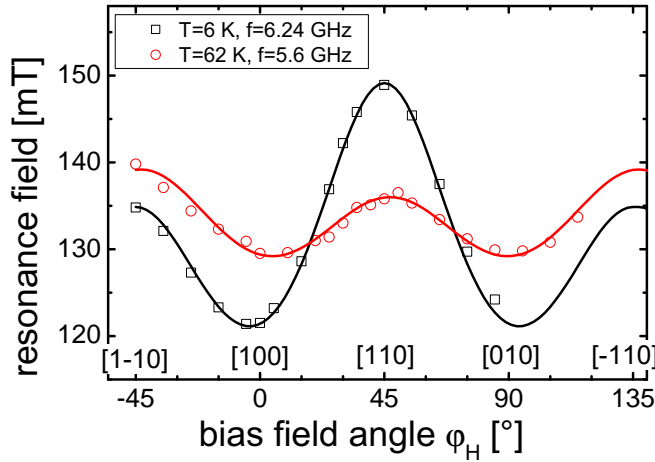


Figure 5.5: Angular variation of the resonance fields of the annealed $\text{Ga}_{0.94}\text{Mn}_{0.06}\text{As}$ film C for $T = 6$ K (squares) and $T = 62$ K (circles). Solid curves represent the theoretical fits which are used to extract the anisotropy constants.

are usually determined by fitting the experimental hard axis loops $M(H_0)$ to a theoretical fit function, under the assumption of coherent rotation of the magnetization in a single domain model. The fitting of the experimental data is restricted to higher magnetic fields because the nucleation and growth of magnetic domains in the vicinity of $H_0 = 0$ is not included in the fitting process. Even for higher fields, it is unclear, if the switching process takes place solely by coherent rotation of the magnetization. Consequently, the anisotropy parameters determined in such SQUID measurements can have a large uncertainty. In addition, the diamagnetic background of the GaAs substrate, which has to be subtracted from the raw data further complicates the analysis. In contrast, FMR measurements provide a direct quantitative access to the anisotropies and to the spin reorientation transitions in (Ga,Mn)As.

In Fig. 5.5 an illustrative example of the angular dependence of the resonance fields is shown for sample C for $T = 6$ K and $T = 62$ K. At both temperatures, one can clearly observe the superposition of a fourfold and a twofold symmetry, which can be ascribed to cubic and uniaxial in-plane anisotropies, respectively. While the maximum of the resonance field at $T = 6$ K is along $[110]$, the maximum at $T = 62$ K is shifted by 90° to the $[1\bar{1}0]$ direction. This maximum can be identified as the hard axis of the uniaxial in-plane anisotropy $K_{U\parallel}$. This temperature induced rotation of $K_{U\parallel}$ is also reproduced quantitatively by fitting the experimental data using the procedure described in Section 5.3. The resulting anisotropy parameters for several temperatures are plotted in Fig. 5.6(b): One observes, that all anisotropy constants monotonically decrease with temperature. At $T_{\text{SRT}} \approx 53$ K, however, $K_{U\parallel}$ crosses zero and changes its sign, which corresponds to a transition of the easy axis of $K_{U\parallel}$ from the $[1\bar{1}0]$ to the $[110]$ direction. These characteristics of the anisotropies are responsible for the realignment of the magnetization, a so called spin reorientation transition (SRT). Since the magnetization is aligned in the film plane (001) in all investigated (Ga,Mn)As samples and

in the entire temperature range ($4\text{K} \leq T \leq T_C$), in the following only the competition between uniaxial and cubic in-plane anisotropy needs to be considered. Only $K_{U\parallel}$ and $K_{C\parallel}$ define the equilibrium orientations of the magnetization. For a better illustration of the SRT, the free energy density F is calculated by using the experimentally determined anisotropy parameters. In Fig. 5.6(b), polar plots of F are shown for both a temperature below and above the SRT-temperature. For both temperatures, there are four possible equilibrium orientations of the magnetization (the easy axes of \vec{M}). These orientations are clearly tilted away from the easy axes of the cubic anisotropy $\langle 100 \rangle$ due to the presence of $K_{U\parallel}$. Returning to the angular variation of the resonance fields in Fig. 5.5, one finds that the minima of $H_R(\varphi_H)$ lie exactly along the $\langle 100 \rangle$ directions. This clearly demonstrates, that for comparable values of $K_{C\parallel}$ and $K_{U\parallel}$ the minima of $H_R(\varphi_H)$ do not coincide with the easy axes of \vec{M} . The resonance fields are proportional to the curvature of the energy landscape (second derivatives of the free energy), while the energy minima correspond to the first derivatives of the free energy. Therefore, the minima of the angular dependence $H_R(\varphi_H)$ only match the energy minima under certain conditions, for example if one of the anisotropy terms $K_{U\parallel}$ or $K_{C\parallel}$ is dominant. This is an important issue one has to keep in mind when analyzing the angle dependent FMR data.

Without loss of generality, \vec{M} is assumed to point along $\varphi \approx -15^\circ$ with respect to $[100]$ at low temperature. Then the spin reorientation transition proceeds as follows: Because $K_{U\parallel}$ drops more rapidly than $K_{C\parallel}$, \vec{M} rotates counterclockwise towards $[100]$ ($\varphi \rightarrow 0^\circ$) when the temperature is increased. At $T_{\text{SRT}} = 53\text{ K}$, $K_{U\parallel}$ equals zero and \vec{M} points exactly along $[100]$. With increasing temperature, $|K_{U\parallel}|$ becomes larger (now with opposite sign compared to low T), and \vec{M} rotates towards $[110]$. This description shows, that the SRT may not be understood in the sense of a sharp transition, but as a smooth continuous rotation of the magnetization vector in the film plane. This behavior is not surprising, because a combination of anisotropy terms of second and fourth order always leads to a smooth SRT. In contrast, if the second order term is dominant, the transition is sharp. As an example, in (Ga,Mn)As such a sudden reorientation of the magnetization from the perpendicular to the in-plane orientation was observed for an as-grown $\text{Ga}_{0.947}\text{Mn}_{0.053}\text{As}$ film [65]. Of course, one has to consider, that a (Ga,Mn)As film with a size of several millimeters is usually not in a single domain state, and that the SRT process is more complicated. It is conceivable, that at even higher temperatures, a second SRT $\langle 100 \rangle \rightarrow \langle 110 \rangle$ occurs, when $K_{C\parallel}(T)$ drops more rapidly than $K_{U\parallel}(T)$. Due to the lack of experimental data in this temperature range, it is unclear whether this second SRT actually takes place.

Nevertheless, this second type of SRT $\langle 100 \rangle \rightarrow \langle 110 \rangle$ was observed in the as-grown sample A. This type of SRT, which was also frequently found in SQUID measurements [47, 65, 69], can be attributed to the different temperature dependence of cubic and uniaxial anisotropies. In Fig. 5.6(a), one can clearly observe that the cubic anisotropy $K_{C\parallel}$ is dominant at low temperatures, however, with increasing temperature $K_{C\parallel}$ decreases more rapidly than $K_{U\parallel}$. Finally, at higher sample temperatures, the magnitude of the uniaxial anisotropy becomes larger than that of the cubic anisotropy.

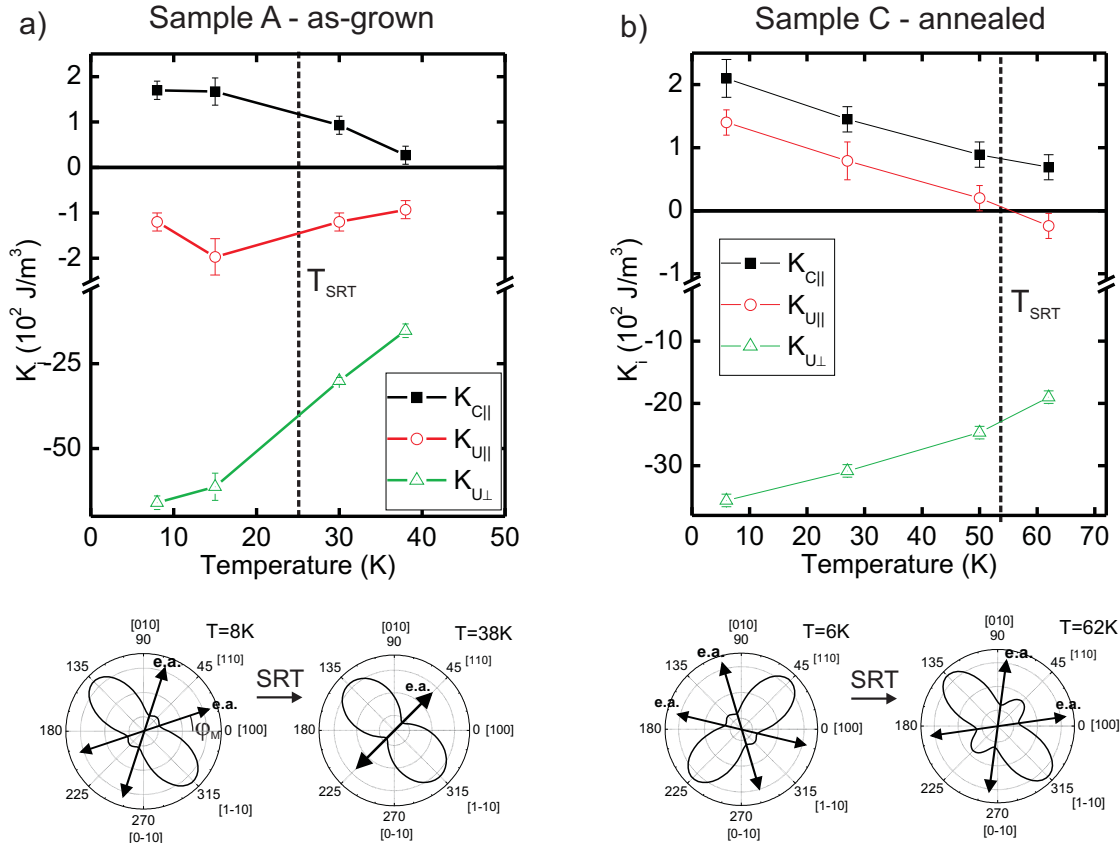


Figure 5.6: (Upper row) Temperature dependence of the anisotropy constants K_i of (a) sample A (as-grown, $t = 100$ nm) and (b) sample C (annealed, $t = 50$ nm). The solid lines are guides for the eye. (Lower row) Polar plots of the free energy densities in the film plane for $H_0 = 0$ below and above the spin reorientation temperature T_{SRT} . The arrows specify the possible easy axis orientations of \vec{M} .

Again the reorientation process can be understood very easily by calculating the free energy densities (Fig. 5.6(a)): At low temperatures, there are four possible orientations of \vec{M} , which are tilted towards $[110]$. With increasing temperature, $K_{\text{C}\parallel}$ decreases with respect to $K_{\text{U}\parallel}$ and \vec{M} rotates towards $\langle 110 \rangle$. At the spin reorientation temperature $T_{\text{SRT}} \approx 25$ K, two of the energy minima vanish and only one single easy axis along $[110]$ remains. Also above T_{SRT} , the easy axis remains fixed along $[110]$, because the uniaxial anisotropy dominates.

5.3.3 Conclusion

The FMR investigation of various (Ga,Mn)As films has demonstrated, that the magnetic anisotropies depend crucially on Mn-, hole-, defect concentration, and strain. On the other hand, these structural parameters depend sensitively on the low temperature growth and annealing parameters. Therefore, even samples grown under identical conditions do not necessarily show the same anisotropies. Furthermore, the complex temperature dependence of the anisotropies and the temperature induced spin reorien-

tation transitions complicate the application of (Ga,Mn)As as a ferromagnetic material in spin-injection experiments, magnetic tunnel junctions or other types of spintronic devices. Therefore, a technique, which allows a control of the magnetic anisotropies in (Ga,Mn)As is highly desirable. In Chapter 6, it will be shown, that lithographically defined (Ga,Mn)As elements can be used to adjust the magnetic anisotropies in a well defined and reproducible manner.

5.4 Electrical detection of the ferromagnetic resonance

Apart from the above discussed local and integral measurement techniques, the magnetic properties of micro- and nanostructures can be also investigated by performing electrical measurements. For this purpose, the precession of the magnetization is excited by microwaves, like in conventional FMR, however the resonance is detected by measuring the sample resistance. Such an experimental approach has been reported for the first time by Tsoi et al. [70] where a current driven spin wave excitation was detected electrically in a stack of magnetic multilayers by measuring the magneto-resistance. The technique has also been used to study spin excitations in a permalloy grating [71]. In (Ga,Mn)As, Wirthmann et al. [72] have demonstrated the electrical detection of the ferromagnetic resonance by means of the spin rectification effect [73], where the nonlinear combination of spin and charge dynamics generates DC-currents. By contrast, in this section a much easier approach will be introduced where the microwave excitation leads to a temperature induced resistance change and to a change of the anisotropic magnetoresistance. In the following, the feasibility of the experimental approach will be demonstrated and the physical origin of the signal will be discussed. The advantages and disadvantages of this experimental tool will be outlined at the end of the section.

An illustration of the employed measurement configuration is shown in Fig. 5.7(a). A $10\ \mu\text{m}$ broad and $70\ \mu\text{m}$ long (Ga,Mn)As element was patterned from a piece of the (Ga,Mn)As film C, which was characterized in Section 5.3. The element is placed parallel, with a distance of $5\ \mu\text{m}$, to the signal line of a coplanar strip line (CPS) and is contacted electrically by $50\ \text{nm}$ thick Au contacts. Details concerning the sample preparation and the waveguide characterization can be found in Appendices 8.2 and 8.3, respectively.

All electrical measurements were performed in a simple two point configuration by applying a constant current I and measuring the voltage drop U across the element. First, the sample was characterized electrically without microwave excitation. For the measurement of the longitudinal resistance (Fig. 5.7(a)), the current I was applied along $[1\bar{1}0]$ and the external magnetic field \vec{H}_0 along $[100]$. The negative slope of the resistance in the higher field range (inset of Fig. 5.7(a)) can be attributed to the negative magneto-resistance effect (NMR). Measurements with the external field applied along various in-plane directions (data not shown) have demonstrated that the slope does not depend on the magnetization direction, i.e. the NMR-effect is isotropic. This is also in agreement with earlier reports [74, 75] and can be explained in terms of weak localization and a magnetic field dependent scattering rate. The anisotropic magnetore-

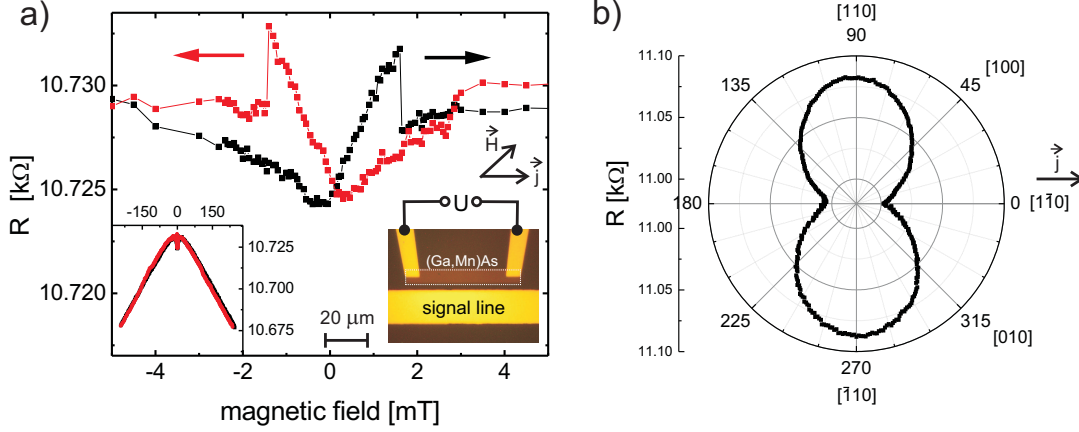


Figure 5.7: An optical micrograph of the (Ga,Mn)As element with the electrical connections is shown in the lower right side of (a). A DC-current $I = 10 \mu\text{A}$ was applied along $[1\bar{1}0]$. (a) Hysteresis of the magnetoresistance at $T = 14 \text{ K}$. The external magnetic field H_0 is swept along the $[100]$ -direction, which corresponds to an easy axis of the magnetization, compare Section 5.3. The arrows indicate the sweep direction of the external field. The inset of (a) on the lower left side shows the same measurement for the full field range of 250 mT. (b) Polar plot of the anisotropic magneto-resistance at $T = 6 \text{ K}$ obtained by rotating a magnetic field of 250 mT in the film plane. The high field is sufficient to align the magnetization exactly along the field direction, i.e. $\varphi = \varphi_H$.

sistance (AMR), which reflects the dependence of the resistance on the angle between magnetization and current direction becomes apparent both in the low (Fig. 5.7(a)) and high field range (Fig. 5.7(b)). It is convenient to define the in and out-of-plane AMR effects for the magnetization parallel and perpendicular to the film plane as follows:

$$\text{AMR}_{\parallel} = \frac{R_{[1\bar{1}0]} - R_{[110]}}{R_{[1\bar{1}0]}} \quad (5.2)$$

$$\text{AMR}_{\perp} = \frac{R_{[1\bar{1}0]} - R_{[001]}}{R_{[1\bar{1}0]}}. \quad (5.3)$$

The indices specify the magnetization direction, the current in the experiment is always applied along the $[1\bar{1}0]$ -direction. Experimentally, the two spikes at $\pm 1.5 \text{ mT}$ (Fig. 5.7(a)) can be attributed to the switching of the magnetization. The switching fields are in good agreement with static MOKE measurements on similar structures. The dependence of the resistance on the magnetization direction becomes apparent when a strong external field of 250 mT is rotated in the film plane (Fig. 5.7(b)). In agreement with earlier papers [75, 76], this (Ga,Mn)As sample C exhibits a negative AMR_{\parallel} , i.e. the lowest resistance is observed when \vec{M} is aligned parallel to \vec{j} . This behavior in the diluted magnetic semiconductor (Ga,Mn)As is opposite to the 3d-ferromagnets, where the lowest resistance is usually found when the magnetization is aligned perpendicular to the current direction. However, $\text{AMR}_{\parallel} \approx -0.7\%$ in the present sample is smaller than in the earlier report [75] of a comparable (Ga,Mn)As sample with the same thickness $t = 50 \text{ nm}$ and Mn-concentration $x = 6\%$, where $\text{AMR}_{\parallel} \approx -2\%$ was found. Empirically, the AMR-effect decreases with increasing Mn-content and after an annealing procedure, i.e. this

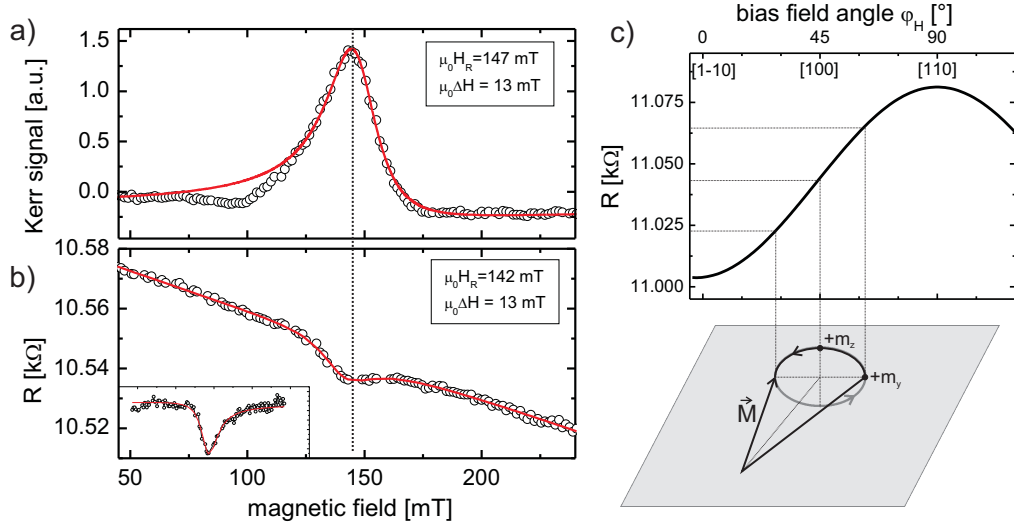


Figure 5.8: (a) Dynamic Kerr signal measured in the center of the (Ga,Mn)As element. (b) Resistance of the same element obtained in a two point measurement with constant current $I = 5\mu\text{A}$. Both measurements were performed under the same conditions (microwave frequency $f = 7.2$ GHz, $P \approx 15$ dBm, and cryostat temperature $T = 14$ K). The external field was applied along the [100]-direction. In order to highlight the resonance, in the inset the negative magneto-resistance was subtracted from the raw data. The red solid lines were obtained by fitting the experimental data to Eq. 2.28. The background from the negative magneto-resistance was taken into account by adding a negative slope ($-m \cdot H_0$) to the fit function. (c) Illustration of the precession of the magnetization with in and out-of-plane components m_y and m_z , respectively. Due to the symmetry of the AMR effect, in this configuration ($\vec{H}_0 \parallel [100]$) the contribution from the in-plane AMR vanishes. Note that for a better visualization the magnitude of the precession is strongly exaggerated, the precession angles in the experiment are typically less than 1° .

behavior may indicate that the nominal Mn-concentration is larger or the annealing procedure is more efficient than in Ref. [75].

After this static electrical characterization, the magneto-resistance in the presence of a microwave excitation with a frequency $f = 7.2$ GHz is addressed. In Fig. 5.8(b), the resonance occurs as a dip of the resistance at 140 mT. In order to verify the origin of this signal, the polar Kerr signal (Fig. 5.8(a)) was also measured in the center of the same (Ga,Mn)As element under the same conditions (temperature, microwave power, etc.). Considering the experimental sensitivity, the electrically detected resonance position $\mu_0 H_R^{\text{el}} = 142$ mT and the resonance position of the local Kerr-FMR technique $\mu_0 H_R^{\text{local}} = 147$ mT agree very well. Additional measurements at other microwave frequencies (data not shown) confirmed that the dip in the resistance signal truly originates from ferromagnetic resonance. The signal-to-noise ratio for the electrical detection of the ferromagnetic resonance is relatively low. It may be enhanced in a more sophisticated electrical measurement setup using a 4-point geometry and by applying appropriate lock-in techniques.

Now the signal magnitude for the electrically detected FMR and its physical origin are discussed. At resonance the magnetization precesses around the effective field direction.

In contrast to a time-resolved experiment such as Kerr-FMR, the temporal evolution of this precession cannot be monitored with a time-averaged electrical measurement. The precessional motion can be divided into in-plane and out-of-plane components, m_y and m_z , respectively, compare Fig. 5.8(c). The anisotropic magneto-resistance depends only on the relative orientation of \vec{M} and \vec{j} . Considering the symmetry of the AMR-effect, in the present configuration ($\vec{M} \parallel [100]$) the in-plane components of the AMR cancel out since the change of the magneto-resistance is opposite for $\pm m_y$. Therefore, only AMR_\perp contributes to the signal. Unfortunately, the magnitude of AMR_\perp could not be determined experimentally since no perpendicular fields can be applied in the present experimental setup. In the literature, however, for (Ga,Mn)As with similar Mn-concentrations a negative AMR_\perp - a higher resistance for the magnetization perpendicular to the film plane - is observed [75,77]. Under this condition, one would expect an increase of the magneto-resistance at resonance. Since in the experiment the opposite sign is observed, this indicates that the signal does not originate from the anisotropic magneto-resistance. This statement is further supported by estimating the expected AMR signal amplitude: By calculating the imaginary part of the dynamic susceptibility χ'' (Eq. 2.24), the precession angles of the magnetization can be determined. Using the experimentally determined anisotropy and damping parameters from Section 5.3 results in $\chi''_{zz} \approx 4$. The out-of-plane precession component is then given by $m_z = \chi''_{zz} \cdot h_z$ where h_z is the magnitude of the driving microwave field at the position of the magnetic element. The field distribution of the coplanar stripline is discussed in Appendix 8.3. In the current geometry the average rf-field is $\mu_0 h_z \approx 0.1$ mT. Finally, an out-of-plane precession angle $\beta_z = \tan^{-1}(m_z/M_S) \approx 0.5^\circ$ is derived. In the literature [75], for annealed $\text{Ga}_{0.94}\text{Mn}_{0.06}\text{As}$ films $\frac{\text{AMR}_\perp}{\text{AMR}_\parallel} \approx 0.8$ was found. Using this ratio to estimate AMR_\perp , the expected change ΔR at resonance therefore should be $\approx 0.05 \Omega$, which is two orders of magnitude smaller than the experimentally observed value $\Delta R = 10 \Omega$. These considerations demonstrate that neither the sign nor the signal magnitude can be explained by means of the AMR effect.

The sign of the resistance signal at FMR, however, is well explained by the absorption of microwaves which leads to a small increase of the sample temperature at resonance. A measurement of the temperature dependence of the resistance $R(T)$ (measured with low current $I_{\text{bias}} = 10 \mu\text{A}$ in order to avoid sample heating) showed that at low temperatures the resistance decreases monotonically with temperature $\frac{\Delta R}{\Delta T} = -30 \frac{\Omega}{\text{K}}$. Assuming a temperature induced change of the sample resistance, the decrease of $\Delta R = 10 \Omega$ at resonance would correspond to a temperature increase of $\Delta T \approx 0.3$ K.

In the next step the magnitude of the signal is discussed. On the one hand the power absorption at FMR can be calculated using the following expression:

$$P_{\text{rf}} = \mu_0 \pi f \chi'' h^2 V \approx 1 \mu\text{W}, \quad (5.4)$$

where $V = 70 \mu\text{m} \cdot 10 \mu\text{m} \cdot 50 \text{nm}$ is the volume of the (Ga,Mn)As element. On the other hand, one can also estimate the power which is required to explain the change of the resistance at resonance. By measuring the I-V characteristic of the sample, the resistance R can be determined as a function of electrical power $P_{\text{el}} = UI$. Due to Joule heating,

the sample resistance is not constant, but drops very rapidly for smaller power P_{el} . In fact, already $P_{\text{el}} \approx 1 - 2 \mu\text{W}$ leads to a resistance change $\Delta R = 10 \Omega$. To summarize, the estimated power due to Joule heating $P_{\text{el}} \approx 1 - 2 \mu\text{W}$ is in good quantitative agreement with the resulting power absorption due to microwave excitation $P_{\text{rf}} \approx 1 \mu\text{W}$. This confirms the purely thermal origin of the signal at resonance. Under these experimental conditions, the contribution of the AMR effect can be neglected.

Although the physical origin of the FMR signal in this experiment is a temperature induced change of the resistance, the technique is still useful to study the magnetic anisotropy and damping in micro- and nanostructures. Actually, by enhancing the sensitivity of the setup and by applying much lower microwave powers, it should be possible to observe the ferromagnetic resonance also purely by means of AMR. The reason is that the cone angles of the precession scale with the driving microwave field h , but the absorbed power (which causes the temperature increase) is proportional to h^2 . Hence, for very low h , the ferromagnetic resonance should be observable purely by means of the AMR. By combining these measurements with a static investigation of the in and out-of-plane AMR components, measurements of the absolute values of the in and out-of-plane precession angles are feasible.

At last, the advantages and disadvantages of this experimental technique are discussed. Compared to Kerr-FMR, the experimental setup is much simpler, since neither a pulsed laser source nor a scanning Kerr microscope are required. In addition, the setup may easily be implemented in a superconducting 3D vector magnet which would allow one to apply high magnetic fields in any direction. This would be very useful for the determination of the magnetic anisotropies and the damping in confined magnetic structures. One of the disadvantages is that the signal gives only the average response of the whole element, hence the technique does not allow to perform spatially resolved measurements. Finally, the sample preparation is more complex because each individual (Ga,Mn)As element has to be contacted electrically.

5.5 Magnetic relaxation mechanisms

The understanding and the control of the magnetic relaxation mechanisms in ferromagnetic materials is very important for different kinds of applications. In magnetic recording technology fast switching of the magnetization requires the control of the magnetic damping parameter. The damping also directly affects current induced magnetization switching and domain wall motion. The intrinsic damping which can be described by the damping parameter α is usually measured by determining the linewidth of the absorption peak in conventional FMR studies. However, in inhomogeneous magnetic samples the intrinsic damping can be overshadowed by extrinsic contributions, such as inhomogeneities of the magnetic properties, or two magnon scattering processes. These contributions will be discussed in detail in Section 5.5.1. It will be also explained how these contributions can be separated in angle and frequency resolved FMR measurements. In Section 5.5.3 conventional FMR absorption and local Kerr-FMR measurements are employed to draw conclusions about the homogeneity of a (Ga,Mn)As film on macroscopic

length scales. In Section 5.5.4 local Kerr-FMR measurements at a fixed sample position provide information about the magnetic homogeneity of the (Ga,Mn)As film on a sub-micrometer length scale. The experimental results are supported by micromagnetic simulations which allow an estimation of the variations of the magnetic anisotropies in a size range of hundreds of nanometers. Finally, in Section 5.5.5, the intrinsic damping in (Ga,Mn)As is discussed and compared to earlier FMR studies.

5.5.1 Intrinsic and extrinsic contributions of the FMR linewidth

The intrinsic and extrinsic contributions to the FMR linewidth will be discussed in the following. The transfer of energy and angular momentum from the spin system to the lattice (phonons) or to the electrons is considered as the intrinsic part (ΔH_{int}). Even for a perfect sample this contribution is inevitable at finite temperatures. Based on the phenomenological damping term of the LLG-equation of motion $\frac{\alpha}{M_S} \vec{M} \times \frac{\partial \vec{M}}{\partial t}$ (Eq. 2.16), the intrinsic damping parameter α can be interpreted as a viscous, velocity-dependent damping. Therefore, one would expect a linear frequency dependence of the linewidth in FMR studies. Due to extrinsic contributions, a zero frequency offset and deviations from this linear dependence are frequently found experimentally [78, 79]. These extrinsic contributions can be attributed to structural defects, which can cause for instance local variations of the magnetic anisotropy (ΔH_0) and lead to two-magnon scattering processes (ΔH_{2M}). These contributions are absent in a perfectly homogeneous sample. The inhomogeneous linewidth ΔH_0 can be understood as an extrinsic contribution due to local variations of the magnetic properties on larger length scales. As the resonance field varies from point to point, the resulting integral FMR spectrum is given by the sum of various FMR spectra which are shifted against each other. This leads to a broadening of the FMR spectrum. This extrinsic contribution to the FMR linewidth is independent of the microwave frequency, it leads to a constant linewidth offset ΔH_0 .

Two magnon scattering is a relaxation process where the uniform FMR mode is scattered into degenerate spin wave modes. This process is well known for ferrite and metallic films for several decades [80, 81] and can be understood with aid of the spin wave dispersion $\omega(k)$. In Fig. 5.9(a), a sketch of $\omega(\vec{k})$ is shown for an ultrathin magnetic film, where the wavevectors \vec{k} of the spin waves are confined to the film plane. Explicit formula for the spin wave dispersion for various orientations of the magnetization and in-plane wavevector can be found in Ref. [82]. In a ferromagnetic resonance experiment, the uniform FMR mode with angular frequency ω_0 and wavevector $\vec{k} = 0$ is primarily excited, where all magnetic moments precess in phase. When the magnetization \vec{M} and wavevector \vec{k} are aligned parallel (lower curve), $\omega(k)$ has a negative slope in the dipole dominated lower wavevector regime. For higher wavevectors (corresponding to smaller wavelengths $\lambda = \frac{2\pi}{k}$), the spin wave dispersion is dominated by the exchange interaction and increases quadratically with the wavevector. Therefore, at a certain wavevector k' , $\omega(k)$ crosses the frequency of the uniform FMR mode ω_0 , i.e. this spin wave is degenerate with the uniform mode ($\omega(k') = \omega_0$) and two magnon scattering can take place. Momentum conservation is not required due to the loss of translational invariance in

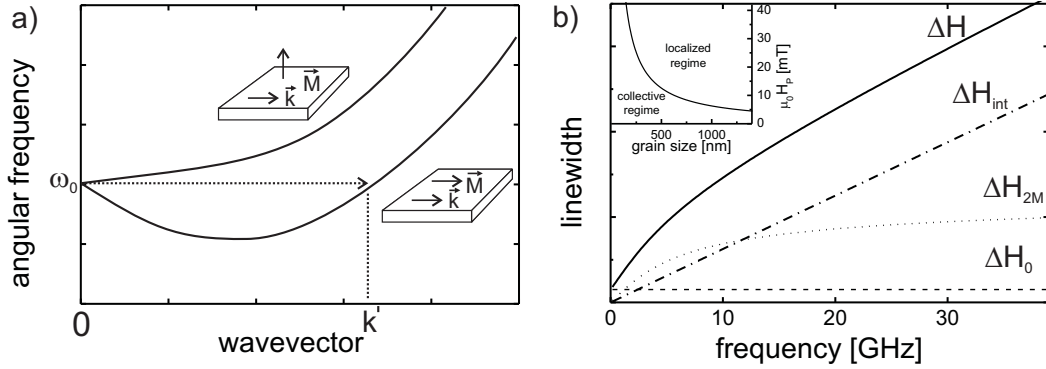


Figure 5.9: (a) Schematic diagram of the spin wave dispersion $\omega(k)$ for parallel alignment of the magnetization \vec{M} and \vec{k} in the film plane (lower trace) and for perpendicular orientation of \vec{M} with respect to the film plane (upper trace). \vec{k} is the propagation direction of the spin wave in the film plane. (b) Sketch of the frequency dependence of intrinsic and extrinsic linewidth contributions. The inset in (b) shows the calculated transition from collective to local behavior as a function of the grain size D and rms variation of the anisotropy field H_P .

a magnetic film with inhomogeneities. In contrast, when the magnetization is oriented perpendicular to the sample plane (upper curve), $\omega(k)$ increases monotonically in the entire wavevector range. Therefore no degenerate magnons are available and two-magnon scattering is suppressed.

The resulting linewidth in the FMR experiment can thus be attributed to a superposition of these intrinsic and extrinsic contributions:

$$\Delta H = \Delta H_0 + \Delta H_{2M} + \Delta H_{\text{int}} = \Delta H_0 + \Delta H_{2M}(f) + \frac{2\pi\alpha}{\mu_0\gamma}f \quad (5.5)$$

where f is the microwave frequency, and α is the dimensionless damping parameter. ΔH is defined by the half width at half maximum (HWHM) of the Lorentzian shaped resonance curves. The frequency dependence of these contributions is shown schematically in Fig. 5.9(b). While the intrinsic Gilbert damping ΔH_{int} shows a linear frequency dependence, magnetic inhomogeneities lead to a linewidth offset ΔH_0 . The contribution of two magnon scattering ΔH_{2M} does not scale linear with microwave frequency, ΔH_{2M} saturates at very high frequencies and shows a steep increase at lower frequencies [82]. The resulting FMR linewidth ΔH , which is the sum of these contributions, shows a steeper increase at lower frequencies, and has an almost constant slope at higher frequencies when the contribution of two magnon scattering saturates.

Note, that the two magnon scattering contribution in Fig. 5.9(b) serves only as an illustration, the actual $\Delta H_{2M}(f)$ -characteristics depends crucially on the orientation of the magnetization. In addition, ΔH_{2M} depends on the spin wave manifold of the magnetic film. Since two magnon scattering is associated with the Fourier components of the magnetic defects, ΔH_{2M} is also anisotropic, i.e. ΔH_{2M} depends on the orientation of the magnetization. A calculation of ΔH_{2M} is therefore very complex [82] or even impossible because the size, distribution and orientation of magnetic defects in a sample are usually unknown.

It is however important to consider how inhomogeneities of various sizes contribute to the measured FMR linewidth. In a general treatment McMichael et al. [83] have addressed this question in a grain model, where the magnetic properties are constant within each grain of average size D and the magnetic anisotropy varies randomly from grain to grain. There are two limiting cases: For very small grains in the size range of nanometers the resonance line is not affected by the inhomogeneities. This behavior can be understood in terms of the dipolar and exchange interaction, which locks neighboring magnetic moments together. Magnetic moments within a certain distance only experience and precess around an average effective field. In this scenario, the linewidth shows a linear frequency dependence, which is described solely by the intrinsic damping factor α . In the other limiting case, for very large grains, the "local resonance model" [84] can be applied, where neighboring grains are considered as independent, and the interactions between these grains can be neglected. In this scenario, the FMR spectrum is given by the sum of independent local resonance spectra. For grains in the intermediate size range (tenths of nanometers to micrometer), the inhomogeneous contribution to the linewidth is dominated by two-magnon scattering processes. McMichael et al. have also estimated the transition, where the behavior changes from the two magnon scattering dominated regime to local resonance in independent grains. Mathematically, the transition occurs when $H_p D = \pi M_S t$, where H_p is the rms variation of the anisotropy field following a Gaussian distribution, M_S is the magnetization and t is the film thickness. The resulting diagram, calculated with the parameters of the 50 nm thick (Ga,Mn)As film (sample C) is shown in the inset of Fig. 5.9(b). This graph demonstrates, that for smaller grain sizes ($D < 1\mu\text{m}$) and smaller variations of the anisotropy fields, the local resonance model does not provide a correct description of the FMR linewidth in (Ga,Mn)As and two magnon scattering processes have to be taken into account.

5.5.2 Previous studies of the FMR linewidth in (Ga,Mn)As films

The first studies of the FMR linewidth in (Ga,Mn)As films [26, 30, 85] were carried out at a single microwave frequency, therefore intrinsic and extrinsic contributions could not be distinguished. A significant decrease of the linewidth in (Ga,Mn)As films after an annealing treatment was attributed to an improved magnetic homogeneity of the sample. Subsequent FMR studies were performed in microwave cavities where only discrete microwave frequencies can be applied. In both Refs. [86, 87] two microwave frequencies ($f = 9.4$ GHz, $f = 34$ GHz) were used. ΔH_0 and α were evaluated by linear fitting these two data points under the assumption that a contribution of two magnon scattering can be neglected although it is unclear if this assumption is justified. Both for (Ga,Mn)As films on (Ga,In)As(001)-substrates [87] and for (Ga,Mn)As films on GaAs(001)-substrates with low Mn-concentration $x = 3\%$ [86], it was found that the extrinsic contributions can be as large or even larger than the contribution from the intrinsic Gilbert damping, while the linewidth offsets in a high-quality (Ga,Mn)As/GaAs(001) film with higher Mn-concentration $x = 7\%$ and after an optimized annealing treatment are significantly smaller. In addition, a strong dependence of α on temperature and magnetization direction was found in these studies. By using coplanar waveguides (cf.

Appendix 8.3), systematic studies of the FMR linewidth in a frequency range of 80 MHz to 10 GHz could be performed in this thesis, allowing one to separate the individual FMR contributions. Since in conventional FMR studies typically samples with a size of several square millimeters are investigated, it is unclear if the magnetic inhomogeneities occur on microscopic or macroscopic length scales. Inhomogeneities or gradients on a macroscopic length scale may be introduced during the LT-MBE growth or annealing of the (Ga,Mn)As films, because of varying growth conditions (sample temperature, stoichiometric ratio) at different positions of the GaAs wafer. Microscopic inhomogeneities taking place on a nanometer to micrometer length scale can be caused by the intrinsic random distribution of the Mn-atoms, point defects, Mn-clusters, local depletion of holes, etc. These topics will be addressed in the following two sections by making use of the local Kerr-FMR technique.

5.5.3 Homogeneity of the magnetic properties on macroscopic length scales

In this section, the Kerr-FMR technique is employed to investigate the magnetic relaxation mechanisms locally. In combination with a simultaneous measurement of the FMR absorption of the whole sample this offers the opportunity to determine the length scale on which inhomogeneities of the magnetic properties occur. Before the discussion of the experimental results, one should point out that due to the sample design and experimental geometry, which were introduced in Section 5.1, different effects may lead to an artificial broadening of the inductive FMR-absorption spectra: First of all, the external magnetic field has a gradient of $\approx 1\%$ per mm, the resulting line broadening of ≈ 0.1 mT can, however, be neglected. Secondly, strain-relaxation induced changes of the magnetic anisotropies (compare Chapter 6 and Refs. [10, 11]) at the boundary of the $50\ \mu\text{m}$ wide and 1 mm long element lead to laterally non-uniform resonance conditions affecting $\approx 5\%$ of the total sample volume. However, in the FMR spectra this boundary region becomes mainly visible as a second less pronounced peak or shoulder. By excluding this peak in the fitting process, the linewidth of the main peak should be unaffected. More importantly, since the coplanar wave guide partially covers the (Ga,Mn)As element (cf. Fig. 5.1(a)), microwave losses in the $30\ \mu\text{m}$ wide signal line can lead to an inhomogeneous temperature distribution in the (Ga,Mn)As element. Due to the strong temperature dependence of the anisotropies (cf. Section 5.3), this leads also to non-uniform resonance conditions which is expressed by a line broadening. A test measurement with much lower microwave power (-20 dB), where these temperature variations are negligible, showed a narrowing of the FMR spectrum of ≈ 1.5 mT. In conclusion, only a microwave induced temperature variation leads to a significant line broadening of ≈ 1.5 mT in the inductive measurements. In Fig. 5.10 the results of the local and integral measurements are summarized. The magnetic properties of this annealed 50 nm thick (Ga,Mn)As film (sample C) were already discussed in Section 5.3. Once again, it should be emphasized, that the results of the local Kerr-FMR technique reflect the local magnetic properties within the laser spot ($\approx 1\ \mu\text{m}^2$), while the inductive

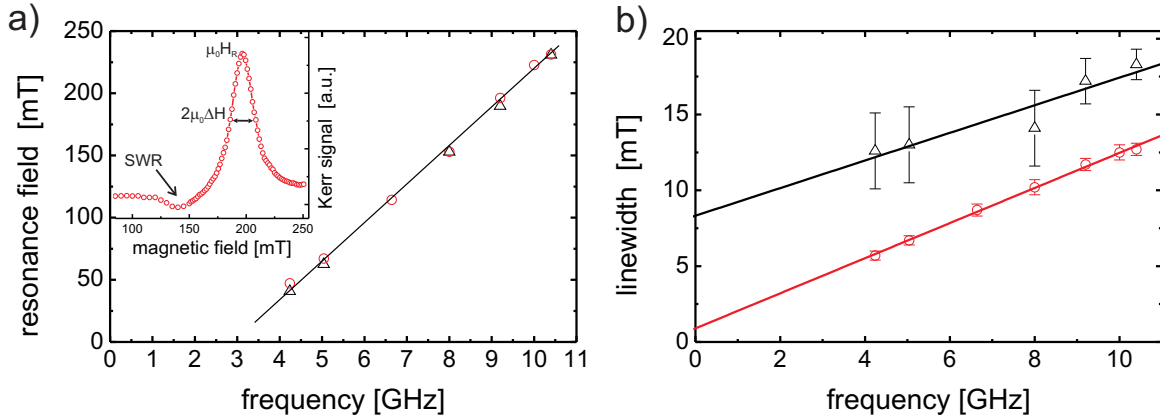


Figure 5.10: Inset of (a): Example of a typical Kerr-FMR spectrum ($f = 9.2$ GHz, $T = 8.5$ K), illustrating the resonance position H_R and the linewidth ΔH . The measurements were performed using the same (Ga,Mn)As film (sample C) and experimental approach as described in Section 5.1. (a) Resonance fields $\mu_0 H_R$ and (b) linewidths $\mu_0 \Delta H$ as a function of microwave frequency determined in local (red circles) and integral (black triangles) FMR measurements for $T = 8.5$ K and $H \parallel [100]$. The line in (a) is just a guide to the eye. The lines in (b) are linear fits to the experimental data. The error bars in (b) were obtained by analyzing the agreement of the fit function with the experimental data. The integral FMR spectra show a second less pronounced peak close to the main resonance which is probably related to strain relaxation effects at the boundary of the $50 \mu\text{m}$ wide stripe. In combination with the much lower SNR compared to local Kerr-FMR, this leads to larger error bars.

technique (microwave absorption) reflects the average properties of the 1 mm long and $50 \mu\text{m}$ wide (Ga,Mn)As element. A typical Kerr-FMR spectrum is given in the inset of Fig. 5.10(a). The main resonance at $\mu_0 H_R = 195$ mT corresponds to the uniform precession of the magnetization, where all magnetic moments precess in phase. As discussed in Section 5.1, the second less pronounced peak at $\mu_0 H_{\text{SWR}} = 140$ mT can be attributed to a spin wave resonance (SWR). Local and inductive FMR spectra were measured for several microwave frequencies, the resulting resonance fields $H_R(f)$ and linewidths $\Delta H(f)$ of the main resonance are plotted in Fig. 5.10. The local and inductive resonance fields agree quantitatively very well (Fig. 5.10(a)), while the linewidths differ significantly (Fig. 5.10(b)). In addition, both $\Delta H(f)$ curves show an almost linear dependence, indicating that a contribution of two-magnon scattering to the linewidth is small and can be neglected for the analysis of the experimental data ($\Delta H_{2M} = 0$). By linear fitting the $\Delta H(f)$ -data the zero frequency offsets of the linewidths ΔH_0 are obtained which represent the linewidth contribution due to local magnetic inhomogeneities. The resulting linewidth offset $\mu_0 \Delta H_0 = 0.7 \pm 0.4$ mT of the local Kerr-FMR measurement is much smaller than the integral linewidth $\mu_0 \Delta H_0 = 8 \pm 3$ mT indicating that magnetic inhomogeneities play only a minor role on a lateral length scale below one micrometer. Also after consideration of the above discussed artificial line broadening of ≈ 1.5 mT, the inductive linewidth is one order of magnitude larger. In order to backup these findings, conventional FMR measurements were performed on a different piece ($\approx 20 \text{ mm}^2$) of the same (Ga,Mn)As wafer in another low temperature FMR setup. Due to inhomogeneous growth and annealing processes, the magnetic proper-

ties of both sample pieces are somewhat different, nevertheless the linewidth offset of $\mu_0\Delta H_0 = 5.8$ mT ($H \parallel [100]$, $T = 10$ K) is in good quantitative agreement with the linewidth above ($\mu_0\Delta H_0 = 8$ mT), when the heating induced line broadening is subtracted. It is important to note, that the local linewidth offset $\mu_0\Delta H_0 = 0.7 \pm 0.4$ mT is also much smaller than $\mu_0\Delta H_0 \approx 4.3$ mT ($H \parallel [100]$, $T = 20$ K) in the earlier FMR studies of Khazen et al. [87], where a macroscopic film of higher Curie temperature $T_C = 157$ K was investigated. This is an additional indication that gradients or fluctuations of the magnetic properties in (Ga,Mn)As mainly take place on macroscopic length scales (micrometer to millimeter size range).

The scanning Kerr microscopy technique offers also the opportunity to measure FMR spectra at different sample positions (x,y), therefore the sample homogeneity can also be investigated on larger length scales. By fitting the individual FMR spectra to Lorentzian functions, the resonance fields $H_R(x, y)$ were determined for each lateral position (x,y). Because of locally varying magnetic properties, the resonance fields vary from point to point. In Fig. 5.11(a), statistics of H_R are given for the high symmetry in-plane directions. The distributions of H_R clearly show that because of locally varying magnetic properties also the resonance fields are varying locally, explaining the significant broadening of the spectra in the FMR absorption measurements above. The narrowest distribution is found for $H \parallel [100]$, which corresponds to the easy axis of the cubic anisotropy, while the distributions along $[1\bar{1}0]$ and $[110]$ are significantly broader. Shifts of the resonance fields can be caused by variations of the anisotropy constants $K_{U\perp}$, $K_{C\parallel}$, $K_{U\parallel}$, magnetization M and gyromagnetic ratio γ , compare the FMR condition (Eq. 2.19). However, a lateral variation of M , γ and $K_{U\perp}$ would lead to the same width of the resonance field distribution for all three field directions in the film plane. Therefore, the different widths of the distributions in Fig. 5.11(a) can only be attributed to lateral variations of the in-plane anisotropies $K_{C\parallel}$ and $K_{U\parallel}$. Since variations of the cubic anisotropy $K_{C\parallel}$ have only a minor influence on the distributions along the $[110]$ and $[1\bar{1}0]$ directions, the broader distributions along these directions demonstrate that the lateral variation of the uniaxial in-plane anisotropy $K_{U\parallel}$ is more pronounced than the variation of the cubic anisotropy.

In conclusion, the comparison of inductive and local FMR linewidths and measurements of the resonance field distributions along various crystallographic directions have demonstrated that the magnetic properties of (Ga,Mn)As films are very inhomogeneous on micrometer to millimeter length scales. In conventional FMR measurements of (Ga,Mn)As films this behavior is expressed by a significant broadening of the spectra.

5.5.4 Homogeneity of the magnetic anisotropies on a sub-micrometer length scale

In addition to the determination of the homogeneity of the sample on macroscopic length scales, measurements of the linewidth at a fixed sample position can be used to draw conclusions about the homogeneity of the magnetic anisotropies on a smaller length scale ($< 1\mu\text{m}$). For this purpose, the frequency dependence of the linewidth $\Delta H(f)$

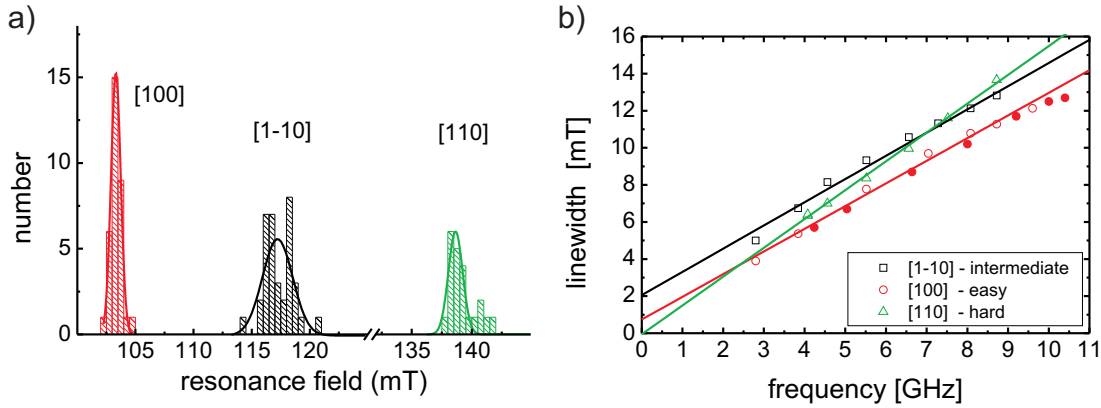


Figure 5.11: (a) Distributions of the local resonance fields at $f = 6.0$ GHz and $T = 10$ K determined by measuring FMR spectra at different sample positions. The solid lines are gaussian fits to the experimental resonance field distributions. Since the measurement positions covered only a small fraction ($< 1\%$) of the total sample area, the integral FMR spectrum (microwave absorption of the whole sample) cannot be reproduced by summing all individual local spectra. (b) Linewidths (HWHM) measured at a fixed sample position of the $50\ \mu\text{m} \times 1\ \text{mm}$ large (Ga,Mn)As element as a function of the microwave frequency for various crystallographic directions. The measurements (open symbols) were performed at $T = 10$ K and with low rf-power $P \approx 3$ dBm in order to minimize microwave induced sample heating. The experimental data from Fig. 5.10(b) for a marginally lower temperature of 8.5 K and a slightly higher microwave power is given by the full circles. The solid lines are linear fits to the experimental data.

was determined for various crystallographic directions, see Fig. 5.11(b). One can clearly observe, that the extrapolation of the experimental $\Delta H(f)$ data to zero frequency differs for the individual field directions. In addition, a linear increase of the $\Delta H(f)$ data is found for the [100] and [110] orientations, while $\Delta H(f)$ deviates from the linear dependence when the magnetization is aligned along the $[1\bar{1}0]$ orientation. This behavior is an indication of a contribution of two magnon scattering. The available experimental data in this frequency range is not sufficient to determine the contribution of two magnon scattering ΔH_{2M} quantitatively. Indeed, because of the relatively small curvature of the $\Delta H(f)$ data, two magnon scattering seems to play only a minor role. Therefore, for the following analysis of the intrinsic damping factors α and linewidths offsets ΔH_0 , the contribution of two magnon scattering was assumed to be zero ($\Delta H_{2M} = 0$). The parameters ΔH_0 and α were therefore determined by linear fitting the experimental data, see table 5.2. The different linewidth offsets for various crystallographic directions hint at a local variation of the magnetic anisotropies within the laser spot diameter. An estimation of the amplitude of the lateral homogeneity of the anisotropies on this sub-micrometer length scale will be given in the following. It is important also to consider, how inhomogeneities along the growth direction [001] contribute to the measured FMR linewidth. The penetration depth of the probe beam is much larger than the film thickness $t = 50$ nm (cf. Section 5.6.2), implying that the magnetic properties perpendicular to the film plane [001] are probed uniformly. Because the exchange length $l_{ex} = 18$ nm (cf. Section 5.1) and the film thickness of $t = 50$ nm are of comparable size, the magnetic moments across the film thickness can be consid-

	α	$\mu_0\Delta H_0$ [mT]
[$\bar{1}\bar{1}0$]	0.035 ± 0.003	2.1 ± 0.5
[100]	0.034 ± 0.002	0.7 ± 0.4
[110]	0.043 ± 0.001	-0.1 ± 0.3

Table 5.2: Damping constants α and linewidth offsets ΔH_0 at $T = 10$ K determined by linearly fitting the experimental data in Fig. 5.11(b).

ered as strongly coupled. As a result even very large gradients or inhomogeneities of the magnetic properties along the growth direction do not significantly affect the measured linewidth. Therefore, the local measurements are mostly sensitive to the magnetic homogeneity laterally in the film plane.

Since the size of the magnetic grains (regions with homogenous magnetic properties) has to be smaller than one micrometer (laser spot diameter $\approx 1 \mu\text{m}$), the simple 'local resonance model' (cf. Section 5.5.1) can not be employed to estimate the influence of magnetic inhomogeneities on the FMR linewidth. It is important to note that in the present context the term 'grain' only refers to the magnetic homogeneity of the sample. It is not associated with structural grains, since the studied (Ga,Mn)As films are grown epitaxially on GaAs substrates. In order to determine the variations of the magnetic properties for the present (Ga,Mn)As film, micromagnetic simulations were performed using the Object Oriented MicroMagnetic Framework code (OOMMF) [88]. The simulations were carried out on a square grid with a cell size $10 \text{ nm} \times 10 \text{ nm} \times 50 \text{ nm}$. All relevant parameters of the simulated (Ga,Mn)As film, such as magnetization ($\mu_0 M_S = 42 \text{ mT}$), anisotropies ($K_{U\perp} = -3 \times 10^3 \frac{\text{J}}{\text{m}^3}$, $K_{U\parallel} = 1 \times 10^2 \frac{\text{J}}{\text{m}^3}$, $K_{C\parallel} = 2 \times 10^3 \frac{\text{J}}{\text{m}^3}$), intrinsic damping factor ($\alpha = 0.035$), exchange constant ($A = 5 \times 10^{-13} \frac{\text{J}}{\text{m}}$) are known from local FMR and SQUID measurements. The variations of the magnetic properties on a sub-micrometer length scale, however, are unknown. Indeed, there are several experimental indications, which justify the usage of the average grain size $D = 200 \text{ nm}$: One can exclude that the actual grain size is larger than the laser spot size, because the linewidth offset $\Delta H_0 \parallel [100]$ is finite. Furthermore, since the experimental FMR spectra can be fitted to a single Lorentzian peak (cf. Fig. 5.1(b)), more than just a few grains have to be present in the probed sample area of $\sim 1 \mu\text{m}^2$. Finally, it is also hard to imagine, that very small grains in the range of nanometers or a few tenths of nanometer cause the experimentally observed linewidth offset ΔH_0 , since this would require extremely large variations of the magnetic properties, compare the inset of Fig. 5.9(b) and Refs. [83, 89]. As a consequence, the assumption of grains with average sizes of 50-300 nm seems most promising. In the simulations, all parameters with the exception of the cubic anisotropy constant $K_{C\parallel}$ are assumed to be spatially uniform due to the following reasons: Due to symmetry reasons, lateral variations of the perpendicular anisotropy $K_{U\perp}$, g-factor and magnetization M would lead to the same inhomogeneous linewidth for any in-plane orientation of the magnetization. Because ΔH_0 is approximately zero for the [110]-direction (table 5.2), larger variations of these magnetic parameters can be excluded. Furthermore, variations of the uniaxial in-plane anisotropy $K_{U\parallel}$ would only marginally affect the linewidths along the [100]-direction indicating that ΔH_0 is mainly caused by

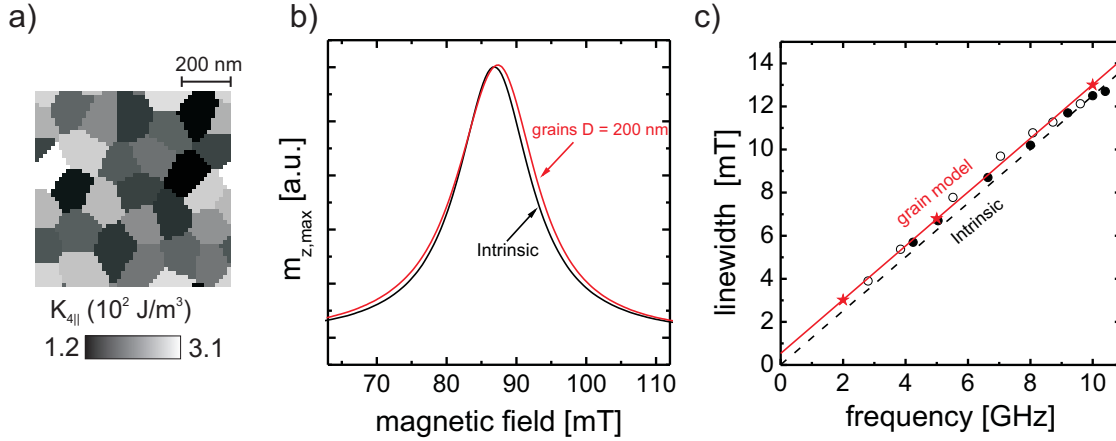


Figure 5.12: (a) Map of the cubic anisotropy constant $K_{C\parallel}(x, y)$ used for the micromagnetic simulations of the FMR spectra. $K_{C\parallel}$ follows a gaussian distribution with a rms variation of 25%. The simulations were performed for a $1\ \mu\text{m} \times 1\ \mu\text{m}$ large sample, comparable to the size of the probe laser spot. (b) Examples of simulated FMR spectra for $f = 5\ \text{GHz}$ both for a homogeneous film (characterized by the intrinsic damping factor α) and for the interacting grain structure. In the simulation, the external magnetic field was aligned along the easy axis of the cubic anisotropy [100], the rf-driving field \vec{h} pointed along the [001]-direction, i.e. perpendicular to the film plane. (c) Frequency dependence of the linewidth (HWHM) for the homogeneous film (dotted line) and the simulation of the coupled grains (red stars). The red solid line is a linear fit to the linewidth of the grain model. Experimental data from Fig. 5.11(b) are plotted as circles.

a variation of $K_{C\parallel}$.

In Fig. 5.12(a), the grain structure representing the lateral distribution of $K_{C\parallel}$ is shown. Within each grain of average size $D \approx 200\ \text{nm}$, all magnetic parameters are constant. $K_{C\parallel}$ varies randomly from grain to grain, the rms variation of $K_{C\parallel}$ is 25%. In Fig. 5.12(b) representative FMR spectra for $f = 5\ \text{GHz}$ are plotted both for the simulated grain structure and for a homogenous sample, where the linewidth is solely determined by the intrinsic damping factor ($\mu_0\Delta H = 2\pi\alpha f/\gamma$). One can observe a marginal upward shift of the resonance field and a line broadening of $\approx 0.5\ \text{mT}$ for the grain simulation. In order to compare the simulations with the experimental $\Delta H(f)$ data, FMR spectra were simulated for three microwave frequencies. In Fig. 5.12(c), the simulated linewidths (red stars) are compared to the linewidths for homogeneous magnetic properties (dashed line) and to the experimental linewidths (dots). One finds that the $\Delta H(f)$ data in the grain model is shifted by a small constant offset $\mu_0\Delta H_0 \approx 0.5\ \text{mT}$ upwards with respect to the intrinsic damping curve. From Fig. 5.12(c), it is also apparent that the grain simulation provides a good description of the experimental linewidths.

These results demonstrate that beside the magnetic inhomogeneity of (Ga,Mn)As films on larger length scales (micrometer to millimeter-range), magnetic defects occur also on a submicrometer length scale. This behavior is also expressed by a small contribution of two magnon scattering in the $\Delta H(f)$ data. Furthermore, the comparison of the experimental data with micromagnetic simulations hints at a rms variation of the cubic anisotropy of few tenths of percents.

Finally, the temperature dependence of the inhomogeneous linewidth is discussed. For

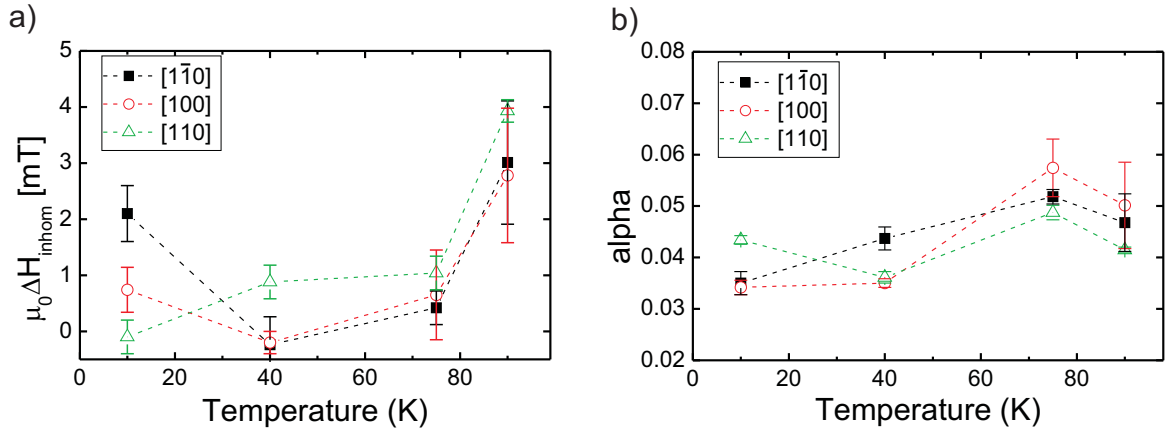


Figure 5.13: Linewidth offset ΔH_0 (a) and damping parameter α (b) as a function of temperature for various orientations of the applied field. The parameters were determined by performing linear fits of the frequency dependence of the experimentally determined linewidth. The error bars represent the agreement of the experimental data with the linear fit.

this purpose, $\Delta H(f)$ was measured at various temperatures. By linear fits to the experimental $\Delta H(f)$ data, $\Delta H_0(T)$ and $\alpha(T)$ were determined. Hence it is assumed that the contribution of two magnon scattering ΔH_{2M} can be neglected, compare Fig. 5.13. The same temperature characteristics as in Ref. [87] are observed for the inhomogeneous linewidth. ΔH_0 decreases to almost zero at $T = 40$ K and $T = 75$ K and rises when approaching the Curie temperature $T_C = 110$ K. Since the magnetic anisotropy constants decrease with increasing temperatures (cf. Section 5.3), also spatial inhomogeneities of the anisotropies are reduced leading to smaller lateral variations of the resonance fields. Therefore, a decrease of ΔH_0 is found in this intermediate temperature range. In the vicinity of the Curie temperature already small fluctuations of the atomic composition and of the hole concentration can have a drastic effect on the magnitude and orientation of the anisotropies, explaining the increase of ΔH_0 . One can also observe that the behavior of the linewidths offsets along the $[1\bar{1}0]$ and $[110]$ -directions reverses at higher temperatures, i.e. at $T = 10$ K the zero frequency offset ΔH_0 along $[1\bar{1}0]$ is larger than along $[110]$, while for $T \geq 40$ K the opposite trend is observed. These temperature dependencies might be attributed to the temperature induced reorientation of the uniaxial in-plane anisotropy, whose easy axis rotates from the $[1\bar{1}0]$ to the $[110]$ orientation, compare the temperature dependent studies of the anisotropies in Section 5.3.2.

5.5.5 Intrinsic damping in (Ga,Mn)As films

Finally, the intrinsic damping in (Ga,Mn)As is discussed, which is represented by the dimensionless damping parameter α . It is important to note that α must be understood as an intrinsic material parameter which is independent of the sample homogeneity. Sinova et al. [85] have calculated the damping parameter of (Ga,Mn)As in a theoretical model, where the relaxation of the localized Mn-spins is transferred to the hole system by means of the p-d-exchange interaction. In the valence bands the moments of the holes are relaxed through intraband and interband transitions, therefore the damping factor

should depend crucially on the characteristics of the complex valence band structure. For constant Mn-concentration x , the theory predicts an increase of α with increasing hole concentration p . The dependence of α on the Mn-concentration is however more complex and depends on an adjustable parameter, the 'quasiparticle lifetime'. For the present sample with $x = 0.06$ and $p \approx 4 \times 10^{20} \text{cm}^{-3}$, the theory predicts $\alpha = 0.02 - 0.025$ which is in reasonable agreement to the experimental damping parameter $\alpha = 0.035 - 0.045$ at low temperature. However, Khazen et al. [87] reported $\alpha = 0.003 - 0.007$ for a (Ga,Mn)As film with a Mn-content $x = 0.07$ and unknown, but probably very high hole concentration because of the high Curie temperature $T_C = 157$ K. This value is one order of magnitude lower than predicted by Sinova et al., where α should lie between 0.02 and 0.04. The present experimental data is not yet sufficient to decide whether the model provides a good description of the intrinsic damping in (Ga,Mn)As.

The one order of magnitude larger damping parameter of the present film compared to the film of Khazen [87] may be related to the different Mn- and hole concentrations of these films. Both the experimental reports addressing the intrinsic damping in (Ga,Mn)As [86,87] and the present experimental observations indicate that α decreases with increasing Mn- and hole concentration. As an example, for the (Ga,Mn)As film D with very high Mn concentration $x = 12.5\%$ (characterized in Section 5.3), a very small damping parameter $\alpha = 0.003 - 0.005$ was determined in conventional FMR measurements at $T = 20$ K. In contrast to the earlier reports of Khazen et al. [87] and Matsuda et al. [86], the intrinsic damping parameter α is only slightly anisotropic in the present (Ga,Mn)As film C, α is very similar for the different in-plane directions, compare table 5.2. It is even conceivable that the small anisotropy of α is a consequence of a contribution of two-magnon scattering, which was neglected in the present analysis. Especially in the investigated lower frequency range a contribution of two-magnon scattering can lead to erroneous results of the intrinsic damping factor, when α is determined by the slope of the $\Delta H(f)$ -data. FMR studies of the linewidth at much higher microwave frequencies, where the intrinsic damping is dominant, would very useful to support this statement.

The temperature dependence of the intrinsic damping factor α is shown in Fig. 5.13(b). In contrast to the results of Khazen et al. [87], where α increases with temperature by a factor of 2-3, α increases only weakly with temperature. In addition, it is rather striking that α does not show any significant dependence on the crystallographic directions in the film plane in the whole temperature range. A deeper consideration of the intrinsic damping mechanisms in (Ga,Mn)As is however beyond the scope of this thesis. A more detailed discussion of this topic will be given in the PhD-thesis of M. Kiessling.

5.5.6 Conclusion

In conclusion, local and integral measurements of the FMR linewidth have demonstrated, that inhomogeneities of the magnetic properties in (Ga,Mn)As mainly occur on macroscopic length scales. Presumably, the much larger linewidth offsets in earlier FMR studies of macroscopic (Ga,Mn)As films can be ascribed to gradients or inhomogeneities of the sample properties on a micrometer to millimeter length scale, generated during

the growth or annealing process (e.g. local variations of the growth and annealing conditions, such as temperature, stoichiometric ratio, etc.). This is supported by the fact, that the *local* linewidth offset in the present sample is the by far lowest of all reported values in (Ga,Mn)As. The spatially resolved FMR measurements indicate that the magnetic inhomogeneities on these larger length scales can be mainly attributed to a variation of the uniaxial in-plane anisotropy $K_{U\parallel}$. The local Kerr-FMR studies have revealed, that inhomogeneities of the magnetic anisotropies occur also on a smaller lateral length scale in the range of a few hundreds of nanometers. These inhomogeneities most likely occur due to smaller variations of the hole and Mn-concentrations. The comparison of the experimental results with a simple grain model indicates that the magnetic inhomogeneities on this sub-micrometer length scale are mainly caused by a lateral variation of the cubic in-plane anisotropy $K_{C\parallel}$. Furthermore, the frequency dependent measurements of the linewidth showed a signature of a small contribution of two-magnon scattering processes. This extrinsic damping mechanism was neglected in the analysis of the earlier FMR studies of (Ga,Mn)As films. In order to separate extrinsic and intrinsic contributions of the linewidth in (Ga,Mn)As films unambiguously, FMR studies in a much higher frequency range of several tenths of gigahertz and in the perpendicular field orientation, where two-magnon scattering is suppressed, would be very valuable. Finally, it was found that the intrinsic damping parameter is relatively isotropic and lies in the range $\alpha = 0.034 - 0.043$ at low temperatures. The present experimental data indicate that α decreases both with increasing hole and Mn-concentration. Further systematic investigations of films with various Mn- and hole concentrations would be very useful in order to get an even better understanding of the intrinsic damping mechanisms in (Ga,Mn)As.

5.6 Time-resolved experiments

Both theoretical considerations [37] and experimental results [38] have demonstrated that the ferromagnetic properties of (Ga,Mn)As depend crucially on the carrier concentration. The manipulation of the magnetic properties by variation of the hole concentration in (Ga,Mn)As has been addressed both in static and dynamic experiments. Employing static magnetotransport measurements, Chiba et al. [7] have demonstrated that the easy axis of the magnetization can be rotated by varying the hole concentration using a strong electric field. Recently, also SQUID measurements [8] in a metal/insulator/semiconductor structure have shown the crucial influence of the hole concentration on magnetic properties like Curie temperature. This effect also offers the opportunity to manipulate the magnetization on short time scale by using femtosecond light pulses. Fast processes in (Ga,Mn)As have been investigated by various groups using pump-probe experiments. For high pump power, the reduction of the magnetization (demagnetization) occurring on a subpicosecond time scale has been demonstrated [90]. For low pump power and at longer time scales, Wang et al. [13] reported an inverse effect: a photoinduced increase of the magnetization on a time scale of several hundreds of picoseconds. This temporary enhancement of ferromagnetism is ascribed to pump-induced transient holes. However, such a behavior is controversially discussed, because the ori-

gin of the signal in these pump-probe experiments is unclear. It is well established [58], that the magneto-optical signal in these ultrafast experiments consists of a nonmagnetic part, due to a photoinduced change of the refractive index, and of a magnetic part due to a change of the magnetization length and direction. Rozkotová et al. [91–93] performed systematic pump-probe measurements in (Ga,Mn)As, using different pump and probe beam polarizations, and wavelengths, and measured the reflectivity change of the sample. The authors found that only the oscillatory component of the magneto-optical signal can be linked to the ferromagnetic order in (Ga,Mn)As. This demonstrates that the measured signal is not necessarily proportional only to the magnetization.

In Ref. [12] the precession of the magnetization was launched with a short optical pump pulse. Using the same line of arguments as Wang et al. [90], the authors proposed that the weak pump pulse introduces photoexcited holes, which lead to a non-thermal change of the magnetic anisotropies. The verification of this statement is based on a modeling of the magneto-optic signal by using trial functions of the effective field. Due to the measurement geometry, both polar magneto-optic Kerr effect and the magnetic linear dichroism contributed to the signal. Since the relative strength and the wavelength dependencies of these two effects were unknown, the magneto-optical constants were used as free parameters. In combination with the unknown temporal and spatial dependence of the effective field $H_{\text{eff}}(x, y, z, t)$, a large number of unknown parameters was involved. An accurate reconstruction of the temporal dependence of the effective field is thus not possible. Therefore, also a thermal influence of the pump beam cannot be excluded.

In summary, conventional pump-probe experiments do not provide a quantitative access to the magnetic anisotropies and thus do not allow to draw quantitative conclusions about the effects of photoexcited holes on the magnetic anisotropies. In addition, the magneto-optic response in all-optical experiments has to be analyzed very carefully. Since ferromagnetic resonance is one of the most powerful techniques for the determination of magnetic anisotropies, pump-probe and the FMR techniques are combined, in order to study the role of photoexcited holes on the anisotropies and the magnetization. The ambiguous nature of the magneto-optical response is circumvented, since not relative changes of the magnetization components are measured, but absolute shifts of the resonance fields. The reliability of the local FMR technique was already demonstrated in Section 5.1. Before combining both experiments, the reliability of the pump-probe technique will be verified in the subsequent section.

5.6.1 All-optical pump-probe measurements

This section addresses all-optical pump-probe measurements, where both the excitation of the magnetization dynamics and the determination of the magnetization direction, are performed optically. Instead of the continuous wave excitation of the magnetization with rf-fields like in a ferromagnetic resonance experiment, the magnetization dynamics is launched by a short optical pump pulse. The excitation process and the temporal evolution of the magnetization is described schematically in Fig. 5.14(a)-(c). The mechanisms which trigger the precession of the magnetization will be discussed in the following. The pump pulse induces several effects which take place on different time

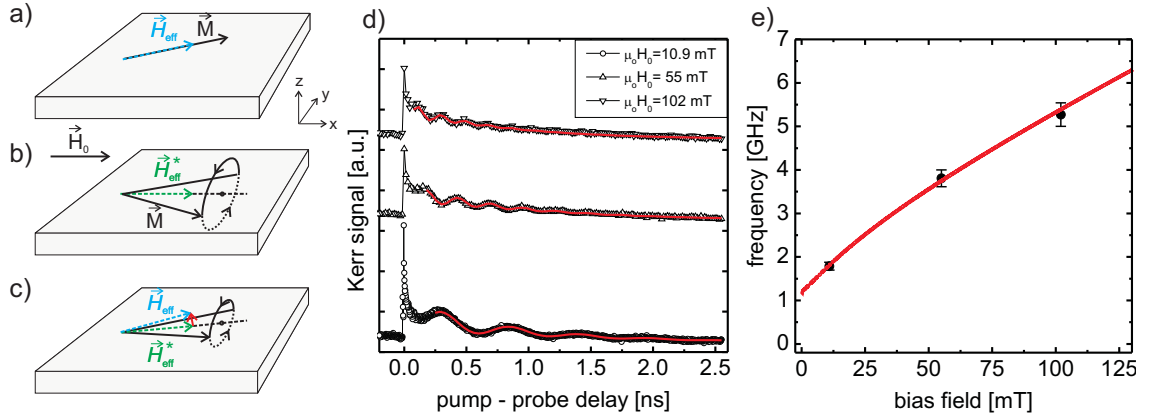


Figure 5.14: Schematic illustration of the excitation process and the precessional motion of the magnetization. (a) Before the arrival of the pump pulse the magnetization \vec{M} is aligned along the effective field direction \vec{H}_{eff} , which is the sum of external magnetic field \vec{H}_0 and anisotropy field \vec{H}_{ani} . (b) The pump pulse leads to a change of the magnetic anisotropies which results in the new effective field direction \vec{H}_{eff}^* . The non-parallel alignment of \vec{M} and \vec{H}_{eff}^* leads to a torque $\vec{T} = \vec{M} \times \vec{H}_{\text{eff}}^*$ and the magnetization starts to precess around \vec{H}_{eff}^* . In (c) \vec{H}_{eff}^* starts to turn back toward its equilibrium direction \vec{H}_{eff} . After a certain relaxation time, also the magnetization has returned to its equilibrium position. (d) Experimental data showing the temporal evolution of the Kerr signal for the 50 nm thick (Ga,Mn)As sample C, at $T = 6$ K, at a pump wavelength $\lambda = 404$ nm and pump fluence $F \approx 0.5 \frac{\text{mJ}}{\text{cm}^2}$. The external DC field is applied along $\varphi_H = -35^\circ$. The curves are vertically offset for clarity. The red solid lines represent the fits to Eq. 5.6. (e) Precession frequencies versus the external magnetic field (symbols). The solid line was calculated using Eq. 2.19 and the anisotropy parameters determined with local FMR on the same sample (table 5.1).

scales: First, provided that the pump pulse is sufficiently intense, the magnetic system can be partially demagnetized, it was shown that this process in (Ga,Mn)As occurs on a subpicosecond time scale [90]. However, this effect cannot trigger the precession, because the magnetization is aligned in the film plane. A change in the effective field (due to a change of the demagnetizing field) only occurs, if the magnetization is tilted away from the film plane. Second, the pump induced sudden change in the sample temperature ΔT can lead to a fast change of the magnetic anisotropies. Finally, as discussed in the previous section, also the additional photoexcited holes Δp can modify the ferromagnetic properties of (Ga,Mn)As, such as the magnetic anisotropies. The last two effects can lead to a change in the effective field direction \vec{H}_{eff} , which exerts a torque on the magnetization and induces the precessional motion. The high pump fluence in the experiment suggests, that the excitation mechanism is a mixture of hole- and temperature induced changes of the anisotropies. A quantitative consideration of ΔT and Δp will be given in Section 5.6.3.

The measurement setup and procedure are described in detail in Section 4.5. The fundamental near infrared beam ($\lambda = 808$ nm) of the Ti-Sapphire oscillator is used to probe the magnetization component perpendicular to the film plane, while the frequency doubled blue beam ($\lambda = 404$ nm) is used for the excitation. Both pump and probe beam are linearly polarized and impinge on the sample in normal incidence. The spot sizes

of both beams of $2.5 \mu\text{m}$ are determined by scanning over the edge of a microstructure. The pump fluence ($\approx 0.5 \frac{\text{mJ}}{\text{cm}^2}$) and the probe fluence ($\approx 0.1 \frac{\text{mJ}}{\text{cm}^2}$) are at least one order of magnitude larger than in recent studies [12, 13]. Changes of the probe fluence did not affect the precession frequencies, which demonstrates that the probe beam does not change the sample temperature significantly. Fig. 5.14(d) shows examples of typical pump-probe measurements. First of all, the temporal evolution of the Kerr signal is discussed: A fast rise of the signal (risetime < 1 ps) followed by an exponentially damped oscillation is observed. The increase of the signal shortly after the excitation cannot be associated with a demagnetization of the sample, because changes of the magnetization in the film plane are not detected in a polar measurement geometry. The ultrafast heating of the sample leads to abrupt changes of the optical indices which also modifies the probe beam polarization [58]. These ultrafast processes on a femtosecond to picosecond time scale will not be treated here, for a more detailed discussion refer to Refs. [90, 94]. After the initial rise of the signal, a superposition of a slow decay and a pronounced damped oscillation is found. The slower decay of several nanoseconds may be related to the slow diffusion of heat from the pump spot. Since the frequency of the oscillation depends on the external field (Fig. 5.14(e)), it can be attributed to the precession of the magnetization. Due to magnetic relaxation and dephasing effects, the precession damps out after several cycles. The smaller amplitude of the precession for larger magnetic fields can be understood easily: The effective field is the sum of internal fields such as anisotropy field, and external field. The internal field is changed by the pump pulse, but the external field is independent of the excitation. I.e. for a larger external field, the change in the anisotropy field is less important and the torque on the magnetization decreases, which in turn yields a smaller precession amplitude. The precession frequencies in Fig. 5.14(e) were obtained by fitting the experimental data to an exponentially damped sine function:

$$y(t) = A \sin(2\pi ft + \varphi) \cdot \exp(-t/\tau_1) + B \exp(-t/\tau_2) \quad (5.6)$$

where A is the amplitude of the oscillation, f and τ_1 are the frequency and the decay time of the precession. The second exponential function with the decay time τ_2 accounts for the slower background signal. Since the experimental data in the time range 0.1 ns to 2.5 ns can be well fitted using a single precession frequency, the sample temperature does not seem to change significantly. In Fig. 5.14(e), the resulting precession frequencies are compared quantitatively to the local FMR measurements from Section 5.3. The perfect agreement of both measurement techniques demonstrates that the all-optical approach can be used to study the magnetization dynamics in the time domain. The large repetition rate $f_{\text{rep}} = 80$ MHz of the laser and the large pump fluence might lead to a permanent increase of the sample temperature with respect to the temperature without excitation. The good quantitative agreement also reveals that such a pump-induced DC heating is negligible.

Finally, also the magnetic damping is compared with results obtained from the local FMR technique. For this, one has to calculate the dimensionless effective damping parameter α_{eff} , which contains both intrinsic and extrinsic contributions (see Section 5.5). Using the linearized LLG-equation and an oscillator ansatz of the form $m_z =$

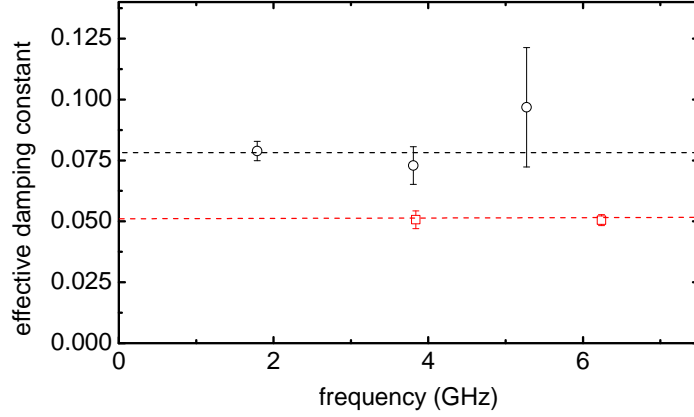


Figure 5.15: Effective damping parameter α_{eff} at $T \approx 7$ K obtained by time-resolved measurements (circles) and local FMR (squares). The dotted lines are just guides to the eye. The large error bars in the time-resolved measurements mainly arise due to the decreasing precession amplitudes with increasing frequency (see Fig. 5.14(d))

$m_z^0 \exp(iAt)$, the following relation between the decay time τ and α_{eff} is found [20]:

$$\alpha_{\text{eff}} = \frac{2}{\tau\gamma\mu_0(\mathfrak{B}_{\text{eff}} + \mathfrak{H}_{\text{eff}})}. \quad (5.7)$$

$\mathfrak{B}_{\text{eff}}$ and $\mathfrak{H}_{\text{eff}}$ are defined in Eq. 2.19 and are determined by the external DC field and the anisotropy constants. Since the in-plane anisotropies are much smaller than the perpendicular magnetic anisotropy, one can use the following approximation:

$$\alpha_{\text{eff}} \approx \frac{2}{\tau\gamma\mu_0(2H_0 + M_{\text{eff}})}. \quad (5.8)$$

As an example, for a magnetic field $\mu_0 H_0 = 55$ mT, $\tau = (0.47 \pm 0.04)$ ns is found, which using Eq. 5.8 and the experimentally determined M_{eff} (Section 5.3) leads to $\alpha_{\text{eff}} = 0.073 \pm 0.06$. This damping constant can be compared quantitatively to local FMR measurements in the frequency domain, which were carried out on the same (Ga,Mn)As sample C. For this, the linewidth of the FMR technique ΔH has to be converted into the effective damping constant using the following relation:

$$\alpha_{\text{eff}} = \frac{\mu_0\gamma}{2\pi} \frac{\Delta H}{f}, \quad (5.9)$$

The resulting damping constants are plotted in Fig. 5.15. The 50% higher damping in the all-optical measurements can be mainly attributed to a inhomogeneous distribution of the effective field within the pump spot diameter. The pump beam has a gaussian intensity profile, the fluence is maximum in the center and decays towards the exterior of the spot. Since both probe and pump beam have the same diameter of $\approx 2.5 \mu\text{m}$, gradients of the temperature within the probed sample area lead to non-uniform magnetic anisotropies. This inhomogeneous anisotropy fields cause a dephasing of the individual spins within the probe spot diameter, which is reflected by a larger effective damping

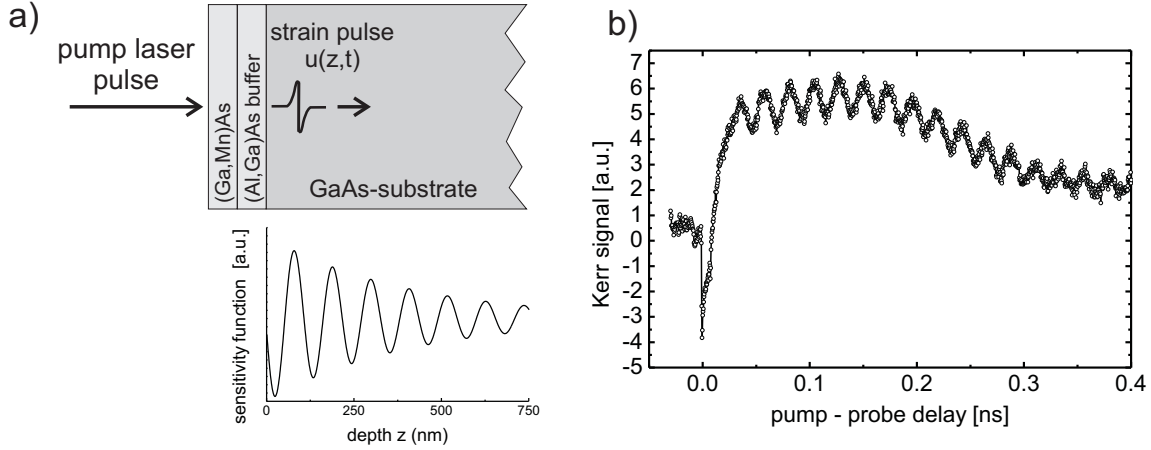


Figure 5.16: (a) Sketch illustrating the excitation of a strain pulse $u(z,t)$ propagating from the (Ga,Mn)As film into the GaAs substrate. (b) Temporal evolution of the Kerr signal for a fluence $F \approx 5 \frac{\text{mJ}}{\text{cm}^2}$ at $T = 6$ K. A magnetic bias field $\mu_0 H_0 = 15$ mT was applied along the [100] direction.

constant. In addition, also spin waves, which move out of the illuminated area might result in an enhanced damping constant.

In summary, the good agreement with Kerr-FMR shows that all-optical measurements are a useful technique to study the magnetization dynamics in (Ga,Mn)As directly in the time domain. However, the error bars in Figs. 5.14 and 5.15 clearly demonstrate, that local FMR is the superior technique for the experimental determination of the anisotropy and damping parameters.

5.6.2 Acoustic strain waves

At high pump fluences ($> 5 \text{mJ/cm}^2$), a very interesting feature is observed in the pump-probe experiments (Fig. 5.16(b)). A fast oscillatory signal with a frequency of ≈ 50 GHz, which is only weakly damped and lasts for several hundreds of picoseconds, is observed in the Kerr signal. Further measurements (data not shown) have demonstrated that the frequency of this fast oscillation is independent of magnetic field amplitude, direction or temperature and even does not vanish above the Curie temperature. This confirms, that the oscillation is not related to the ferromagnetic order in (Ga,Mn)As. On the other hand, it was found, that the frequency of the slower oscillation ($f \approx 2$ GHz) depends on the external field magnitude and can thus be attributed to the precession of the magnetization. In addition, the very fast drop of the Kerr signal at $t = 0$ ps, with a fall time of less than one picosecond, can be attributed to a pump-induced change of the complex refractive index.

In the following, it will be demonstrated that the fast oscillation can be ascribed to an acoustic strain wave, which is generated in the (Ga,Mn)As film and propagates perpendicular to the film plane into the GaAs substrate. In Fig. 5.16(a), an excitation and detection scenario for a strain pulse is illustrated, which was initially proposed by Thomsen et al. [95]: The intense pump pulse is partially absorbed in the (Ga,Mn)As film and leads to a fast instantaneous temperature rise. The rapid heating leads to a thermal

expansion of the lattice and thus to a strain pulse $u(z, t)$, which propagates normal to the surface into the GaAs substrate. No literature value for the acoustic impedance of (Ga,Mn)As is available, nevertheless the acoustic impedances of (Ga,Mn)As film, AlGaAs-buffer layer and GaAs substrate are expected to be very similar, therefore the strain wave should be transmitted into the GaAs substrate without significant reflection. Inside of the GaAs substrate the strain wave propagates with the longitudinal sound velocity of GaAs[100]. Both a change of the reflectivity and of the polarization of the probe beam occur since the strain pulse changes the optical constants of the material. Thomsen et al. [95] gave also a very comprehensive mathematical treatment of these processes. In order to determine the temporal shape of the oscillations in the Kerr signal, one has to calculate the convolution of the sensitivity function $f(z)$ with the time and position dependent strain function $u(z, t)$. The sensitivity function describes how a strain pulse at a certain position z of the film contributes to the overall signal. $f(z)$ can be calculated by solving Maxwell's equations with position dependent refractive indices. As illustrated in Fig. 5.16(a), $f(z)$ is given by an exponentially damped sine function, where the periodicity is given by the half of the wavelength in the material: $k = \frac{\lambda}{2n} = 110$ nm. $\lambda = 808$ nm is the wavelength in vacuum and $n = 3.65$ [96] is the refractive index of GaAs. The sensitivity function drops to $1/e$ on a length scale which is determined by the absorption coefficient α . For GaAs at low temperatures, the penetration depth ($1/\alpha$) at this photon energy is in the micrometer range [97].

The resulting time dependence of the signal obtained by the convolution of strain and sensitivity function is thus given by:

$$K(t) = \int_0^\infty f(z) \cdot u(z, t) dz \propto \sin\left(\frac{4\pi v_l n}{\lambda} t\right) e^{(-t/\tau)}. \quad (5.10)$$

The oscillation period T is given by $T = \frac{\lambda}{2v_l n}$, and the decay time is determined by $\tau = 1/(2\alpha v_l)$. A fit to the experimental data yields $T = (22.9 \pm 0.3)$ ps and $\tau = (0.6 \pm 0.3)$ ns. The experimental sound velocity is then given by $v_l = \frac{\lambda}{2nT} = (4.83 \pm 0.07) \cdot 10^5 \frac{\text{cm}}{\text{s}}$, which is in excellent agreement with the literature value for the sound velocity in GaAs[001] [98]: $v_l = 4.77 \cdot 10^5 \frac{\text{cm}}{\text{s}}$. The absorption coefficient in GaAs can also be calculated by means of the decay time: $\alpha = 1/(2\tau v_l) = (1.7 \pm 0.6) \cdot 10^3 \text{cm}^{-1}$, which does not agree very well with a literature value of GaAs ($T = 20$ K, $\lambda = 808$ nm): $\alpha = 9 \cdot 10^3 \text{cm}^{-1}$ [97]. Since the probe photon energy $E_{ph} = 1.54$ eV is slightly larger than the band gap of GaAs at $T = 10$ K: $E_g = 1.52$ eV, the discrepancy may be explained by the sensitivity of the absorption coefficient close to the energy gap of GaAs.

5.6.3 Transient changes of the magnetic anisotropies

After having demonstrated the reliability of both all-optical pump-probe technique (Section 5.6.1) and local Kerr-FMR (Section 5.1), both measurement techniques are combined. By measuring the angular dependence of the resonance fields $H_R(\varphi_H)$ as a function of the pump-probe delay, information about the time dependence of the magnetic anisotropies can be obtained. If there was a transient influence of the pump pulse on

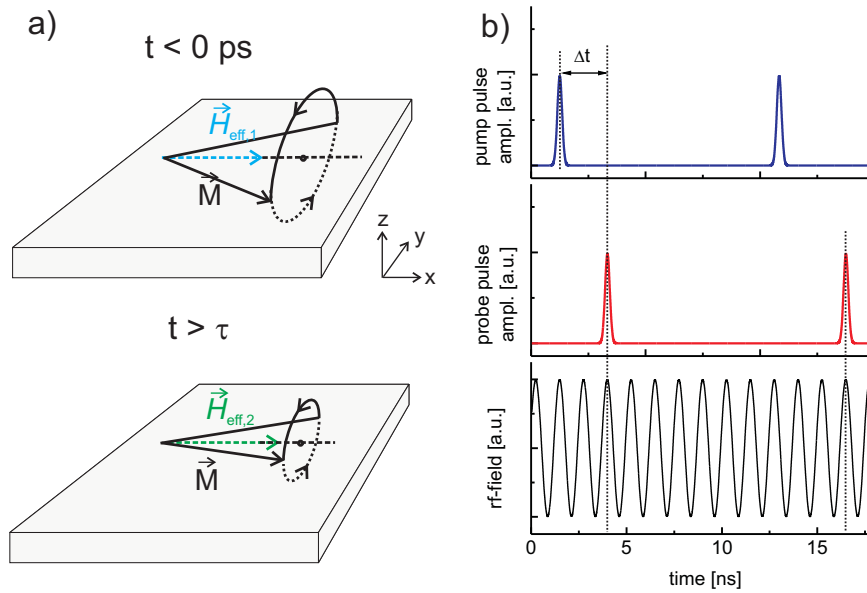


Figure 5.17: (a) Illustration of the effects of photoexcited holes on the precessing magnetization for the case that the external field matches the resonance field before the excitation ($t < 0$ ps). (b) Illustration of the synchronization between pump pulses, probe pulses and the microwave excitation. The phase of the sinusoidal microwave excitation is synchronized with the probe laser pulses. For this the frequency of the microwave field has to be an integer multiple of the laser repetition rate of 80 MHz. This phase is maintained constant during the measurement. The pump pulses are delayed with respect to the probe pulses by means of a mechanical delay. This approach allows one to measure the resonance fields as a function of the pump-probe delay $H_R(t)$.

the magnetization and the magnetic anisotropies as reported in [12, 13], the resonance fields should shift after the excitation with the pump pulse.

In practice, the experiment is performed as follows: In a first step, the spatial and temporal overlap of pump and probe beams is ensured by performing all-optical pump-probe measurements in the time domain (detailed description in sections 4.5 and 5.6.1). In the next step, the pump beam modulation (chopping of pump beam) is switched off and the microwave excitation is turned on. Analog to the description of the local FMR technique in Section 4.4, the microwave frequency is kept constant and the resonance spectra are measured by sweeping the external magnetic field. During the measurements, the phase between microwave excitation and probe pulses is held constant. The delay between pump and probe pulses is varied by means of an additional optical delay. This temporal synchronization of pump and probe pulses and microwave phase is depicted in Fig. 5.17(b). Representative examples of FMR spectra measured without pump beam, before and after arrival of the pump pulse are shown in Fig. 5.18. The exact overlap of the spectra with and without excitation demonstrates, that the additional pump beam does not lead to a permanent heating of the sample. In addition, the resonance field does not even change after the excitation with the pump pulse ($\Delta t = +250$ ps), which indicates that the effective magnetic field remains unchanged. Additional, systematic measurements at various delay times, pump intensities, bias field angles and temperatures were performed (data not shown). Within the experimental error bars (± 1 mT),

none of the results showed a time dependence of the resonance fields $H_R(t)$. It is crucial to consider, whether the pump-induced change in the hole concentration Δp can lead to measurable changes of the resonance fields ΔH_R : The density of photons per pulse and area is given by: $N_A = F/E_{\text{pump}} \approx 10^{16} \text{cm}^{-2}$, where $F \approx 5 \frac{\text{mJ}}{\text{cm}^2}$ is the fluence and $E_{\text{pump}} = 3.1 \text{ eV}$ is the energy of the pump pulses. From theory [37], a minimum value of the light absorption coefficient $\alpha = 1 \cdot 10^4 \text{cm}^{-1}$ can be estimated. Thus, at least 5% of the photons are absorbed in the 50 nm thick (Ga,Mn)As film. The resulting density of additional holes is then given by: $\Delta p = 0.05 \cdot N_A/t = 1 \cdot 10^{20} \text{cm}^{-3}$, which corresponds to $\approx 25\%$ of the equilibrium hole concentration p . Both in theory and experimentally [7, 8, 37, 38, 63], it was demonstrated, that the magnetization and the magnetic anisotropies depend on the hole concentration. While the same dependence was found for the magnetization and the strain-induced perpendicular anisotropy, the behavior of the in-plane anisotropies is not consistent among the different reports [7, 38]. However, since the in-plane anisotropies $K_{C\parallel}$ and $K_{U\parallel}$ in the present sample are more than one order of magnitude smaller than the perpendicular anisotropy $K_{U\perp}$, the hole-induced change of the in-plane anisotropies (and thus the change of the resonance fields) can be neglected in the following estimation. Experimentally [7, 38] and theoretically [37], it was found, that the perpendicular uniaxial anisotropy $K_{U\perp}$ increases with increasing hole concentration. For $\Delta p/p = 25\%$, one can estimate a lower boundary of $\Delta K_{U\perp}/K_{U\perp}$ of 15%. In the mean-field model, the magnetization increases with increasing hole concentration with $p^{1/3}$. A change of $\Delta M/M = 3\%$ (using the exp. data of Ref. [38]) can be estimated. Using these ratios $\Delta M/M$, $\Delta K_{U\perp}/K_{U\perp}$ and the magnetic parameters which were determined in Section 5.3, the photoinduced holes would lead to a downshift of the resonance fields of at least $\mu_0 \Delta H_R = -5 \text{ mT}$, which is significantly larger than the accuracy of the experimental resonance fields of $\approx 1 \text{ mT}$. Finally, one has to consider, that two sets of different parameters ($M, K_{U\perp}, K_{C\parallel}, K_{U\parallel}$) could lead to the same resonance field, since the dependence of the in-plane anisotropies on the hole concentration can be complicated. However, even this scenario can be ruled out, because the resonance fields remained unchanged when the external field was applied along the [110] or [1-10]-direction. These pessimistic approximations demonstrate, that pump-induced changes of the anisotropies should have been observed in this type of experiment.

In order to understand these experimental results it is necessary to return to the lifetime of the photoexcited holes and to consider how the transient hole-induced changes of the anisotropies affect the measured resonance fields $H_R(t)$ in this experiment with continuous microwave excitation. The orientation of the effective field \vec{H}_{eff} should be almost unaffected by the pump excitation in the present experiment because the external magnetic field is much stronger than the magnetic in-plane anisotropies. However, the change of the magnitude of the effective field should lead to a shift of the resonance field after the excitation. This situation is illustrated in Fig. 5.17(a): Under the assumption that the external field matches the resonance field before the arrival of the pump pulse, i.e. $H_0 = H_R$, the amplitude of the precession has a maximum for $t < 0 \text{ ps}$. After the excitation ($t > 0 \text{ ps}$) the pump-induced changes of the magnetic anisotropy modify the resonance condition; $H_0 = H_R$ is not fulfilled any more. Therefore, the precession amplitude

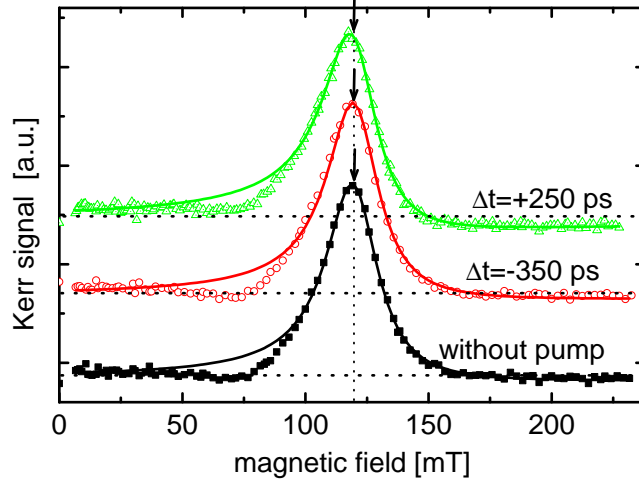


Figure 5.18: FMR spectra of sample C, for $f = 5.5$ GHz and $T = 40$ K without pump pulse, before ($\Delta t = -350$ ps) and after the arrival of the pump pulse ($\Delta t = +250$ ps). The experimental data are given by the symbols, and are vertically offset for clarity. The solid lines are the Lorentzian fits to the experimental data, the fitted resonance fields are shown by the arrows. Due to small drifts of the microwave phase, the spectra are slightly asymmetric. Therefore, the resonance fields do not exactly agree with the maxima in the spectra.

is significantly decreased. This drop of the amplitude does not occur instantaneously, but is mainly governed by the relaxation time τ . For $\mu_0 H_0 = 102$ mT, a relaxation time $\tau \approx 280$ ps was found experimentally in the previous section. So, if the lifetime of the holes was in the range of several hundreds of picoseconds, this temporary change of the resonance condition should have led to significant changes of the measured resonance fields $H_R(t)$. In order to determine the effects of shorter changes of the magnetic anisotropy quantitatively, a macrospin simulation with continuous microwave-excitation was performed. The temporal evolution of the resonance field $H_R(t)$ was simulated using the experimentally found magnetic parameters and assuming a rectangular time dependence of the perpendicular anisotropy: $K_{U\perp} = -3 \times 10^3 \frac{\text{J}}{\text{m}^3}$ for $t < 0$ ps and $t > 100$ ps; and $K_{U\perp} = -3.45 \times 10^3 \frac{\text{J}}{\text{m}^3}$ for $0 \text{ ps} < t < 100 \text{ ps}$. It was found that this anisotropy change with a duration of only 100 ps would lead to significant (measurable) changes of the resonance fields $H_R(t)$ up to 500 ps after the excitation. This also demonstrates, that the lifetime of the holes must be much lower than 100 ps and is not in the range of several hundreds of picoseconds, as reported by Wang et al. [13] and Hashimoto et al. [12]. It is also hard to imagine, why the much lower pump fluences (three orders of magnitude) and the resulting very small changes of the hole concentration $\Delta p/p < 0.1\%$ ¹ in these earlier experiments [12, 13] should have led to measurable changes of the anisotropies or the magnetization.

In summary, in the present combined pump-probe and FMR experiments no transient

¹In Ref. [13], $\Delta p/p = 2\%$ was reported, which is not correct. Even under the unrealistic assumption, that every photon is absorbed in the (Ga,Mn)As film and leads to an additional hole, only $\Delta p/p \approx 1\%$ can be estimated.

changes of the magnetic anisotropy on a subnanosecond time scale were observed, indicating that the lifetime of the photo-excited holes is less than ≈ 50 ps. In future experiments, as-grown $\text{Ga}_{1-x}\text{Mn}_x\text{As}$ samples with lower Mn-concentration x should be investigated. In these films the equilibrium hole concentration is much lower, therefore photoexcited holes should lead to larger transient changes of the magnetic properties and resonance fields. Further systematic studies, using also different pump beam energies, should allow one to understand the role of the transient carriers on the ferromagnetic properties in (Ga,Mn)As.

6 Magnetic anisotropy and coercive fields of (Ga,Mn)As nanostructures

Diluted magnetic semiconductors, such as (Ga,Mn)As, are considered as promising candidates for the application in spintronics devices. In order to understand and engineer the magneto-transport properties of such structures it is of utmost importance to understand and control the magnetic anisotropies and the switching behavior. The results from the previous chapter and earlier experimental results have demonstrated that the magnetic anisotropies in (Ga,Mn)As films depend crucially on various parameters such as temperature [30, 33, 47, 65], hole and Mn-concentration [38, 39] and post-growth annealing [67]. Also a strong dependence of the anisotropies on the biaxial strain in the film plane was observed [32]. Because many of these parameters depend sensitively on the growth and annealing conditions, it is very difficult to adjust or even reproduce the magnetic anisotropies in (Ga,Mn)As films.

Yet, recent experiments have shown that the magnetic anisotropies can be manipulated by releasing the compressive lattice strain in micron-sized (Ga,Mn)As elements [9–11]. Unfortunately, these experiments did not resolve magnetic anisotropies in (Ga,Mn)As micro- and nanostructures locally; the signal in magneto-resistance or SQUID measurements is always proportional to the average magnetization of the structures. In this chapter the local ferromagnetic resonance technique is employed which provides a direct access to the energy landscape and to the magnetic anisotropies of confined structures. By patterning a (Ga,Mn)As film the compressive biaxial strain in the film plane can be partially released, strongly affecting the magnetic anisotropies. In sections 6.1 and 6.2 circular and rectangular-shaped structures are studied experimentally, in order to analyze these strain relaxation effects in detail. In Section 6.3 the consequences of this local strain relaxation are visualized with the scanning Kerr microscopy technique. The results indicate that the magnetic anisotropies in small (Ga,Mn)As elements change locally. In Section 6.4 the influence of these strain induced anisotropies on the static properties such as ground state and switching process will be demonstrated. Moreover, the influence of the induced anisotropy on the coercive fields will be discussed. Micromagnetic simulations are performed in order to backup the experimental findings and to reveal details about the switching process which are not accessible experimentally. Up to the present day the origin of the uniaxial in-plane anisotropy in unpatterned (Ga,Mn)As films is controversially discussed. It was proposed that this anisotropy is caused by a uniaxial strain in the film plane, which breaks the tetragonal crystal symmetry [40, 47]. In Section 6.5, the magnetic anisotropies of lithographically defined elements and an unpatterned film are compared in order to follow up on this question.

6.1 Magnetic anisotropies of rectangular (Ga,Mn)As elements

A magnetic memory element requires at least two stable magnetic ground states, which represent the binary numbers '0' and '1'. In conventional ferromagnetic materials, such as iron, this can be easily achieved by means of the shape anisotropy in small rectangular or elliptically shaped structures. However, since the magnetization in (Ga,Mn)As is typically two orders of magnitude smaller than in conventional ferromagnetic materials, the shape anisotropy is much smaller than the intrinsic magneto-crystalline anisotropies, which prevents the formation of two reliable magnetization states in (Ga,Mn)As structures. Nevertheless, earlier reports [10, 11] and the experimental results presented in this thesis show that narrow (Ga,Mn)As elements exhibit a strong uniaxial anisotropy in the film plane which is induced by strain relaxation effects. This anisotropy can play the role of the shape anisotropy of conventional ferromagnetic materials. The structural properties of such nanostructured elements will be addressed in the subsequent section. The dependence of the induced anisotropy on the stripe width and orientation will be discussed in Section 6.1.2.

6.1.1 Structural properties

The lattice mismatch between the GaAs substrate and the (Ga,Mn)As film leads to a compressive biaxial strain ε_{xx} in the film plane which induces a pronounced uniaxial anisotropy perpendicular to the film plane (see the discussion in Section 3.1). X-ray diffraction measurements have demonstrated, that this strain is sustained up to high (Ga,Mn)As film thicknesses of several micrometers [33]. In lithographically defined elements this strain can be partially relaxed, which obviously has also significant effects on the magnetic anisotropies. Actually, these relaxation effects were verified experimentally in an array of 200 nm wide bars by means of grazing incidence x-ray diffraction (GIXRD) measurements [10]. It was found that the (Ga,Mn)As lattice partially relaxes along the short side of the bars whereas along the bar the strain is comparable to the compressively strained (Ga,Mn)As film. A sketch of these relaxation effects is given in Fig. 6.1(c). Qualitatively, these relaxation effects can be understood easily: In a (Ga,Mn)As film the atoms in the film plane are forced into their compressively strained position, because they are locked to the underlying GaAs substrate with the lower lattice constant a_0 . In a (Ga,Mn)As stripe, the atoms at the edges of the stripe are free to relax into an unstrained lattice position because no neighboring atoms hinder this relaxation. In contrast, parallel to the stripe, the atoms are surrounded by other atoms and the atoms remain in their compressively strained positions. Quantitatively, these effects were modeled in finite-element simulations where the resulting strain and lattice displacements are obtained by minimizing the strain energy [10, 11, 40]. It was found that only in narrow stripes (few hundred nanometer) the strain relaxation is relatively homogenous across the stripe width, whereas for wider stripes ($\approx 1\mu\text{m}$), the strain relaxation is concentrated mainly at the edges, and decays towards the center of the element. In the

center of the wider elements only a small degree of lattice relaxation $\approx 10\%$ is obtained. As illustrated in Fig. 6.1(c), also the etching depth t_{etch} plays an important role: When the etching extends well into the GaAs substrate a larger degree of strain relaxation is obtained than for lower etch depths. Recently, Zemen et al. [40] have simulated the relaxation profiles also for different ratios of stripe thickness t to width w . The strain relaxation averaged over the cross section of the stripe is quantified by the parameter $\bar{\rho}$, where $\bar{\rho} = 1$ corresponds to the complete relaxation of the (Ga,Mn)As lattice perpendicular to the stripe axis. It was found that $\bar{\rho}$ increases monotonically with increasing t/w . However, $\bar{\rho}$ approaches only one for $t/w \approx 1$. Therefore, only for very narrow stripes the (Ga,Mn)As lattice is fully relaxed perpendicular to the stripe axis.

6.1.2 Quantitative determination of the anisotropies

A systematic FMR study of rectangular elements was performed in order to determine the consequences of the strain relaxation effects on the magnetic anisotropies. In contrast to the earlier SQUID and magneto-transport measurements [9–11], the employed Kerr-FMR technique allows a quantitative determination of the anisotropies. In order to avoid ambiguities, in the following sections the magnetic anisotropies of the unpatterned film are referred to as intrinsic (upper index 'i'), while the anisotropies of the lithographically defined elements are referred to as patterning-induced (upper index 'p').

The nanostructures were prepared on a piece of the (Ga,Mn)As wafer C, whose structural and magnetic properties were already covered in Section 5.3. In a first step e-beam lithography and ion beam etching were used in order to fabricate the magnetic nanostructures. The total etch depth t_{etch} is approximately 80 nm, due to the (Ga,Mn)As film thickness $t = 50$ nm, the etching extends approximately 30 nm into the GaAs substrate, compare Fig. 6.1(c). Stripes having a width ranging from 200 nm up to 4 μm patterned along different crystallographic directions ([100], [110], [010]) were prepared. For the excitation of the magnetization with microwaves in the GHz-range a coplanar waveguide (CPW) with a bandwidth of 10 GHz was defined in a subsequent lithography step. The magnetic elements are placed in the gap between the 30 μm wide center conductor and the ground plane resulting in a mainly out-of-plane rf-excitation. More details concerning the sample preparation and the waveguide characterization are given in Appendices 8.2 and 8.3. A micrograph of the sample is shown in Fig. 8.1.

First of all, the magnetic anisotropies of a 400 nm wide stripe oriented along the [110] direction are compared to the (Ga,Mn)As film. The measurements were performed with a laser spot diameter of ≈ 500 nm at the center of the (Ga,Mn)As elements. The angular dependence of the resonance fields of a $60 \times 60 \mu\text{m}^2$ (Ga,Mn)As mesa, used as reference structure and mimics the response of an isotropically strained unpatterned film is shown in Fig. 6.1(a). The angular dependence of the resonance fields $H_R(\varphi_H)$ is dominated by the intrinsic cubic anisotropy $K_{C\parallel}^i$ and has also a small contribution due to the uniaxial in-plane anisotropy $K_{U\parallel}^i$ (compare Section 5.3). The fourfold symmetry changes drastically into a strongly pronounced twofold symmetry when the (Ga,Mn)As film is patterned into a narrow stripe (Fig. 6.1(b)). The minimum of the resonance fields in

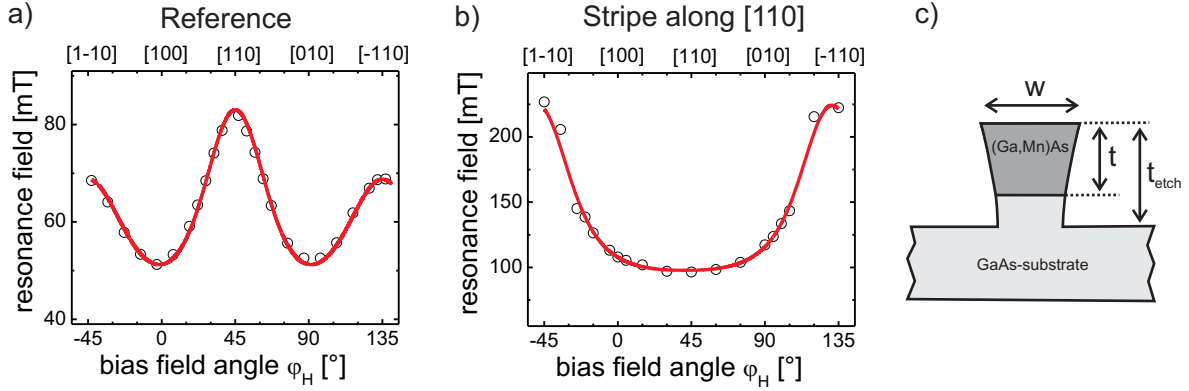


Figure 6.1: Resonance field as a function of the external field angle φ_H for the (Ga,Mn)As reference structure at $f = 3.84$ GHz (a) and for a 400 nm wide stripe patterned along [100] for $f = 7.2$ GHz (b). The measurements were performed at $T = 7$ K. The solid lines are the theoretical fits which are used to extract the anisotropy constants. (c) Schematic illustration of the cross section of a (Ga,Mn)As stripe on a GaAs(001) substrate. The magnitude of the lattice relaxation across the stripe is strongly exaggerated, the lattice expansion across the stripe is smaller than 0.2%.

Fig. 6.1(b) is found along the stripe axis ($H \parallel [110]$). This result clearly demonstrates that the patterning leads to an additional uniaxial anisotropy $K_{U\parallel}^P$ with an easy axis perpendicular to the strain relaxation direction.

These results are also in qualitative agreement with earlier theoretical calculations using a six band $\vec{k}\vec{p}$ description of the GaAs host valence band in combination with a kinetic exchange model for the coupling to local Mn moments where these anisotropic strain effects are included [10, 11, 40, 99]. Surprisingly, already small relaxation effects of several hundredths of a percent ($\varepsilon_{xy} = 0.01 - 0.05\%$) induce a pronounced uniaxial anisotropy which exceeds the values of the intrinsic in-plane anisotropies.

In order to analyze the influence of the strain relaxation on the anisotropies in more detail, stripes with different width and orientation were investigated. In Fig. 6.2(a) the results for three different orientations of the stripes ([100],[010],[110]) are shown. One can clearly observe that the minimum of $H_R(\varphi_H)$ and thus the easy axis of the induced anisotropy coincides with the long axis of the stripe. This behavior is also in agreement with earlier studies using SQUID and magnetotransport measurements [9–11]. The magnitude of the strain-relaxation induced anisotropy $K_{U\parallel}^P$ can be estimated by simply adding an additional patterning-induced uniaxial anisotropy term $E_{U\parallel}^P = K_{U\parallel}^P \sin^2(\varphi - \varphi_U)$ to the free energy density. φ_U denotes the angle of the easy axis of this additional anisotropy with respect to the [100]-direction. By fitting the experimental data for the patterned stripes using the procedure described in Section 5.3, one finds $K_{U\parallel}^P = 1.8 \times 10^3 \frac{\text{J}}{\text{m}^3}$ for the 400 nm wide stripe which is one order of magnitude larger than the intrinsic cubic anisotropy constant of the (Ga,Mn)As film. A rough approximation using the demagnetization factors from Ref. [15] immediately shows that the shape anisotropy $K_S = 3.9 \times 10^1 \frac{\text{J}}{\text{m}^3}$ is almost two orders of magnitude too small to explain this strong uniaxial anisotropy.

The lattice relaxation in broader stripes is spatially non-uniform and takes place on a

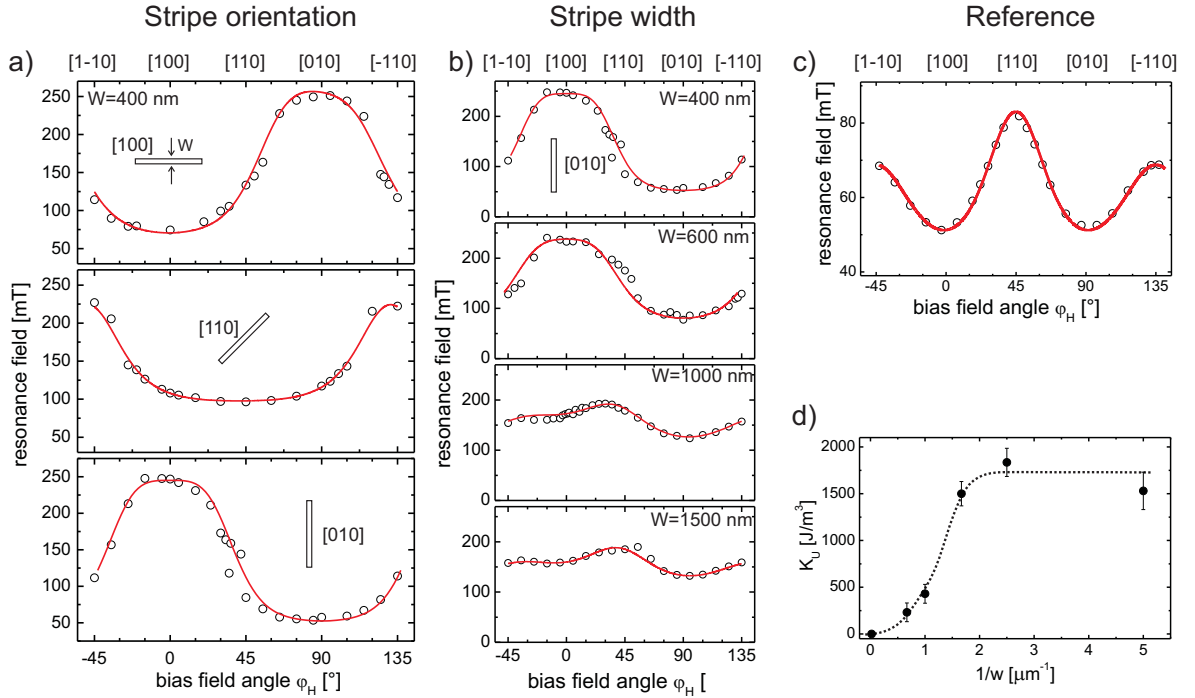


Figure 6.2: Resonance field as a function of the external field angle φ_H for the stripes patterned along different crystallographic axes (a) and different stripe width w (b). All the data on the stripes was obtained at $f = 7.2$ GHz and $T = 7$ K. The solid lines are fits to the experimental data. (c) For comparison the resonance fields of the reference structure (for $f = 3.84$ GHz) are also plotted. (d) Induced uniaxial anisotropy versus reciprocal stripe width $1/w$. The dotted line is just a guide to the eye.

length scale of several hundred nanometers. Therefore it is not surprising to find a very pronounced uniaxial behavior for small stripe widths (400 nm and 600 nm) while for larger widths a mixture of twofold and fourfold symmetry is observed, see Fig. 6.2(b). This behavior can be attributed to the inhomogeneous nature of the lattice relaxation across the stripe width. The data of the wider stripes (1000 nm and 1500 nm) can be well interpreted as a superposition of fourfold and strain relaxation-induced twofold symmetry. In broader stripes the strain relaxation is mostly concentrated at the edges and only a small degree of lattice relaxation is found in the center of the stripe. Because the laser beam probes mainly the central region of the stripes (≈ 500 nm), a smaller patterning-induced anisotropy is observed for the broader stripes. The experimentally determined patterning-induced anisotropy as a function of the reciprocal stripe width is shown in Fig. 6.2(d). As expected, for large stripe widths the induced anisotropy approaches zero because the strain relaxation effects become negligible. For small stripe widths the induced anisotropy saturates, probably due to complete strain relaxation across the stripe width. These results also demonstrate that the magnitude of the induced uniaxial anisotropy can be well adjusted for stripe widths ranging between 500 nm and 1500 nm.

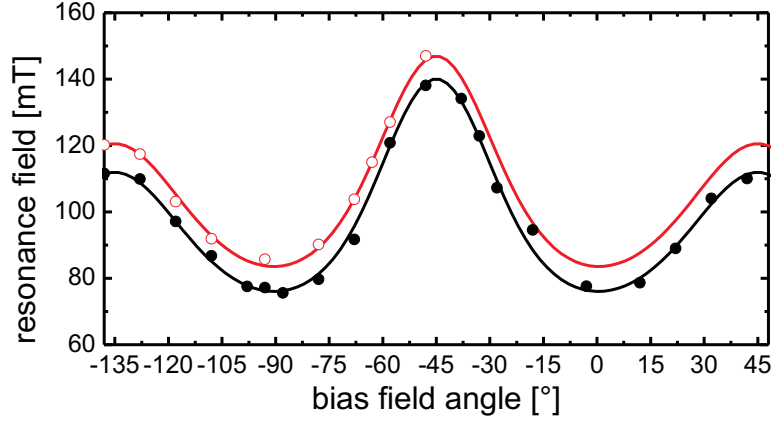


Figure 6.3: Angular dependence of the resonance field for disk-shaped (Ga,Mn)As elements for $f = 5.84$ GHz and $T = 7$ K. The full black and the open red dots represent the experimental data for a disk with a diameter $d = 10 \mu\text{m}$ and $d = 1.5 \mu\text{m}$, respectively. The solid lines are obtained by fitting the experimental data. The (Ga,Mn)As disks were prepared on a piece of the (Ga,Mn)As film B, which was discussed in Section 5.3.

6.2 Magnetic anisotropies of circular (Ga,Mn)As elements

The investigation of a different sample geometry is used to shed light on the role of the strain relaxation direction on the magnetic anisotropies. The angular dependence of the resonance fields for a disk with a large diameter ($d = 10 \mu\text{m}$, black symbols) and a small diameter ($d = 1.5 \mu\text{m}$, red symbols) is shown in Fig. 6.3. The experimental data for the $10 \mu\text{m}$ -diameter disk were obtained at the disk center where the strain relaxation effects are negligible. It has to be emphasized that in contrast to a narrow rectangular structure where the strain can only relax along one direction (Fig. 6.2(a)), isotropic strain relaxation is expected for a disk-shaped element. For this reason the in-plane anisotropies $K_{U\parallel}$ and $K_{C\parallel}$ should remain constant while the strain-induced perpendicular anisotropy $K_{U\perp}$ should be reduced. This reduction is indeed observed (Fig. 6.3) as the resonance fields are only shifted to higher field values. The fits to the experimental data show that $K_{U\parallel}$ and $K_{C\parallel}$ remain almost constant while $K_{U\perp}$ is reduced by approximately 15% for the disk with $1.5 \mu\text{m}$ diameter, compare table 6.1. These experiments in circular elements further support the explanation of the induced uniaxial anisotropy in elements with anisotropic strain relaxation. Because of the relation $K_{U\perp} \sim \varepsilon_{xx}$, the reduction of $K_{U\perp}$ can be ascribed to an average reduction of the biaxial strain of 15% in the $1.5 \mu\text{m}$ diameter disk.

diameter [μm]	$K_{U\perp}$ [$10^2 \frac{\text{J}}{\text{m}^3}$]	$K_{U\parallel}$ [$10^2 \frac{\text{J}}{\text{m}^3}$]	$K_{C\parallel}$ [$10^2 \frac{\text{J}}{\text{m}^3}$]
10	-40 ± 1	-2.0 ± 0.3	3.7 ± 0.3
1.5	-34 ± 2	-1.9 ± 0.6	3.8 ± 0.6

Table 6.1: Anisotropy constants of the disk-shaped elements at $T = 7$ K.

6.3 Visualization of local variations of the magnetic anisotropy

In the previous sections, smaller elements close to the spatial resolution of ≈ 500 nm were investigated. It was found, that strain relaxation effects and local changes of the anisotropies take place up to a length of approximately $1 - 2 \mu\text{m}$. In this section larger micron-sized structures are studied, whose inhomogeneous magnetic response can be visualized with the scanning Kerr microscopy technique. In Fig. 6.4 spatially resolved images of the polar Kerr signal obtained at a fixed excitation frequency f and applied field H_0 for both rectangular and disk-shaped structures are shown.

In circular and rectangular geometries one finds laterally isotropic and anisotropic strain relaxation, respectively (indicated by the blue thick arrows in Figs. 6.4a and 6.4d). Furthermore for larger structures one can distinguish two regions as illustrated in the figures: (i) the boundary of the structure where the strain relaxation takes place and a strong strain induced magnetic anisotropy can be expected. And (ii) the central region of the structure where the (Ga,Mn)As lattice is fully strained and the magnetic anisotropy is unchanged compared to the extended (Ga,Mn)As film. As a consequence, the magnetic anisotropies and the direction of the easy axes of the magnetization are varying *locally*. Based on previous results the local easy axes (shown by the red thin arrows) are expected to be parallel to the boundary of the elements, whereas in the central region the film-like behavior with easy axes along the $\langle 100 \rangle$ -directions is expected.

Spatially non-uniform magnetic anisotropies lead to a non-uniform magnetic response for uniform excitation. In particular the condition for FMR is only satisfied locally. This behavior is clearly observed in Figs. 6.4b,e,g, where the white contrast represents larger values of the polar Kerr signal. This signal is directly linked to the z -component of the precessing magnetization. For a large rectangular structure ($60 \mu\text{m} \times 14 \mu\text{m}$) which was patterned on the same sample, the Kerr signal shows two stripes parallel to the external field direction for $\mu_0 H_0 = 50$ mT whereas for $\mu_0 H_0 = 110$ mT the magnetic response is almost uniform. The strain relaxation at the boundary induces a uniaxial anisotropy with an easy axis parallel to the stripe. A similar behavior is also found for the circular structure (see Fig. 6.4(e)-(g)). Indeed at the resonance field of the disk center (which for $f = 5.84$ GHz and $\varphi_H = -45^\circ$ is approximately $\mu_0 H_U = 140$ mT, see Fig. 6.3) the magnetic response is uniform (Fig. 6.4(f)). However for $H_0 < H_U$ two ring shaped modes at the disk boundary (Fig. 6.4(e)) and for $H_0 > H_U$ two modes localized at the edges are found (Fig. 6.4(g)). Note that while for $H_0 < H_U$ these ring shaped modes are aligned along the field direction, for $H_0 > H_U$ the modes are aligned perpendicular to H_0 . The ring-shaped modes can be explained in the following way: Due to the lattice relaxation at the disk boundary the easy axis follows the circumference. Based on the results for narrow stripes where the easy axis of the magnetization prefers alignment along the long axis of the stripe, it is expected that the local easy axis is aligned tangential with respect to the boundary of the elements. For the ring shaped areas the external field is aligned along the local easy axes which means that the resonance is observed at a lower bias field than the main resonance. In contrast for the areas located at the bottom

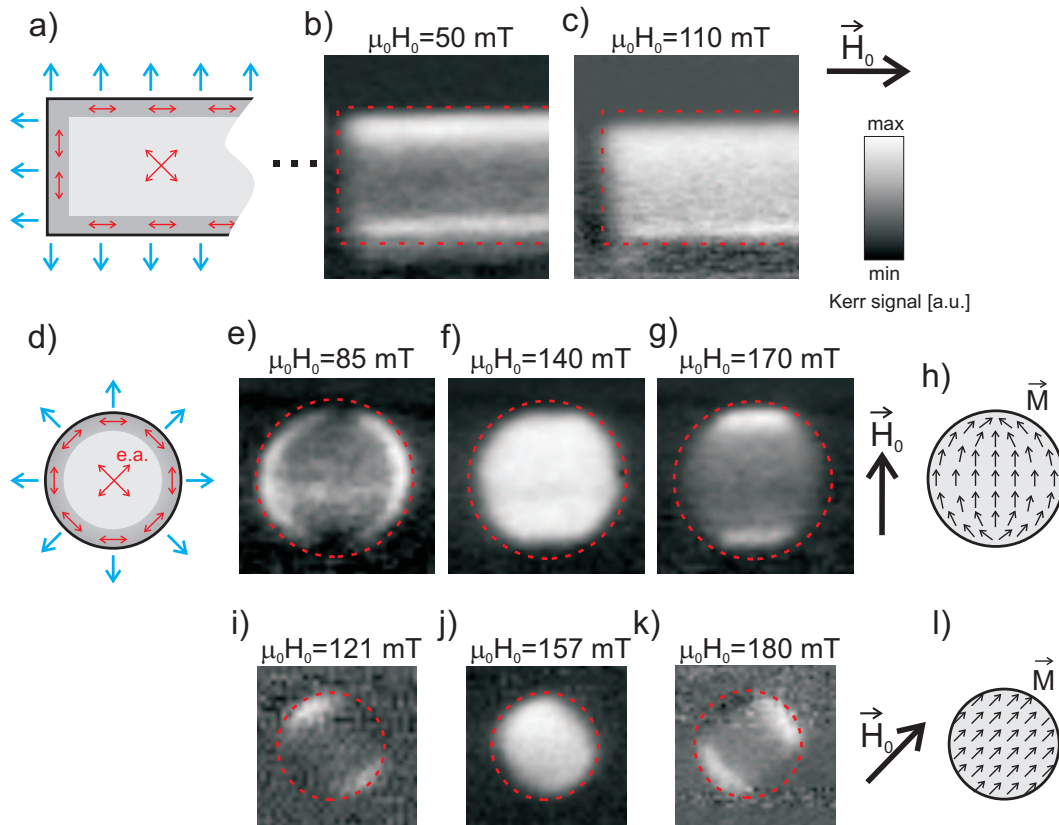


Figure 6.4: Sketch illustrating the strain relaxation direction (blue bold arrows) and the associated distribution of anisotropies with local easy axes (red thin arrows) for a rectangular structure (a) and a circular structure (d). Images of the polar Kerr signal for a large rectangular structure ($60\mu\text{m} \times 14\mu\text{m}$) for $f = 4.6$ GHz (upper row) and for two circular structures with a diameter of $10\mu\text{m}$ for $f = 5.84$ GHz (middle row) and for a diameter of $7\mu\text{m}$ for $f = 8.96$ GHz (lower row). The magnetic field direction for each element is indicated by the arrow. The red dotted lines indicate the outlines of the elements. (h),(l) Sketches of the magnetization configurations for images (e) and (i), respectively.

and top of the image the bias field is aligned along a local hard axis, which results in a larger resonance field. These findings are consistent with other measurements where the external field was applied along other directions. An example is given for $\varphi_H = -90^\circ$ for a $7\ \mu\text{m}$ diameter disk in Fig. 6.4(i)-(k) where the contrast is rotated by 45° with respect to Fig. 6.4(e)-(g).

Finally, it is rather striking that one finds a ring or half-moon shaped signal in Fig. 6.4(e), while the signal in Fig. 6.4(g) has a rectangular shape. This behavior can be attributed to a non-uniform magnetization distribution for smaller external fields H_0 . A sketch of the magnetization distribution for $\mu_0 H_0 = 85\ \text{mT}$ is given in Fig. 6.4(h). Because of the much lower values of the intrinsic anisotropies in the central region of the disk (i), the external field H_0 is sufficient to align the magnetization along H_0 . Because of the strong induced anisotropy in the boundary region (ii), the local anisotropy field $\mu_0 H_V^p \approx 100\ \text{mT}$ competes with the external field $\mu_0 H_0 = 85\ \text{mT}$. Therefore, the magnetization bends towards the boundary of the disk, leading to the half moon shaped signal in Fig. 6.4(e). This magnetization configuration shows similarities to a so called 'onion state', which is well known for small rings produced from ferromagnetic metals, such as cobalt [100, 101]. The onion state is characterized by two domains with opposite circulation of the magnetization. It is important to note, that in these materials, this configuration is a consequence of the minimization of the stray field and Zeeman energy, while the magnetization configuration in (Ga,Mn)As can be ascribed to the local minimization of the magneto-crystalline anisotropy and Zeeman energy. In Fig. 6.4(g), the external field $\mu_0 H_0 = 170\ \text{mT}$ is sufficient to nearly align all magnetic moments parallel, leading to the rectangular contrasts in the Kerr images. This line of arguments is also supported by the Kerr images of the smaller disk ($d = 7\ \mu\text{m}$) at a higher frequency $f = 8.96\ \text{GHz}$, where the resonance positions are shifted to higher field values (Fig. 6.4(i),(k)). Both for $\mu_0 H_0 = 121\ \text{mT}$ (below the main resonance) and $\mu_0 H_0 = 180\ \text{mT}$ (above the main resonance), the Kerr signal has a rather rectangular shape. The higher external field values lead to an almost parallel alignment of the magnetic moments, compare Fig. 6.4(l).

6.4 Magnetization reversal in (Ga,Mn)As micro- and nanostructures

Magnetic domains in (Ga,Mn)As films are usually very large (several hundreds of micrometers) [102], therefore one would expect a single domain configuration in micron-sized (Ga,Mn)As elements, where all magnetic moments are aligned parallel. Already the dynamic FMR investigations of micron-sized elements in the previous section have demonstrated that this is not the case. Therefore also the switching processes may not be described by means of coherent rotation of the magnetization in a Stoner-Wohlfahrt model. Recently, static MOKE measurements of very small (Ga,Mn)As disks [103] have confirmed, that only elements with sizes in the range of the exchange length (20 nm-50 nm) behave like single-domain particles. In this section, the experimentally determined coercive fields will be compared to micromagnetic simulations and to the Stoner-

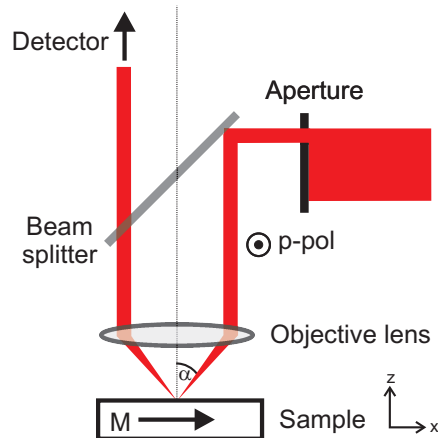


Figure 6.5: Modification of the polar Kerr setup for static longitudinal MOKE measurements. The angle of incidence α is selected by means of an aperture. The external magnetic field is applied along the x-direction (parallel to the plane of incidence).

Wohlfarth model. Especially the influence of the induced anisotropy on the magnetic ground state and the switching will be discussed.

First of all, the experimental technique allowing one to measure the switching of individual (Ga,Mn)As elements in the film plane will be introduced: Because of the polar Kerr geometry in the Kerr-FMR setup (Section 4.4), only magnetization components perpendicular to the film plane are detected. Since the magnetization of all studied films and the external field are aligned in the film plane, the setup has to be modified for the static measurements. As illustrated in Fig. 6.5, an aperture blocks a large part of the incoming laser beam, so that only a small part of the beam impinges the sample under an angle of incidence α . Since the polarization is perpendicular to the plane of incidence, the transversal Kerr effect vanishes and only the longitudinal Kerr effect has to be considered, compare Section 4.1. Therefore, the measured signal represents the projection of the magnetization vector on the x-direction (parallel to the plane of incidence). Instead of the pulsed Ti-Sapphire laser a more stable cw laser diode with a wavelength of 630 nm was used for the static measurements.

Unfortunately, the spatial resolution of approximately 500 nm does not allow one to spatially resolve the actual switching process in the (Ga,Mn)As stripes. However, micromagnetic simulations can help to gain further information which is not accessible in the experiment. All input parameters were determined experimentally by means of SQUID measurements (M_S , A) and local FMR measurements: ($K_{U\perp}$, $K_{C\parallel}$, $K_{U\parallel}^P$), compare Section 5.3. The simulations were performed using the commercially available LLG micromagnetic simulation software [104], on a grid with blocks of $5 \text{ nm} \times 5 \text{ nm} \times 50 \text{ nm}$, i.e. with only one layer along the growth direction. The major uncertainty arises from the spatial distribution of the induced uniaxial anisotropy (see Fig. 6.6(d) for a map of the local anisotropy). In the simulations the magnitude of $K_{U\parallel}^P(x, y)$ is assumed to scale linearly with the magnitude of the lattice relaxation, which was simulated for instance in Refs. [11, 40]. The spatial average of the induced anisotropy in the simulations is equal to the experimentally determined average anisotropy con-

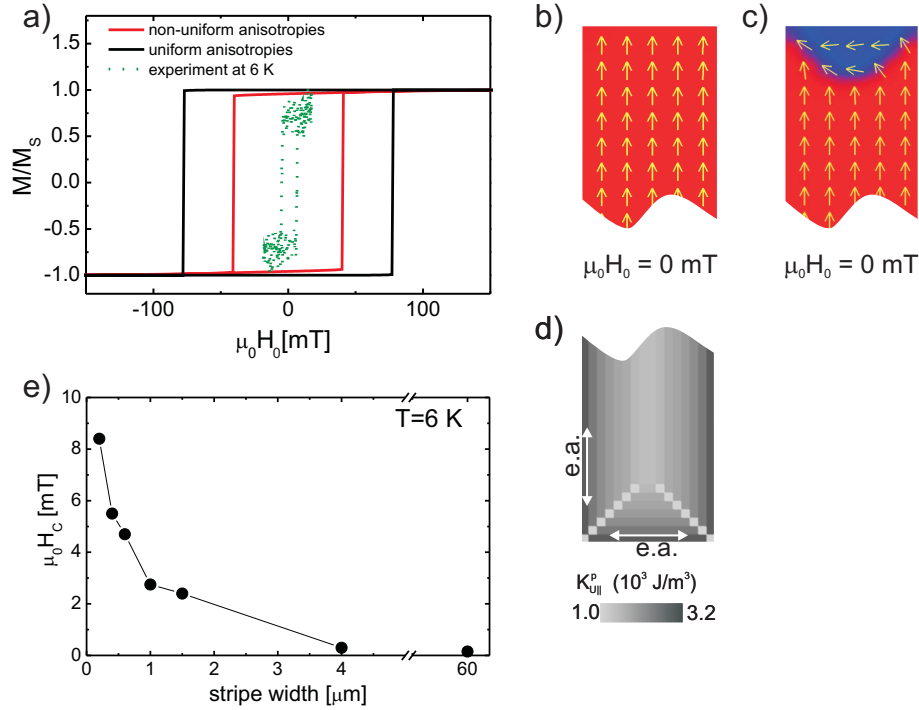


Figure 6.6: (a) Hysteresis loops obtained by micromagnetic simulations for a 400 nm wide and 4 μm long stripe with spatially uniform magnetic anisotropies (black line) and local magnetic anisotropies (red line). The external field was applied parallel to the long axis of the stripe. The dotted line shows experimental data measured on a corresponding structure at 6 K. (b) Magnetic ground state calculated using uniform (averaged) magnetic anisotropies. (c) Modified magnetic ground state due to inhomogeneous magnetic anisotropies. (d) Local distribution of the uniaxial magnetic anisotropy used for the calculation of the ground state (c) and the hysteresis loop (red line) in (a). (e) Experimentally determined coercive fields as a function of stripe width w .

stant $K_{U||}^p = 1.8 \times 10^3 \frac{\text{J}}{\text{m}^3}$ (cf. Section 6.1).

In Fig. 6.6, the results from the experiment and from micromagnetic simulations are summarized for a 400 nm wide stripe. The locally inhomogeneous magnetic anisotropies have a severe effect on the static magnetic properties of the elements such as the magnetic ground state and the coercive field. Experimentally, a coercivity of only 5 mT is found, while the Stoner-Wohlfarth model and micromagnetic simulations with uniform magnetic anisotropies predict a coercive field of 80 mT. When the strain induced edge anisotropies that were determined by the local FMR measurements are included in the micromagnetic simulation, it is found that the non-collinear edge regions nucleate the reversal leading to a more than 50 % reduced coercivity of 40 mT compared to the simulation with uniform magnetic properties (see Fig. 6.6(d) for a map of the local anisotropy that was used in the simulation and the corresponding magnetic groundstate). The even lower coercive field of 5 mT that is measured in the experiment is probably a consequence of thermal excitations that are not considered in the simulation. The temperature in the experiment is only 6 K but in (Ga,Mn)As the spinwave parameter is more than two orders of magnitude larger than e.g. in iron [105]. The large spin-wave parameter in (Ga,Mn)As can be attributed

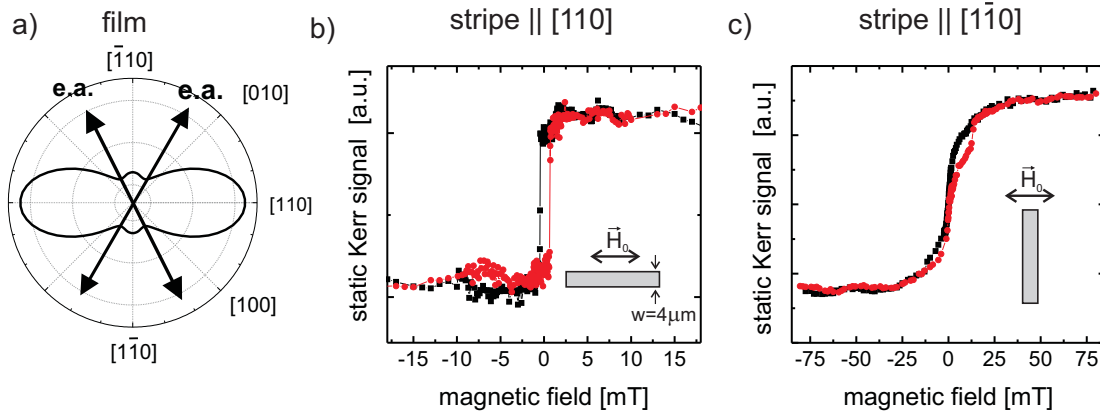


Figure 6.7: (a) Energy landscape of the (Ga,Mn)As film C for $T = 15$ K, calculated using the anisotropy parameters, which were determined experimentally in Section 5.3.2. Hysteresis loops measured at the center of $4 \mu\text{m}$ wide and $15 \mu\text{m}$ long stripes patterned along $[110]$ (b) and $[1\bar{1}0]$ (c) at $T \approx 15 - 20$ K. The external magnetic field \vec{H}_0 was applied along $[110]$.

to a large enhancement of the density of low-energy magnetic excitations due to disorder. This strong magnon softening has been recently shown to be a consequence of significant weakening of bulk spin couplings, resulting in turn from the preferential accumulation of holes in spin clusters and consequent depletion of holes from the bulk spins which support the low-energy extended-state magnon modes [106]. However although the switching field is largely reduced due to thermally excited spinwaves the anisotropic strain relaxation still allows to control the switching field by varying the width of stripe structures. As can be seen in the Fig. 6.6(e) the coercive field changes from 0.15 mT for the extended film to about 8 mT for 200 nm wide stripes. In addition, the presence of a uniaxial anisotropy with the magnetic easy axis parallel to the edges also leads to a modified magnetic ground state, Fig. 6.6(c). The observed behavior is very important for transport measurements with (Ga,Mn)As electrodes for two reasons: The non-collinear magnetic ground state reduces the measured magnetoresistive signal. More importantly the control over the coercivity by varying stripe width allows one to engineer well defined and independent switching of injector and detector electrodes, see Fig. 6.6(d).

The lithographically induced anisotropies even influence the switching process in much larger (Ga,Mn)As elements. This is illustrated for two $4 \mu\text{m}$ wide stripes in Fig. 6.7, which are orientated along $[110]$ and $[1\bar{1}0]$ directions, respectively. The external magnetic field in these experiments is aligned along $[110]$, which for the unpatterned film corresponds to a hard axis, compare Fig. 6.7(a). If the magnetization reversal process in larger elements was unaffected by the edge anisotropies, the hysteresis loops of both stripes should be equal. From Fig. 6.7(b),(c), it is obvious that this is not the case. The square hysteresis loop and the small $\mu_0 H_C = 1.3$ mT in Fig. 6.7(b) can be ascribed to a reversal process which is dominated by domain nucleation and propagation, comparable to the above discussed narrower 400 nm wide stripe. Although the induced anisotropy should be almost zero at the measurement position (center of the element), the edge regions ($< 1 \mu\text{m}$) apparently stabilize the orientation of the magnetization in the entire element. In contrast, in Fig. 6.7(c) a clear hard axis behavior is observed, which can be interpreted as (almost) coherent rotation of the magnetization, because the external

magnetic field is aligned along the hard axes of both intrinsic and patterning induced anisotropies.

These results clearly demonstrate that the switching of the magnetization in (Ga,Mn)As elements - both in the nanometer and micrometer size range - may not be described by means of a single domain approximation. This is of particular importance for various transport experiments, such as AMR, Hall-effect, spin injection, where (Ga,Mn)As elements of such sizes are frequently used, and the magnetic ground state and switching process will depend sensitively on the shape, size, and orientation of the element and the details of the preparation process, such as etch depth.

6.5 Origin of the intrinsic uniaxial in-plane anisotropy

So far, the origin of the the uniaxial in-plane anisotropy in unpatterned (Ga,Mn)As films is controversially discussed. Recent experimental and theoretical studies [40, 47] have tried to explain the origin of $K_{U\parallel}^i$ by means of a trigonal distortion, which is caused by a uniaxial or shear strain in the film plane, and breaks the tetragonal crystal symmetry. Such a strain might be generated by a nonisotropic Mn-distribution, which may be caused by the presence of surface dimers orientated along the $[\bar{1}\bar{1}0]$ direction during the epitaxy [47].

In the Zener mean-field calculations, already small values of $\varepsilon_{xy} = 0.01 - 0.05\%$ [40, 47] would be sufficient to quantitatively explain the magnitude of this experimentally observed intrinsic anisotropy in (Ga,Mn)As films. However, in high resolution x-ray diffraction measurements of (Ga,Mn)As films [33] such a uniaxial strain was never observed. It remains unclear, whether the uniaxial in-plane anisotropy in (Ga,Mn)As films is caused by such an in-plane strain. Nevertheless, local FMR studies of patterned elements can help to illuminate this question. The (Ga,Mn)As film D, which was characterized with respect to its magnetic properties in Section 5.3.1, is well suited to follow up this question because of its large value of the intrinsic anisotropy $K_{U\parallel}^i = 1.86 \times 10^3 \frac{\text{J}}{\text{m}^3}$.

The measurements were performed using the same experimental technique as described in Section 6.1. Details concerning the preparation of the coplanar strip line (CPS) and the (Ga,Mn)As nanostructures are given in Appendix 8.2. The etching depth is ≈ 10 nm larger than the (Ga,Mn)As film thickness (cf. Fig. 6.1(c)). Stripes with the same length $l = 15 \mu\text{m}$, but different width w oriented perpendicular to the signal line of the CPS and disks with different diameters d were prepared, compare Fig. 6.8(a). The long axes of the stripes are aligned parallel to the $[110]$ direction and are oriented perpendicular to the easy axis of the intrinsic anisotropy (along $[1\bar{1}0]$).

As a first step, test measurements of the rectangular structures were performed in order to ensure that strain relaxation induced changes of the anisotropies can compete with the very strong intrinsic anisotropy in this sample. In the following, it is again necessary to distinguish between the intrinsic uniaxial anisotropy $K_{U\parallel}^i$ in unpatterned (Ga,Mn)As films (compare Section 5.3 and Refs. [33, 40, 47]) and the patterning-induced uniaxial anisotropy $K_{U\parallel}^p$ in rectangular structures. In Fig. 6.8(b), the results of angle-resolved FMR measurements of these stripes are compared to the unpatterned film. In

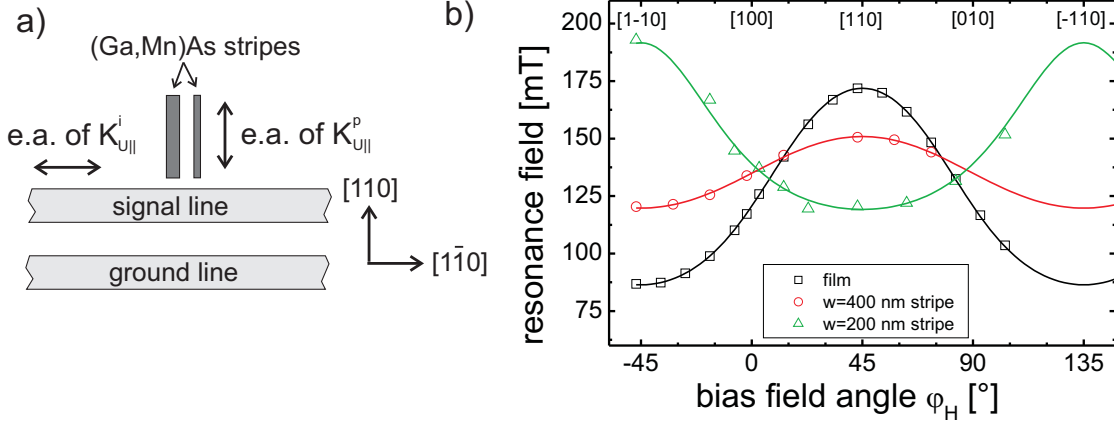


Figure 6.8: (a) Sketch of the measurement configuration showing the orientation of the (Ga,Mn)As stripes and the easy axes of intrinsic and patterning-induced anisotropies. (b) Angular variation of the resonance fields for the (Ga,Mn)As film (squares), $w = 400$ nm wide stripes (circles) and $w = 200$ nm wide stripes (triangles) for $f = 8$ GHz and $T = 25$ K. The solid lines are obtained by the fitting procedure described in Section 5.3.

the 400 nm wide stripe the amplitude of the angular variation $H_R(\varphi_H)$ is significantly reduced. The difference between the resonance fields along the $[110]$ and $[1\bar{1}0]$ directions is decreased by a factor of two. In the narrower 200 nm wide stripes the sign of the effective uniaxial anisotropy is even reversed; the resonance field minimum is now found along the $[110]$ direction. In agreement with the results in Section 6.1.2, this behavior clearly demonstrates that patterning induces a very strong anisotropy $K_{U||}^p$ with an easy axis along the stripe direction $[110]$. In order to determine the value of $K_{U||}^p$ quantitatively, an additional uniaxial anisotropy term has to be added to the energy density. Mathematically, it can be easily shown that $K_{U||}^p$ and $K_{U||}^i$ can be combined into a single uniaxial anisotropy term:

$$E_{U||}^{\text{sum}} \propto K_{U||}^{\text{sum}} \sin^2(\varphi + 45^\circ), \quad (6.1)$$

where the sign of the anisotropy constant $K_{U||}^{\text{sum}} = K_{U||}^i + K_{U||}^p$ determines whether the easy axis of the resulting anisotropy is along the $[1\bar{1}0]$ or the $[110]$ direction. The anisotropy parameters extracted from the theoretical fits (solid lines in 6.8(a)) are $K_{U||}^i = (1.86 \pm 0.06) \times 10^3 \frac{\text{J}}{\text{m}^3}$ for the (Ga,Mn)As film, and $K_{U||}^p = (-1.2 \pm 0.2) \times 10^3 \frac{\text{J}}{\text{m}^3}$ and $K_{U||}^p = (-3.5 \pm 0.3) \times 10^3 \frac{\text{J}}{\text{m}^3}$ for the 400 nm and 200 nm wide stripes, respectively. These results clearly demonstrate, that the magnetic anisotropy can be controlled even in (Ga,Mn)As films with very large values of the intrinsic anisotropy by using carefully chosen element dimensions.

After having verified the very strong effects of the anisotropic lattice relaxation in rectangular structures, disk-shaped elements are addressed. The diameter of the investigated disks ($d = 200$ nm and $d = 300$ nm) is comparable to the width of the rectangular structures above. Therefore strong isotropic strain relaxation effects can be expected. If a trigonal strain ε_{xy} was the origin of the intrinsic uniaxial anisotropy in unpatterned (Ga,Mn)As films, one would expect that this strain should at least partially relax in

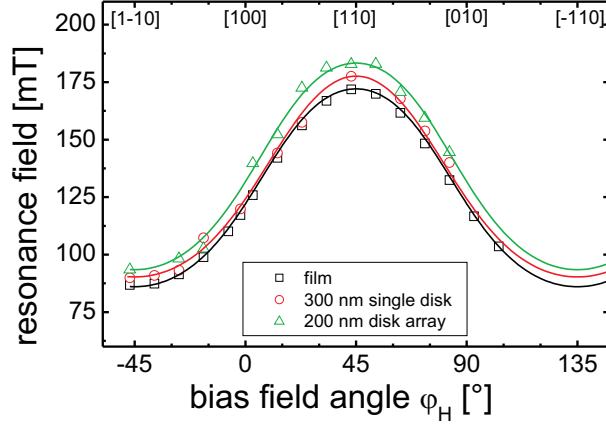


Figure 6.9: Angular variation of the resonance fields for the (Ga,Mn)As film (squares) and 300 nm diameter (circles) and 200 nm diameter disks (triangles) for $f = 8$ GHz and $T = 25$ K. The solid lines are obtained by the fitting procedure described in Section 5.3.

small circular structures and the uniaxial anisotropy should diminish or even vanish. In Fig. 6.9(b), the angular dependence $H_R(\varphi_H)$ of the reference film is compared to disks with different diameters d . The symmetry of $H_R(\varphi_H)$ does not change in the disk-shaped elements, which demonstrates that the in-plane anisotropies remain unchanged. This behavior is also expressed by the anisotropy constants shown in table 6.2, which were derived by fitting the experimental data (solid lines): $K_{U\parallel}$ remains almost constant after patterning, the very small increase of $K_{U\parallel}$ in the disk-shaped elements is within the error bar of the experiment. However, a reduction of a hypothetical intrinsic strain should lead to the opposite behavior, a decrease of $K_{U\parallel}$ in a disk-shaped element. As discussed in Section 6.2, the upward shift of all resonance fields to higher field values can be attributed to a decrease of the perpendicular anisotropy $K_{U\perp}$, generated by a reduction of the isotropic biaxial strain ε_{xx} . Because of the proportionality of perpendicular anisotropy and biaxial strain (Eq. 3.9), the decrease of $K_{U\perp}$ in the 200 nm diameter disks can be directly traced back to an average reduction of the biaxial strain: $\Delta\varepsilon_{xx} = (14 \pm 5)\%$. In conclusion, the results of the magnetic anisotropies in disk-shaped structures clearly indicate that the uniaxial in-plane anisotropy in (Ga,Mn)As films is not caused by a shear or uniaxial strain in the film plane.

	$K_{U\perp}$ [$10^3 \frac{\text{J}}{\text{m}^3}$]	$K_{U\parallel}$ [$10^3 \frac{\text{J}}{\text{m}^3}$]	$K_{C\parallel}$ [$10^3 \frac{\text{J}}{\text{m}^3}$]
Reference	-17.4 ± 0.2	1.86 ± 0.06	-0.13 ± 0.05
Disk $d = 300$ nm	-16.3 ± 0.4	1.91 ± 0.08	-0.11 ± 0.07
Disk $d = 200$ nm	-14.9 ± 0.6	2.0 ± 0.2	-0.19 ± 0.1

Table 6.2: Experimentally determined anisotropy constants of the (Ga,Mn)As reference structure and disk-shaped elements for $T = 25$ K.

In order to further elucidate the origin of the intrinsic anisotropy, ab-initio calculations were performed by S. Mankovsky in the group of H. Ebert at the LMU of Munich.

The theoretical approach is based on a local spin density approximation (LSDA) to the density functional theory. Up to now, only four monolayers (Ga,Mn)As on GaAs(001) were calculated. No mechanism which breaks the tetragonal crystal symmetry such as a uniaxial strain in the film plane is involved. The calculations are based on perfect monocrystalline GaAs and (Ga,Mn)As exhibiting also a perfect (Ga,Mn)As surface. Fig. 6.10 shows a polar plot of the magnetic torque in the film plane for different Mn-concentrations. A direction with maximum torque can be assigned to an easy axis of the magnetization. One can clearly observe a very pronounced uniaxial anisotropy for large Mn-concentrations with an easy axis along [110], which can be ascribed to the symmetry breaking at the surface of the (Ga,Mn)As film and is related to surface states. It would be interesting to see, whether the uniaxial anisotropy in the theoretical calculations scales with $1/t$. Unfortunately, ab-initio calculations of systems with a larger number of (Ga,Mn)As layers are very time-consuming and are not available yet. Also experimental studies of this intrinsic anisotropy as a function of the film thickness would be very valuable. Yet, successively grown (Ga,Mn)As films of various thicknesses cannot be easily compared, because the magnetic properties depend sensitively on the low temperature MBE growth conditions which are not completely reproducible. The thickness dependence of the anisotropies could however be studied by thinning a (Ga,Mn)As film by means of cautious chemical etching steps. On a qualitative level, the theoretical results agree with experimental observations that $K_{U\parallel}^i$ is more pronounced in thinner films with higher Mn-concentrations. As an example, $K_{U\parallel}^i$ in the 20 nm thick $\text{Ga}_{0.875}\text{Mn}_{0.125}\text{As}$ film D is one order of magnitude larger than in the 50 nm thick $\text{Ga}_{0.94}\text{Mn}_{0.06}\text{As}$ films A,B,C. It has to be mentioned that all experimentally investigated (Ga,Mn)As films do not possess a smooth and clean (Ga,Mn)As/vacuum interface but are covered with either amorphous arsenic or by oxides. Therefore, also an influence of the surface layer on the uniaxial anisotropy cannot be excluded in the experiments.

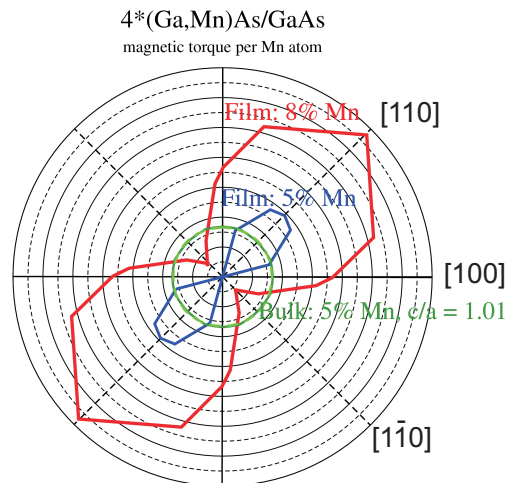


Figure 6.10: Polar plot of the magnetic torque per Mn-atom in the (001)-plane for four monolayers of (Ga,Mn)As with various Mn-concentrations obtained by ab-initio calculations of S. Mankovsky. The results for bulk (Ga,Mn)As with a Mn-concentration of 5 % and a tetragonal distortion $c/a = 1.01$ do not show a uniaxial anisotropy.

In summary, the present experimental results strongly indicate that the uniaxial in-plane anisotropy in (Ga,Mn)As films is not caused by an intrinsic strain in the film plane. Both the presence of $K_{U||}^i$ in very thick films of several micrometer [33], experimental results on thinner (Ga,Mn)As films and the preliminary ab-initio calculations of very thin films suggest that $K_{U||}^i$ is composed of a bulk and a surface contribution. The surface contribution should scale with $1/t$, therefore for thicker films it should be diluted by the bulk contribution. Thickness dependent studies of the magnetic anisotropies of thin films in the nanometer range would be very useful to support this statement. It is however unlikely that surface states actually cause the surface contribution of the uniaxial anisotropy in (Ga,Mn)As because the anisotropy is experimentally observed in all kinds of (Ga,Mn)As samples with various surfaces.

7 Summary and Outlook

In this thesis the magnetic anisotropies of (Ga,Mn)As films and small (Ga,Mn)As structures were investigated experimentally by means of spatially and angle resolved ferromagnetic resonance measurements. For this purpose a novel experimental setup allowing one to perform FMR measurements of nanostructured magnetic elements at cryogenic temperatures was developed.

In chapter 5 the magnetic properties of (Ga,Mn)As films on GaAs(001) substrates were studied experimentally. By combining time-resolved Kerr microscopy and ferromagnetic resonance techniques the different magnetic anisotropies were determined quantitatively. The results are in agreement with those obtained by conventional ferromagnetic resonance measurements demonstrating the reliability of the Kerr-FMR setup. The magneto-crystalline anisotropies in (Ga,Mn)As films and their dependence on the Mn-hole concentration and the strain was investigated and discussed in Section 5.3. It was found, that the different temperature dependence of the magnetic anisotropy constants can lead to temperature induced spin reorientation transitions. An alternative FMR method which is based on the resistive detection of the ferromagnetic resonance was introduced in Section 5.4. Local measurements of the FMR linewidth have allowed to determine the lateral magnetic homogeneity of the (Ga,Mn)As films - an information which is not accessible in conventional FMR studies. The experimental results show that the magnetic inhomogeneities on a micrometer to millimeter length scale largely determine the FMR linewidth. Presumably, these inhomogeneities can be traced back to structural inhomogeneities or gradients (Mn-concentration, concentration of hole compensating defects, etc.), which are generated during the MBE growth or annealing processes. In addition, smaller lateral variations of the magnetic properties were found on a sub-micrometer length scale. The comparison of the experimental data with micromagnetic simulations hints at a lateral variation of the cubic magnetic anisotropy on a length scale of a few hundred nanometer. In Section 5.6 the influence of a short optical pump pulse on the magnetic anisotropies was studied by combining all optical pump-probe and local Kerr-FMR measurements. In contrast to earlier reports where the measurements were performed exclusively in the time domain and the magnetic properties could not be determined quantitatively, no influence of the pump pulse on the magnetic anisotropies on a time scale of hundreds of picoseconds was observed. This is a strong indication that also the lifetime of photoexcited holes is much less than one hundred picoseconds. Lithographically defined (Ga,Mn)As elements were addressed in detail in Chapter 6. The influence of the element shape, size and orientation with respect to the crystallographic axes was studied. In stripe shaped structures the anisotropic relaxation of the lattice strain induces a strong uniaxial in-plane anisotropy. It was found that the easy axis of this induced anisotropy points always perpendicular to the strain relaxation direc-

tion (along the stripe). The magnitude of the anisotropy can be well adjusted by varying the width of the (Ga,Mn)As stripes. These results were supported by spatially resolved measurements of larger micron-sized elements allowing to visualize local variations of the internal magnetic fields caused by variations of the magnetic anisotropies. The systematic investigation of (Ga,Mn)As elements with various dimensions and orientations also showed that both the magnetic anisotropies and the coercive fields in (Ga,Mn)As can be well controlled by lithography. In metallic ferromagnets with large magnetization dipolar (demagnetizing) effects can lead to similar phenomena. However, in the case of (Ga,Mn)As strain relaxation can mimic these effects in a material with a very small magnetization leading to edge localized resonance modes and shape induced magnetic anisotropy. Finally, in Section 6.5 the question was addressed whether the intrinsic uniaxial in-plane anisotropy in unpatterned (Ga,Mn)As films is caused by a uniaxial strain in the film plane which breaks the tetragonal crystal symmetry. The quantitative determination of the magnetic anisotropies in small disk-shaped (Ga,Mn)As elements, where such a strain in the film plane is relaxed, revealed no change of the in-plane anisotropies in comparison with the (Ga,Mn)As film. This is a strong indication that this uniaxial anisotropy is not caused by strains in the film plane. An explanation of the physical origin of this anisotropy is however still missing.

In future experiments, the established Kerr-FMR technique can be employed to study e.g. the temperature dependence of the spin polarization in (Ga,Mn)As or the dependence of the magnetic anisotropies on the hole concentration:

Recently, Vlaminck and Bailleul [107] have demonstrated the spin-wave Doppler effect in the ferromagnetic metal permalloy experimentally. This effect is based on the interaction between spin waves and a spin-polarized current. The spin-polarized current causes a spin-transfer torque acting on the precessing magnetization. The resulting frequency or wavevector shift of the propagating spin wave can be used to determine the spin-polarization of a ferromagnetic material quantitatively. In Ref. [107] this frequency shift was detected inductively using two microwave antennae. Preliminary work was already carried out in the course of this thesis. A spin-wave was excited in (Ga,Mn)As and detected optically by means of the magneto-optical Kerr effect. The aim is to determine the spin polarization in (Ga,Mn)As quantitatively.

In addition, experiments shall be performed in order to gain deeper insight in the role of the carriers in the diluted magnetic semiconductor (Ga,Mn)As. It has already been demonstrated that the Curie temperature and the magnetic anisotropies can be manipulated by changing the hole concentration with a strong electric field in a metal/insulator/(Ga,Mn)As film system [7, 8]. By employing local FMR measurements the dependence of the magnetic anisotropies on the carrier concentration may be determined quantitatively in similar film structures. In comparison with the previously employed integral techniques such as SQUID or magnetotransport, the Kerr-FMR technique offers the advantage that the magnetic anisotropies can be measured directly.

8 Appendix

8.1 Molecular beam epitaxy of (Ga,Mn)As films

The (Ga,Mn)As samples A, B and C were fabricated at the former chair Prof. Dr. Wegscheider at the university of Regensburg. Sample B and C are different pieces of the same (Ga,Mn)As wafer, which differ only in the annealing process. The compositions and thicknesses of the individual layers are given in table 8.1. The growth sequence is the same for both samples and is described in the following: First, the temperature of the semi-insulating epi-ready GaAs(001) substrate was raised to $\approx 600^\circ\text{C}$, in order to desorb water and oxides from the surface of the substrate. Next, at the same temperature a high-temperature (HT) GaAs or AlGaAs buffer layer was grown. After the reduction of the substrate temperature to $\approx 230 - 250^\circ\text{C}$ a low-temperature (LT) GaAs buffer layer and subsequently, the (Ga,Mn)As film with a nominal Mn-concentration $x = 0.06$ was deposited. Finally, the samples were capped with a thick layer of amorphous arsenide. Due to the very low base pressure of the MBE chamber of typically smaller than $1 \cdot 10^{-11}$ mbar, an unintentional incorporation of other impurity atoms during the MBE growth is negligible. More information concerning the details of the (Ga,Mn)As film growth, such as growth rates, sample temperature, etc. can be found in the PhD-thesis of Ursula Wurstbauer [108].

sample	HT-buffer			LT-buffer			(Ga,Mn)As film	
		t [nm]	T [$^\circ\text{C}$]		t [nm]	T [$^\circ\text{C}$]	t [nm]	x [%]
A	GaAs	300	600	GaAs	10	≈ 250	100 nm	6
B,C	AlGaAs	50	600	GaAs	8	≈ 230	50 nm	6

Table 8.1: Composition, growth temperature and thickness t of the individual layers.

8.2 Sample preparation

All (Ga,Mn)As samples were patterned by means of optical and e-beam lithography in the clean room of Prof. Weiss. A micrograph of a representative sample after this preparation process is shown in Fig. 8.1. During these processes, a maximum sample temperature of 150°C for ≈ 10 minutes was reached. Since the annealing processes in (Ga,Mn)As are typically carried out at temperatures in the range of 200°C (lasting for several hours), significant changes of the magnetic or structural properties (diffusion of Mn-interstitials, formation of MnAs clusters, change of Curie temperature, etc.) are not expected.

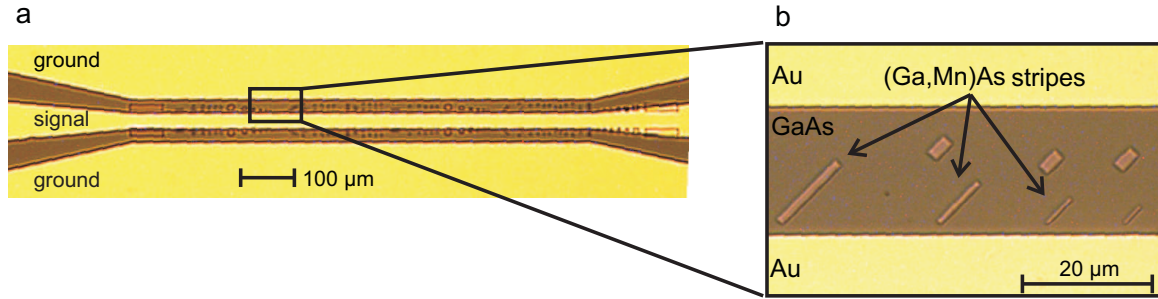


Figure 8.1: (a) Optical micrograph of a representative sample, showing the coplanar waveguide. (b) Smaller detail of the sample displaying some of the (Ga,Mn)As nanostructures.

The preparation of the samples was performed in two lithography steps: In the first step, the (Ga,Mn)As micro and nanostructures were fabricated by e-beam lithography, evaporation of aluminium which serves as an etch mask and ion beam etching. A typical procedure is described in the following:

- Cleaning of the sample ((Ga,Mn)As film on GaAs(001) substrate) with acetone and propanol.
- Spinning of e-beam resist PMMA (200K, 7%) at 8000 rpm for 30 s.
- Post bake at 150°C for ≈ 10 min.
- Exposure of resist with e-beam (dose $200 \frac{\mu\text{C}}{\text{cm}^2}$, acceleration voltage 30 kV).
- Developing of the resist with propanol and MIBK (volume ratio 3:1) for 20 s.
- Stop development in propanol for 20 s.
- Thermal evaporation of aluminium.
- Lift-off process in acetone.
- Etching down into the GaAs substrate by chemical assisted ion beam etching (base pressure $< 5 \cdot 10^{-8}$ mbar, voltage 500 V).
- Removal of the remaining aluminium by dipping into concentrated NaOH.

In the second step the planar metallic waveguides were produced by means of optical lithography, thermal evaporation of the metallization, and subsequent lift-off processes. A typical recipe for the image reversal photoresist AZ5214E (Clariant), which is used here as a negative resist, is given in the following:

- Cleaning of the sample with acetone and propanol.
- Spinning of the photo-resist AZ5214E (6000 rpm, 30 seconds) onto the sample.
- Postbake of the resist at 100°C for 60 seconds.

- Alignment of the sample under a shadow mask in a mask aligner. Exposure of the sample at a dose of approximately 50 mJ/cm^2 .
- Inverse bake at 120°C for 120 seconds.
- Flood exposure of the sample without mask at a dose of approximately 200 mJ/cm^2 .
- Developing of the sample in a mixture of AZ5214E developer and water (ratio 1:4) for 60 seconds.
- Stop development in water for 20 s.
- Thermal evaporation of the metallization: Sputtering of the sample for 20 s and thermal evaporation of several nanometers of chromium for a better adhesion of the subsequent metallization. Evaporation of approximately 200 nm of gold at a base pressure $\sim 10^{-6}$ mbar.
- Lift-off process in acetone.

8.3 Coplanar Waveguides

The precession of the magnetization in ferromagnetic materials takes typically place in the gigahertz frequency range (microwave regime of the electromagnetic spectrum). In order to excite the precessional motion by means of high-frequency magnetic fields, special waveguide structures, which transmit rf-currents in this frequency range, have to be employed. In conventional FMR most commonly rectangular or cylindrical cavities are used, which limit the application to a single microwave frequency. In contrast, the usage of planar waveguide structures allows one to adjust the microwave frequency continuously. Indeed, due to the planar waveguide design, the excitation field \vec{h}_{rf} is spatially non-uniform, which has to be considered when investigating larger magnetic elements.

Two different waveguide designs were employed in the course of this thesis. First, a coplanar waveguide (CPW) consisting of a signal line of width w and two extended ground planes which are separated from the signal line by a gap of width g . As illustrated in Fig. 8.2(b), the (Ga,Mn)As elements are placed in one of the two gaps between signal and ground lines. By using an electro-magnetic simulation software, such as Sonnet [109], the characteristics (transmission, current density, etc.) of the waveguide can be simulated and optimized. The optimum ratio between signal line width and gap depends on the dielectric constant of the substrate. For the coplanar waveguides on semi-insulating GaAs-substrates a ratio of $w : g = 10 : 7$ was employed. The second used type is a coplanar stripline (CPS), consisting of only two conductors of the same width w which are separated by a gap of width g (Fig. 8.2(b)). One of the connectors serves as the signal line, the other as a ground line. For this waveguide design a good rf-transmission was found for a ratio of $w : g = 5 : 4$, in the experiments a conductor width of $25 \mu\text{m}$ was applied. Typically, the measured transmission of such CPW and

CPS waveguides including sample holder and SMP connectors suffered less than 5 dB attenuation in the frequency range from 80 MHz to 20 GHz.

Due to the skin effect, for frequencies in the gigahertz range, the current density across the waveguides is not uniform. The current is pushed towards the edges of the waveguide and decreases towards the center of the conductors. The resulting current densities calculated with an electromagnetic simulation software are plotted in Fig. 8.2(c),(d). In order to determine the excitation field \vec{h}_{rf} at a certain position (y, z) , the conductors are divided into a certain number of elements and the contribution of each current element at a certain position is calculated using Biot-Savarts' law. The resulting excitation field is then obtained by summing the field contributions of each current element. The thickness of the gold conductors in the experiment is ≈ 200 nm, whereas the skin depth of the microwaves at $f=10$ GHz is approximately 400 nm. Therefore, one can neglect the extension of the gold connectors in the z -direction and treat the current distribution inside the connectors as one-dimensional. The resulting excitation fields, decomposed into in- and out-of plane components are illustrated in Fig. 8.2(e)-(h). First, it becomes apparent that the in-plane excitation field $h_{rf,y}(y)$ shows the same dependence on the position y as the current density. The reason is that the (Ga,Mn)As elements are placed very close to the vertical center of the Au leads. Both the in-plane and out-of-plane fields show significant maxima at the edges of signal and ground lines. Since the (Ga,Mn)As elements are either placed in the gap between signal and ground planes of the CPW or beside the center line of the CPS, the excitation field points almost completely out-of-plane. The out-of-plane field decreases with approximately $1/y_0$, where y_0 is the horizontal distance from the signal line.

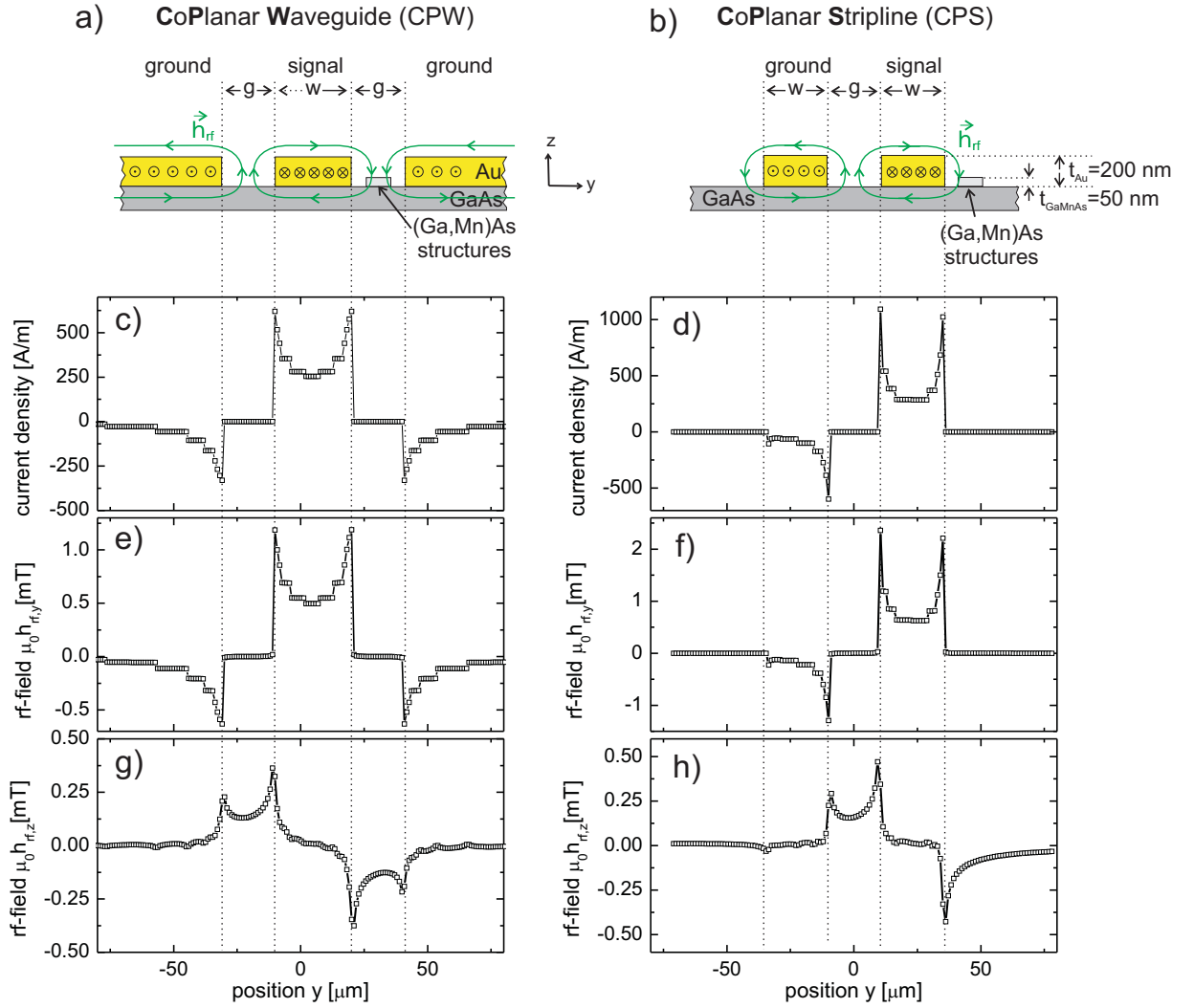


Figure 8.2: Illustration of the cross sections of two types of planar waveguides. (a) Coplanar waveguide with a signal line width $w = 30 \mu\text{m}$ and gaps of $g = 21 \mu\text{m}$. (b) Coplanar stripline with a signal and ground line width $w = 25 \mu\text{m}$ and a gap $g = 20 \mu\text{m}$. The drawings are not true to scale in the z -direction. The current direction in the gold connectors is indicated by symbols. The dotted vertical lines specify the positions of signal and ground lines. (c),(d) The current densities were calculated for a microwave frequency $f = 10 \text{ GHz}$ and for a rf-power $P = 13 \text{ dBm}$ using an electromagnetic simulation software [109]. The discretization of the current is due to the finite number of cells in the E-M-simulation. The current density in the ground line of the CPS (d) is very low, because it is connected to the ground plane of the coplanar sample holder. Therefore only a small mirror current flows opposite to the current in the signal line. The resulting rf-field $\vec{h}_{rf}(y, z)$ is obtained by summing the field distributions of each current element $I(y)$ using Biot-Savarts' law. It is decomposed into in-plane $h_{rf,y}$ (e), (f) and out-of-plane components $h_{rf,z}$ (g), (h). The field calculations were performed for $z = 25 \text{ nm}$ which corresponds to the vertical center of the (Ga,Mn)As elements.

Bibliography

- [1] M. N. Baibich, J. M. Broto, A. Fert, F. N. Van Dau, F. Petroff, P. Etienne, G. Creuzet, A. Friederich, and J. Chazelas. “Giant magnetoresistance of (001)Fe/(001)Cr magnetic superlattices.” *Phys. Rev. Lett.* **61**, 2472 (1988).
- [2] G. Binasch, P. Grünberg, F. Saurenbach, and W. Zinn. “Enhanced magnetoresistance in layered magnetic structures with antiferromagnetic interlayer exchange.” *Phys. Rev. B* **39**, 4828 (1989).
- [3] H. Ohno, A. Shen, F. Matsukura, A. Oiwa, A. Endo, S. Katsumoto, and Y. Iye. “(Ga,Mn)As: A new diluted magnetic semiconductor based on GaAs.” *Appl. Phys. Lett.* **69**, 363 (1996).
- [4] T. Jungwirth, K. Y. Wang, J. Mašek, K. W. Edmonds, J. König, J. Sinova, M. Polini, N. A. Goncharuk, A. H. MacDonald, M. Sawicki, A. W. Rushforth, R. P. Campion, L. X. Zhao, C. T. Foxon, and B. L. Gallagher. “Prospects for high temperature ferromagnetism in (Ga,Mn)As semiconductors.” *Phys. Rev. B* **72**, 165204 (2005).
- [5] V. Novák, K. Olejník, J. Wunderlich, M. Cukr, K. Výborný, A. W. Rushforth, K. W. Edmonds, R. P. Campion, B. L. Gallagher, J. Sinova, and T. Jungwirth. “Curie point singularity in the temperature derivative of resistivity in (Ga,Mn)As.” *Phys. Rev. Lett.* **101**, 077201 (2008).
- [6] L. Chen, S. Yan, P. F. Xu, J. Lu, W. Z. Wang, J. J. Deng, X. Qian, Y. Ji, and J. H. Zhao. “Low-temperature magnetotransport behaviors of heavily Mn-doped (Ga,Mn)As films with high ferromagnetic transition temperature.” *Appl. Phys. Lett.* **95**, 182505 (2009).
- [7] D. Chiba, M. Sawicki, Y. Nishitani, Y. Nakatani, F. Matsukura, and H. Ohno. “Magnetization vector manipulation by electric fields.” *Nature* **455**, 515 (2008).
- [8] M. Sawicki, D. Chiba, A. Korbecka, Y. Nishitani, J. A. Majewski, F. Matsukura, T. Dietl, and H. Ohno. “Experimental probing of the interplay between ferromagnetism and localization in (Ga,Mn)As.” *Nature Phys.* **6**, 22 (2010).
- [9] S. Hümpfner, K. Pappert, J. Wenisch, K. Brunner, C. Gould, G. Schmidt, L. W. Molenkamp, M. Sawicki, and T. Dietl. “Lithographic engineering of anisotropies in (Ga,Mn)As.” *Appl. Phys. Lett.* **90**, 102102 (2007).

-
- [10] J. Wensch, C. Gould, L. Ebel, J. Storz, K. Pappert, M. J. Schmidt, C. Kumpf, G. Schmidt, K. Brunner, and L. W. Molenkamp. “Control of magnetic anisotropy in (Ga,Mn)As by lithography-induced strain relaxation.” *Phys. Rev. Lett.* **99**, 077201 (2007).
- [11] J. Wunderlich, A. C. Irvine, J. Zemen, V. Holý, A. W. Rushforth, E. de Ranieri, U. Rana, K. Výborný, J. Sinova, C. T. Foxon, R. P. Campion, D. A. Williams, B. L. Gallagher, and T. Jungwirth. “Local control of magnetocrystalline anisotropy in (Ga,Mn)As microdevices: Demonstration in current-induced switching.” *Phys. Rev. B* **76**, 054424 (2007).
- [12] Y. Hashimoto, S. Kobayashi, and H. Munekata. “Photoinduced precession of magnetization in ferromagnetic (Ga,Mn)As.” *Phys. Rev. Lett.* **100**, 067202 (2008).
- [13] J. Wang, I. Cotoros, K. M. Dani, X. Liu, J. K. Furdyna, and D. S. Chemla. “Ultrafast enhancement of ferromagnetism via photoexcited holes in GaMnAs.” *Phys. Rev. Lett.* **98**, 217401 (2007).
- [14] S. Blundell. *Magnetism in Condensed Matter*. Oxford University Press (2001).
- [15] A. Aharoni. “Demagnetizing factors for rectangular ferromagnetic prisms.” *J. Appl. Phys.* **83**, 3432 (1998).
- [16] M. Farle. “Ferromagnetic resonance of ultrathin metallic layers.” *Rep. Prog. Phys.* **61**, 755 (1998).
- [17] T. L. Gilbert. “A Lagrangian formulation of the gyromagnetic equation of the magnetization field.” *Phys. Rev.* **100**, 1243 (1955).
- [18] L. Landau and E. Lifshitz. “On the theory of the dispersion of magnetic permeability in ferromagnetic bodies.” *Physik. Z. Sowjetunion* **8**, 153 (1935).
- [19] H. Suhl. “Ferromagnetic resonance in nickel ferrite between one and two kilomegacycles.” *Phys. Rev.* **97**, 555 (1955).
- [20] G. Woltersdorf. *Spin-pumping and two-magnon scattering in magnetic multilayers*. Ph.D. thesis, Simon Fraser University (2004).
- [21] Z. Celinski, K. B. Urquhart, and B. Heinrich. “Using ferromagnetic resonance to measure the magnetic moments of ultrathin films.” *J. Magn. Magn. Mater.* **166**, 6 (1997).
- [22] K. W. Edmonds, K. Y. Wang, R. P. Campion, A. C. Neumann, N. R. S. Farley, B. L. Gallagher, and C. T. Foxon. “High-Curie-temperature $\text{Ga}_{1-x}\text{Mn}_x\text{As}$ obtained by resistance-monitored annealing.” *Appl. Phys. Lett.* **81**, 4991 (2002).

- [23] K. C. Ku, S. J. Potashnik, R. F. Wang, S. H. Chun, P. Schiffer, N. Samarth, M. J. Seong, A. Mascarenhas, E. Johnston-Halperin, R. C. Myers, A. C. Gossard, and D. D. Awschalom. “Highly enhanced Curie temperature in low-temperature annealed [Ga,Mn]As epilayers.” *Appl. Phys. Lett.* **82**, 2302 (2003).
- [24] K. W. Edmonds, P. Bogusławski, K. Y. Wang, R. P. Campion, S. N. Novikov, N. R. S. Farley, B. L. Gallagher, C. T. Foxon, M. Sawicki, T. Dietl, M. Buongiorno Nardelli, and J. Bernholc. “Mn interstitial diffusion in (Ga,Mn)As.” *Phys. Rev. Lett.* **92**, 037201 (2004).
- [25] T. Jungwirth, J. Sinova, J. Mašek, J. Kučera, and A. H. MacDonald. “Theory of ferromagnetic (III,Mn)V semiconductors.” *Rev. Mod. Phys.* **78**, 809 (2006).
- [26] X. Liu and J. K. Furdyna. “Ferromagnetic resonance in $\text{Ga}_{1-x}\text{Mn}_x\text{As}$ dilute magnetic semiconductors.” *J. Phys.: Condens. Matter* **18**, R245 (2006).
- [27] C. Gould, K. Pappert, G. Schmidt, and L. W. Molenkamp. “Magnetic anisotropies and (Ga,Mn)As-based spintronic devices.” *Adv. Mater.* **19**, 323 (2007).
- [28] F. Matsukura, H. Ohno, and T. Dietl. *Handbook of Magnetic Materials, Volume 14*, chapter III-V Ferromagnetic Semiconductors. Elsevier Science (2002).
- [29] J. Blinowski and P. Kacman. “Spin interactions of interstitial Mn ions in ferromagnetic GaMnAs.” *Phys. Rev. B* **67**, 121204(R) (2003).
- [30] X. Liu, Y. Sasaki, and J. K. Furdyna. “Ferromagnetic resonance in $\text{Ga}_{1-x}\text{Mn}_x\text{As}$: Effects of magnetic anisotropy.” *Phys. Rev. B* **67**, 205204 (2003).
- [31] D. E. Bliss, W. Walukiewicz, J. W. Ager, E. E. Haller, K. T. Chan, and S. Tanigawa. “Annealing studies of low-temperature-grown GaAs:Be.” *J. Appl. Phys.* **71**, 1699 (1992).
- [32] M. Glunk, J. Daeubler, L. Dreher, S. Schwaiger, W. Schoch, R. Sauer, W. Limmer, A. Brandlmaier, S. T. B. Goennenwein, C. Bihler, and M. S. Brandt. “Magnetic anisotropy in (Ga,Mn)As: Influence of epitaxial strain and hole concentration.” *Phys. Rev. B* **79**, 195206 (2009).
- [33] U. Welp, V. K. Vlasko-Vlasov, A. Menzel, H. D. You, X. Liu, J. K. Furdyna, and T. Wojtowicz. “Uniaxial in-plane magnetic anisotropy of $\text{Ga}_{1-x}\text{Mn}_x\text{As}$.” *Appl. Phys. Lett.* **85**, 260 (2004).
- [34] J. Mašek and F. Máca. “Lattice expansion of (Ga,Mn)As: The role of substitutional Mn and of the compensating defects.” *Acta Phys. Pol. A* **108**, 789 (2005).
- [35] I. Kuryliszyn-Kudelska, J. Z. Domagała, T. Wojtowicz, X. Liu, E. Łusakowska, W. Dobrowolski, and J. K. Furdyna. “Effect of Mn interstitials on the lattice parameter of $\text{Ga}_{1-x}\text{Mn}_x\text{As}$.” *J. Appl. Phys.* **95**, 603 (2004).

- [36] L. X. Zhao, C. R. Staddon, K. Y. Wang, K. W. Edmonds, R. P. Champion, B. L. Gallagher, and C. T. Foxon. “Intrinsic and extrinsic contributions to the lattice parameter of GaMnAs.” *Appl. Phys. Lett.* **86**, 071902 (2005).
- [37] T. Dietl, H. Ohno, and F. Matsukura. “Hole-mediated ferromagnetism in tetrahedrally coordinated semiconductors.” *Phys. Rev. B* **63**, 195205 (2001).
- [38] K. Khazen, H. J. von Bardeleben, J. L. Cantin, L. Thevenard, L. Largeau, O. Mauguin, and A. Lemaître. “Ferromagnetic resonance of Ga_{0.93}Mn_{0.07}As thin films with constant Mn and variable free-hole concentrations.” *Phys. Rev. B* **77**, 165204 (2008).
- [39] L. Thevenard, L. Largeau, O. Mauguin, A. Lemaître, K. Khazen, and H. J. von Bardeleben. “Evolution of the magnetic anisotropy with carrier density in hydrogenated Ga_{1-x}Mn_xAs.” *Phys. Rev. B* **75**, 195218 (2007).
- [40] J. Zemen, J. Kučera, K. Olejník, and T. Jungwirth. “Magnetocrystalline anisotropies in (Ga,Mn)As: Systematic theoretical study and comparison with experiment.” *Phys. Rev. B* **80**, 155203 (2009).
- [41] S. T. B. Goennenwein, T. A. Wassner, H. Huebl, M. S. Brandt, J. B. Philipp, M. Opel, R. Gross, A. Koeder, W. Schoch, and A. Waag. “Hydrogen control of ferromagnetism in a dilute magnetic semiconductor.” *Phys. Rev. Lett.* **92**, 227202 (2004).
- [42] C. Zener. “Interaction between the *d* shells in the transition metals.” *Phys. Rev.* **81**, 440 (1951).
- [43] T. Dietl, H. Ohno, F. Matsukura, J. Cibert, and D. Ferrand. “Zener model description of ferromagnetism in zinc-blende magnetic semiconductors.” *Science* **287**, 1019 (2000).
- [44] M. Abolfath, T. Jungwirth, J. Brum, and A. H. MacDonald. “Theory of magnetic anisotropy in III_{1-x}Mn_xV ferromagnets.” *Phys. Rev. B* **63**, 054418 (2001).
- [45] K. Y. Wang, K. W. Edmonds, R. P. Champion, B. L. Gallagher, N. R. S. Farley, C. T. Foxon, M. Sawicki, P. Boguslawski, and T. Dietl. “Influence of the Mn interstitial on the magnetic and transport properties of (Ga,Mn)As.” *J. Appl. Phys.* **95**, 6512 (2004).
- [46] A. Shen, H. Ohno, F. Matsukura, Y. Sugawara, N. Akiba, T. Kuroiwa, A. Oiwa, A. Endo, S. Katsumoto, and Y. Iye. “Epitaxy of (Ga,Mn)As, a new diluted magnetic semiconductor based on GaAs.” *J. Cryst. Growth* **175-176**, 1069 (1997).
- [47] M. Sawicki, K.-Y. Wang, K. W. Edmonds, R. P. Champion, C. R. Staddon, N. R. Farley, C. T. Foxon, E. Papis, E. Kamińska, A. Piotrowska, T. Dietl, and B. L. Gallagher. “In-plane uniaxial anisotropy rotations in (Ga,Mn)As thin films.” *Phys. Rev. B* **71**, 121302 (2005).

- [48] M. Sperl. *Magnetische Eigenschaften von (Ga,Mn)As-Schichten und Fe/(Ga,Mn)As-Hybridstrukturen*. Ph.D. thesis, University of Regensburg (2009).
- [49] W. Kipferl. *Spinwellenanregungen in ferromagnetischen ultradünnen epitaktischen Fe-Schichten und Nanostrukturen*. Ph.D. thesis, University of Regensburg (2004).
- [50] A. Hubert and R. Schäfer. *Magnetic Domains - The Analysis of Magnetic Microstructures*. Springer Verlag, Berlin, Heidelberg (2000).
- [51] R. Lang, A. Winter, H. Pascher, H. Krenn, X. Liu, and J. K. Furdyna. “Polar Kerr effect studies of $\text{Ga}_{1-x}\text{Mn}_x\text{As}$ epitaxial films.” *Phys. Rev. B* **72**, 024430 (2005).
- [52] S. Tamaru, J. A. Bain, R. J. M. van de Veerdonk, T. M. Crawford, M. Covington, and M. H. Kryder. “Imaging of quantized magnetostatic modes using spatially resolved ferromagnetic resonance.” *J. Appl. Phys.* **91**, 8034 (2002).
- [53] I. Neudecker, M. Kläui, K. Perzlmaier, D. Backes, L. J. Heyderman, C. A. Vaz, J. A. Bland, U. Rüdiger, and C. H. Back. “Spatially resolved dynamic eigenmode spectrum of Co rings.” *Phys. Rev. Lett.* **96**, 057207 (2006).
- [54] I. Neudecker, K. Perzlmaier, F. Hoffmann, G. Woltersdorf, M. Buess, D. Weiss, and C. H. Back. “Modal spectrum of permalloy disks excited by in-plane magnetic fields.” *Phys. Rev. B* **73**, 134426 (2006).
- [55] M. Buess, R. Höllinger, T. Haug, K. Perzlmaier, U. Krey, D. Pescia, M. R. Scheinfein, D. Weiss, and C. H. Back. “Fourier transform imaging of spin vortex eigenmodes.” *Phys. Rev. Lett.* **93**, 077207 (2004).
- [56] M. Buess, T. P. J. Knowles, R. Höllinger, T. Haug, U. Krey, D. Weiss, D. Pescia, M. R. Scheinfein, and C. H. Back. “Excitations with negative dispersion in a spin vortex.” *Phys. Rev. B* **71**, 104415 (2005).
- [57] E. Beaurepaire, J.-C. Merle, A. Daunois, and J.-Y. Bigot. “Ultrafast spin dynamics in ferromagnetic nickel.” *Phys. Rev. Lett.* **76**, 4250 (1996).
- [58] B. Koopmans, M. van Kampen, J. T. Kohlhepp, and W. J. M. de Jonge. “Ultrafast magneto-optics in nickel: Magnetism or optics?” *Phys. Rev. Lett.* **85**, 844 (2000).
- [59] B. Koopmans. *Spin Dynamics in Confined Magnetic Structures II*, chapter Laser Induced Magnetization Dynamics. Springer Verlag (2003).
- [60] C. Bihler, W. Schoch, W. Limmer, S. T. B. Goennenwein, and M. S. Brandt. “Spin-wave resonances and surface spin pinning in $\text{Ga}_{1-x}\text{Mn}_x\text{As}$ thin films.” *Phys. Rev. B* **79**, 045205 (2009).
- [61] X. Liu, Y. Y. Zhou, and J. K. Furdyna. “Angular dependence of spin-wave resonances and surface spin pinning in ferromagnetic (Ga,Mn)As films.” *Phys. Rev. B* **75**, 195220 (2007).

- [62] C. Kittel. “Excitation of spin waves in a ferromagnet by a uniform rf field.” *Phys. Rev.* **110**, 1295 (1958).
- [63] X. Liu, W. L. Lim, M. Dobrowolska, J. K. Furdyna, and T. Wojtowicz. “Ferromagnetic resonance study of the free-hole contribution to magnetization and magnetic anisotropy in modulation-doped $\text{Ga}_{1-x}\text{Mn}_x\text{As}/\text{Ga}_{1-y}\text{Al}_y\text{As}:\text{Be}$.” *Phys. Rev. B* **71**, 035307 (2005).
- [64] S. T. B. Goennenwein, T. Graf, T. Wassner, M. S. Brandt, M. Stutzmann, J. B. Philipp, R. Gross, M. Krieger, K. Zürn, P. Ziemann, A. Koeder, S. Frank, W. Schoch, and A. Waag. “Spin wave resonance in $\text{Ga}_{1-x}\text{Mn}_x\text{As}$.” *Appl. Phys. Lett.* **82**, 730 (2003).
- [65] M. Sawicki, F. Matsukura, A. Idziaszek, T. Dietl, G. M. Schott, C. Ruester, C. Gould, G. Karczewski, G. Schmidt, and L. W. Molenkamp. “Temperature dependent magnetic anisotropy in (Ga,Mn)As layers.” *Phys. Rev. B* **70**, 245325 (2004).
- [66] T. Hayashi, Y. Hashimoto, S. Katsumoto, and Y. Iye. “Effect of low-temperature annealing on transport and magnetism of diluted magnetic semiconductor (Ga,Mn)As.” *Appl. Phys. Lett.* **78**, 1691 (2001).
- [67] V. Stanciu and P. Svedlindh. “Annealing-induced changes of the magnetic anisotropy of (Ga,Mn)As epilayers.” *Appl. Phys. Lett.* **87**, 242509 (2005).
- [68] C. Bihler, M. Althammer, A. Brandlmaier, S. Geprägs, M. Weiler, M. Opel, W. Schoch, W. Limmer, R. Gross, M. S. Brandt, and S. T. B. Goennenwein. “ $\text{Ga}_{1-x}\text{Mn}_x\text{As}$ piezoelectric actuator hybrids: A model system for magnetoelastic magnetization manipulation.” *Phys. Rev. B* **78**, 045203 (2008).
- [69] K.-Y. Wang, M. Sawicki, K. W. Edmonds, R. P. Campion, S. Maat, C. T. Foxon, B. L. Gallagher, and T. Dietl. “Spin reorientation transition in single-domain (Ga,Mn)As.” *Phys. Rev. Lett.* **95**, 217204 (2005).
- [70] M. Tsoi, A. G. M. Jansen, J. Bass, W.-C. Chiang, M. Seck, V. Tsoi, and P. Wyder. “Excitation of a magnetic multilayer by an electric current.” *Phys. Rev. Lett.* **80**, 4281 (1998).
- [71] Y. S. Gui, S. Holland, N. Mecking, and C. M. Hu. “Resonances in ferromagnetic gratings detected by microwave photoconductivity.” *Phys. Rev. Lett.* **95**, 056807 (2005).
- [72] A. Wirthmann, X. Hui, N. Mecking, Y. S. Gui, T. Chakraborty, C. Hu, M. Reinwald, C. Schüller, and W. Wegscheider. “Broadband electrical detection of spin excitations in $\text{Ga}_{0.98}\text{Mn}_{0.02}\text{As}$ using a photovoltage technique.” *Appl. Phys. Lett.* **92**, 232106 (2008).

- [73] Y. S. Gui, N. Mecking, X. Zhou, G. Williams, and C.-M. Hu. “Realization of a room-temperature spin dynamo: The spin rectification effect.” *Phys. Rev. Lett.* **98**, 107602 (2007).
- [74] F. Matsukura, M. Sawicki, T. Dietl, D. Chiba, and H. Ohno. “Magnetotransport properties of metallic (Ga,Mn)As films with compressive and tensile strain.” *Physica E* **21**, 1032 (2004).
- [75] K. Y. Wang, K. W. Edmonds, R. P. Campion, L. X. Zhao, C. T. Foxon, and B. L. Gallagher. “Anisotropic magnetoresistance and magnetic anisotropy in high-quality (Ga,Mn)As films.” *Phys. Rev. B* **72**, 085201 (2005).
- [76] D. V. Baxter, D. Ruzmetov, J. Scherschligt, Y. Sasaki, X. Liu, J. K. Furdyna, and C. H. Mielke. “Anisotropic magnetoresistance in $\text{Ga}_{1-x}\text{Mn}_x\text{As}$.” *Phys. Rev. B* **65**, 212407 (2002).
- [77] W. Limmer, M. Glunk, J. Daeubler, T. Hummel, W. Schoch, R. Sauer, C. Bihler, H. Huebl, M. S. Brandt, and S. T. B. Goennenwein. “Angle-dependent magnetotransport in cubic and tetragonal ferromagnets: Application to (001)- and (113)A-oriented (Ga,Mn)As.” *Phys. Rev. B* **74**, 205205 (2006).
- [78] G. Woltersdorf and B. Heinrich. “Two-magnon scattering in a self-assembled nanoscale network of misfit dislocations.” *Phys. Rev. B* **69**, 184417 (2004).
- [79] K. Lenz, H. Wende, W. Kuch, K. Baberschke, K. Nagy, and A. Jánossy. “Two-magnon scattering and viscous Gilbert damping in ultrathin ferromagnets.” *Phys. Rev. B* **73**, 144424 (2006).
- [80] E. Schlömann. “Spin-wave analysis of ferromagnetic resonance in polycrystalline ferrites.” *J. Phys. Chem. Solids* **6**, 242 (1958).
- [81] C. E. Patton, C. H. Wilts, and F. B. Humphrey. “Relaxation processes for ferromagnetic resonance in thin films.” *J. Appl. Phys.* **38**, 1358 (1967).
- [82] R. Arias and D. L. Mills. “Extrinsic contributions to the ferromagnetic resonance response of ultrathin films.” *Phys. Rev. B* **60**, 7395 (1999).
- [83] R. D. McMichael, D. J. Twisselmann, and A. Kunz. “Localized ferromagnetic resonance in inhomogeneous thin films.” *Phys. Rev. Lett.* **90**, 227601 (2003).
- [84] C. Chappert, K. L. Dang, P. Beauvillain, H. Hurdequint, and D. Renard. “Ferromagnetic resonance studies of very thin cobalt films on a gold substrate.” *Phys. Rev. B* **34**, 3192 (1986).
- [85] J. Sinova, T. Jungwirth, X. Liu, Y. Sasaki, J. K. Furdyna, W. A. Atkinson, and A. H. MacDonald. “Magnetization relaxation in (Ga,Mn)As ferromagnetic semiconductors.” *Phys. Rev. B* **69**, 085209 (2004).

- [86] Y. H. Matsuda, A. Oiwa, K. Tanaka, and H. Munekata. “Ferromagnetic resonance study of magnetization relaxation in GaMnAs.” *Physica B* **376**, 668 (2006).
- [87] K. Khazen, H. J. von Bardeleben, M. Cubukcu, J. L. Cantin, V. Novak, K. Olejnik, M. Cukr, L. Thevenard, and A. Lemaître. “Anisotropic magnetization relaxation in ferromagnetic Ga_{1-x}Mn_xAs thin films.” *Phys. Rev. B* **78**, 195210 (2008).
- [88] Object Oriented MicroMagnetic Framework. The OOMMF code is available at <http://math.nist.gov/oommf/>.
- [89] R. D. McMichael. “A mean-field model of extrinsic line broadening in ferromagnetic resonance.” *J. Appl. Phys.* **103**, 07B114 (2008).
- [90] J. Wang, L. Cywiński, C. Sun, J. Kono, H. Munekata, and L. J. Sham. “Femtosecond demagnetization and hot-hole relaxation in ferromagnetic Ga_{1-x}Mn_xAs.” *Phys. Rev. B* **77**, 235308 (2008).
- [91] E. Rozkotová, P. Němec, P. Horodyská, D. Sprinzl, F. Trojánek, P. Malý, V. Novák, K. Olejník, M. Cukr, and T. Jungwirth. “Light-induced magnetization precession in GaMnAs.” *Appl. Phys. Lett.* **92**, 122507 (2008).
- [92] E. Rozkotová, P. Němec, D. Sprinzl, P. Horodyská, F. Trojánek, P. Malý, V. Novák, K. Olejník, M. Cukr, and T. Jungwirth. “Laser-Induced Precession of Magnetization in GaMnAs.” *IEEE T. Magn.* **44**, 2674 (2008).
- [93] E. Rozkotová, P. Němec, N. Tesařová, P. Malý, V. Novák, K. Olejník, M. Cukr, and T. Jungwirth. “Coherent control of magnetization precession in ferromagnetic semiconductor (Ga,Mn)As.” *Appl. Phys. Lett.* **93**, 232505 (2008).
- [94] E. Kojima, R. Shimano, Y. Hashimoto, S. Katsumoto, Y. Iye, and M. Kuwata-Gonokami. “Observation of the spin-charge thermal isolation of ferromagnetic Ga_{0.94}Mn_{0.06}As by time-resolved magneto-optical measurements.” *Phys. Rev. B* **68**, 193203 (2003).
- [95] C. Thomsen, H. T. Grahn, H. J. Maris, and J. Tauc. “Surface generation and detection of phonons by picosecond light pulses.” *Phys. Rev. B* **34**, 4129 (1986).
- [96] J. S. Blakemore. “Semiconducting and other major properties of gallium arsenide.” *J. Appl. Phys.* **53**, 123 (1982).
- [97] M. D. Sturge. “Optical absorption of gallium arsenide between 0.6 and 2.75 eV.” *Phys. Rev.* **127**, 768 (1962).
- [98] H.-Y. Hao and H. J. Maris. “Dispersion of the long-wavelength phonons in Ge, Si, GaAs, quartz, and sapphire.” *Phys. Rev. B* **63**, 224301 (2001).
- [99] J. Zemen, T. Jungwirth, and J. Wunderlich. “Uniaxial strain controlling magnetic anisotropy in (Ga,Mn)As.” *Acta Phys. Polonica A* **112**, 431 (2007).

-
- [100] J. Rothman, M. Kläui, L. Lopez-Diaz, C. A. F. Vaz, A. Bleloch, J. A. C. Bland, Z. Cui, and R. Speaks. “Observation of a bi-domain state and nucleation free switching in mesoscopic ring magnets.” *Phys. Rev. Lett.* **86**, 1098 (2001).
- [101] S. P. Li, D. Peyrade, M. Natali, A. Lebib, Y. Chen, U. Ebels, L. D. Buda, and K. Ounadjela. “Flux closure structures in cobalt rings.” *Phys. Rev. Lett.* **86**, 1102 (2001).
- [102] U. Welp, V. K. Vlasko-Vlasov, X. Liu, J. K. Furdyna, and T. Wojtowicz. “Magnetic domain structure and magnetic anisotropy in $\text{Ga}_{1-x}\text{Mn}_x\text{As}$.” *Phys. Rev. Lett.* **90**, 167206 (2003).
- [103] J.-P. Adam, S. Rohart, J. Ferré, A. Mougin, N. Vernier, L. Thevenard, A. Lemaître, G. Faini, and F. Glas. “Macrospin behavior and superparamagnetism in (Ga,Mn)As nanodots.” *Phys. Rev. B* **80**, 155313 (2009).
- [104] The LLG Micromagnetics Simulator can be obtained at <http://llgmicro.home.mindspring.com>.
- [105] M. Sperl, A. Singh, U. Wurstbauer, S. K. Das, A. Sharma, M. Hirmer, W. Nolting, C. H. Back, W. Wegscheider, and G. Bayreuther. “Spin-wave excitations and low-temperature magnetization in the dilute magnetic semiconductor (Ga,Mn)As.” *Phys. Rev. B* **77**, 125212 (2008).
- [106] A. Singh. “Clustering induced suppression of ferromagnetism in diluted magnets.” *Phys. Rev. B* **75**, 035206 (2007).
- [107] V. Vlaminck and M. Bailleul. “Current-induced spin-wave doppler shift.” *Science* **322**, 410 (2008).
- [108] U. Wurstbauer. *Herstellung und Charakterisierung von Mangan dotierten III-V Halbleiterheterostrukturen*. Ph.D. thesis, University of Regensburg (2008).
- [109] Sonnet - the high frequency electromagnetic software is available at <http://www.sonnetsoftware.com/>.

Publications

Part of the work presented in Chapter 6 has been published as:

- **Mapping the magnetic anisotropy in (Ga,Mn)As nanostructures**
F. Hoffmann, G. Woltersdorf, W. Wegscheider, A. Einwanger, D. Weiss, and C. H. Back
Phys. Rev. B **80**, 054417 (2009)

Other publications:

- **Mode degeneracy due to vortex core removal in magnetic disks**
F. Hoffmann, G. Woltersdorf, K. Perzlmaier, A. N. Slavin, V. S. Tiberkevich,
A. Bischof, D. Weiss, and C. H. Back
Phys. Rev. B **76**, 014416 (2007)

Other publications (in collaboration):

- **Modal spectrum of permalloy disks excited by in-plane magnetic fields**
I. Neudecker, K. Perzlmaier, F. Hoffmann, G. Woltersdorf, M. Buess, D. Weiss
and C. H. Back
Phys. Rev. B **73**, 134426 (2006)
- **Imaging magnetic excitations in confined magnetic structures**
I. Neudecker, F. Hoffmann and G. Woltersdorf and C.H. Back
J. Phys. D Appl. Phys. **41**, 164010 (2008)

Acknowledgements

Finally, I would like to thank everyone who has contributed to this PhD-thesis. Specially I want to thank the following people:

- My supervisor Prof. Dr. Christian Back for giving me the chance to perform such interesting experiments, for many helpful and motivating discussions and experimental ideas. I appreciate that he still likes to spend time in the lab in order to follow up on various physical topics.
- Prof. Dr. Dieter Weiss for providing access to the clean room and for managing the Sonderforschungsbereich 689.
- Dr. Georg Woltersdorf was always the first contact person for all kinds of physical, experimental and technical questions. I highly appreciate his broad physical knowledge and would like to thank him for many explanations, discussions, proofreads, and e-beam lithography steps.
- Dr. Ursula Wurstbauer and Dr. Janusz Sadowski for the MBE growth of (Ga,Mn)As films.
- Dr. Vít Novák for providing the highly doped (Ga,Mn)As film.
- Dr. Matthias Sperl for helpful discussions and SQUID measurements.
- Matthias Kiessling for conventional FMR and SQUID measurements.
- Dr. Sergey Mankovsky for discussions on the origin of the uniaxial in-plane anisotropy and for providing the results of ab-initio calculations on thin (Ga,Mn)As films.
- Andreas Einwanger for preparing (Ga,Mn)As structures with e-beam lithography.
- Hans Bauer for micromagnetic simulations using the OOMMF code.
- Tobias Stöckl and the staff of the mechanical workshop for their help with the design and fabrication of the Kerr-FMR setup.
- The electronic workshop for the repair of electronic devices and the fabrication of special electronic components.

- I want to thank Alexander Weber, Michael Binder, Ingo Neudecker, Rüdiger Pürner, Paul Ramm, Frederik Süßmann, Bernhard Endres, and many others for helpful discussions, and the pleasant atmosphere both in the lab and in the office.
- Financial support through the Sonderforschungsbereich 689 "Spinphänomene in reduzierten Dimensionen" is gratefully acknowledged.
- In addition to scientific research, I would like to mention the pleasant environment at the chair Prof. Back. I would like to thank also everyone who has contributed to extracurricular activities such as Christmas parties, excursions, hiking tours, BBQ's, etc.

Last but not least, I would like to thank my girlfriend Eva and my parents for their permanent support and encouragements.